CHEMICAL TUNING OF THERMAL EXPANSION IN OXIDES

A Thesis
Presented to
The Academic Faculty

by

Chad Ruschman

In Partial Fulfillment
of the Requirements for the Degree
Master's of Science in Chemistry
School of Chemistry and Biochemistry

Georgia Institute of Technology
August 2010

CHEMICAL TUNING OF THERMAL EXPANSION IN OXIDES

Approved by:

Dr. Angus P. Wilkinson, Advisor
School of Chemistry and Biochemistry
Georgia Institute of Technology

Dr. Z. John Zhang
School of Chemistry and Biochemistry
Georgia Institute of Technology

Dr. E. Kent Barefield
School of Chemistry and Biochemistry
Georgia Institute of Technology

Date Approved: May 19, 2010

To my mother and my wife Lindsay

ACKNOWLEDGEMENTS

First and foremost, I would like to give thanks to my advisor, Dr. Angus P. Wilkinson. He has been an exceptional advisor, from whom I have learned much. His constant support and guidance have helped me in my endeavor at Georgia Tech, and I will forever be grateful for his help. I would also like to take the time to thank my committee members Dr. Z. John Zhang and Dr. E. Kent Barefield for taking their time to provide feedback and help me improve this thesis.

I would like to thank the past and present members of the Wilkinson group whose attitudes and friendship have made my time at Georgia Tech much more enjoyable. I especially like to thank Dr. Andrew C. Jupe, for his assistance in data collection and analysis of some of our synchrotron data and teaching me a little about program writing. I would also like to thank Benjamin Greve for staying up with me for those long shifts at Argonne National Lab while collecting data on these samples. Dr. Mehmet Cetinkol also deserves thanks for teaching me new laboratory techniques as I got my start here at Georgia Tech. The assistance and friendship from Dr. Ken Martin of Berry College, Dr. Carine Vanpetegham, and Cody Morelock are also appreciated.

Many of the experiments in this thesis were performed at the Advanced Photon Source Argonne National Lab (APS, ANL). I acknowledge the U.S. Department of Energy for financially supporting the synchrotron facility used for much of the experimental work in this thesis.

I especially would like to thank the beam line scientists at the APS who helped make the work possible. First, I would like to thank Dr. Karena W. Chapman and Dr. Peter J. Chupas for allowing us to use their high pressure diamond anvil cells and flow furnace in our experiments. They also helped with the set-up of beam line 11-ID-B and data collection on these samples. Thanks are also extended to Dr. Peter L. Lee who assisted us in the set up and data collection of samples on beam line 1-BM-C and collected the high resolution powder x-ray diffraction data for us on beam line 11-BM. I would also like to thank Dr. Yu-Sheng Chen and the other staff at CHEMMatCARS, Sector 15, who collected the single crystal data for $Zr_2(PO_4)_2(SO_4)$.

I would also like to acknowledge the National Science Foundation for providing the funding for this work through grants DMR-0905842 and DMR-0605671.

Last, I would like to thank my family and friends for their support and encouragement in this endeavor. Most importantly, I would like to thank my beautiful wife Lindsay who gave up everything in Kentucky to move down to Georgia with me, not knowing as to what we would encounter. Your constant love and support is my true inspiration. Thank you for everything.

TABLE OF CONTENTS

LIST OF TABLES

LIST OF FIGURES

SUMMARY

This thesis focuses on the synthesis, characterization, and thermal expansion of oxide materials belonging to framework families that have previously been known to exhibit negative thermal expansion. The reported body of work contributes to our understanding of how chemical changes can affect the thermal expansion and other properties of oxides.

In **Chapter 2**, the thermal expansion of $Zr_2(PO_4)_2(SO_4)$ is discussed, based on *in-situ* variable temperature diffraction measurements. $Zr_2(PO_4)_2(SO_4)$ shows anisotropic positive thermal expansion with contraction of two axes and expansion along one axis. Additional peaks were seen in the diffraction patterns recorded during the variable temperature experiment indicating that earlier reports on material had incorrectly assigned its space group. TGA and crystal density measurements strongly suggested that the material contained hydroxyl defects within the crystal structure.

Chapter 3, reports an *in-situ* variable pressure diffraction study of $Hf_2(PO_4)_2(SO_4)$ inside of a diamond anvil cell. The unit cell volume has an unusual linear dependence on pressure. Changes in the normalized lattice parameters on compression, suggest the possibility of one or two phase transitions. Ambient pressure diffraction measurements on $Hf_2(PO_4)_2(SO_4)$ showed additional reflections, similar to those seen for $Zr_2(PO_4)_2(SO_4)$, suggesting that the two materials have the same space group.

Chapter 4, is a summary of our attempts to synthesize high quality PbP_2O_7 via the dehydration of $Pb(HPO_4)_2 \cdot xH_2O$. We were unable to find a reproducible procedure for the synthesis of high quality PbP_2O_7.

Finally, in **Chapter 5**, we examine the effects of pressure and temperature on the local structure of $ZrMo_2O_8$ using the pair distribution function (PDF method. The short range structure of $ZrMo_2O_8$ is not well described by crystallographic models in space groups *P2$_1$3* or *Pa-3*. The nearest neighbor Zr-Mo separation, as determined from the PDFs, shows the same dependence on temperature as the materials lattice constant. Under pressure, $ZrMo_2O_8$ experiences an irreversible pressure induced amorphization. However, the Zr-O-Mo linkages are still well defined in the amorphous material; and apparently change geometry reversibly on compression followed by decompression.

CHAPTER 1

INTRODUCTION

1.1 Thermal Expansion

Thermal expansion is a property that is commonly overlooked in regards to materials, mainly because it is common knowledge that most materials expand upon heating (positive thermal expansion). However, since most products are a combination of several materials, problems can arise when two interfaces interact when heating is involved if there is a difference in the thermal expansion coefficients. Upon rapid heating and cooling of these materials, cracking can occur between the interfaces due to a difference in the thermal expansion coefficients. Cracking is a symptom of poor thermal shock resistance caused by a non-zero coefficient of thermal expansion combined with low thermal distribution and low toughness. Thus, it is necessary to create materials that would ideally have zero thermal expansion or as close to zero thermal expansion as possible.

In an ideal world, the interatomic potential between two atoms would behave like a harmonic oscillator. As two atoms are brought together, attractive forces take over and the possibility of bond formation occurs lowering the potential energy of the system. Electron-electron repulsion between these two atoms becomes greater as the distance between the two atoms gets shorter and the potential energy of the system increases as in

Figure 1.1. However, by increasing the temperature of the system, the time average bond distance, R, would remain unchanged and no thermal expansion would occur.

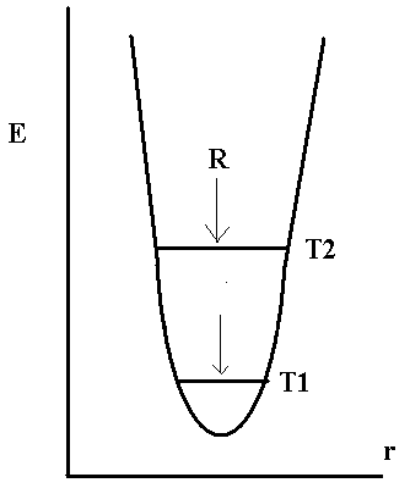

Figure 1.1. Potential energy versus interatomic distance in a harmonic oscillator with average time bond distance R.

The potential energy between two atoms is better described as an anharmonic oscillator with an asymmetric potential energy well (see Figure 1.2). Thermal expansion arises because as the temperature and energy are increased, there is a change in the time average distance R. The overall change in the distance is accompanied by thermal expansion of the material. The degree of change between R_1 and R_2, the two time average distances, is related to the bond strength. In general, as the bond becomes stronger, the two atoms involved become more like a harmonic oscillator and the average bond length has a smaller temperature dependence.

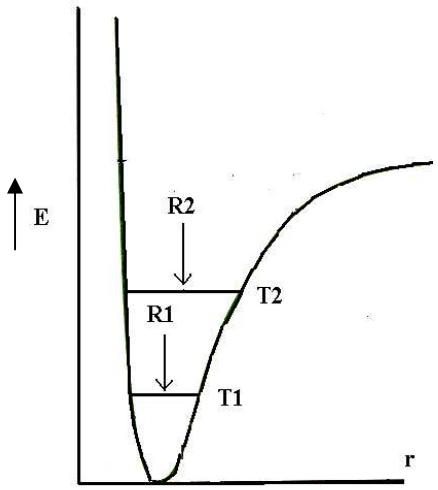

Figure 1.2. Potential energy versus internuclear distance between two atoms behaving like an anharmonic oscillator.

The thermal expansion of materials can be classified in one of two ways, isotropic or anisotropic. In isotropic thermal expansion, all of the unit cell axes expand by the same amount. Isotropic thermal expansion is only seen in cubic crystalline materials and glasses. Anisotropic thermal expansion occurs when expansion is independent in each individual axis. Thermal expansion can be quantified and compared using the coefficient of thermal expansion (CTE or α). The average linear CTE (α_ℓ) is defined as:

$$\alpha_\ell = \frac{d(\ln L)}{dT} = \frac{L - L_0}{L_0 (T - T_0)}, \tag{1}$$

where L and L_0 are the values of the lattice constant at temperature T and T_0, respectively. When the material is anisotropic, α_ℓ is reported for each axis of the material. The volume coefficient of thermal expansion α_V is defined as:

$$\alpha_V = \frac{d(\ln V)}{dT} = \frac{1}{V_T}\frac{dV_T}{dT}, \tag{2}$$

where V is the volume and T is the temperature. In most materials, α_V is directly proportional to the heat capacity C_V (which have similar temperature dependence)[1] as can

be seen in the Grüneisen equation for the volume coefficient of thermal expansion (equation 3):

$$\alpha_V(T) = \frac{\gamma B_0 C_V(T)}{V_0}, \quad (3)$$

where B_0 is the isothermal compressibility, V_0 is the molar volume at T = 0 K and γ is the Grüneisen parameter.[2] Since B_0 and V_0 always have to be positive, the sign of the coefficient of thermal expansion is dependent on the Grüneisen parameter, which can be positive or negative. When the parameter is negative, the material shows negative thermal expansion. While α_ℓ and α_V vary with temperature, averages over some temperature range are typically reported

Individual materials are classified based on their thermal expansion coefficients allowing for them to be separated into three groups:[2]

High Expansion: $\alpha > 8 \times 10^{-6}\ K^{-1}$

Intermediate Expansion: $2 < \alpha < 8 \times 10^{-6}\ K^{-1}$

Low Expansion: $\alpha < 2 \times 10^{-6}\ K^{-1}$

As described above, materials exhibiting low thermal expansion are important, as they suffer less from microcracking and poor thermal shock resistance. One of the earliest materials reported to have a low coefficient of thermal expansion was Invar, an alloy comprised of iron and nickel with a formula of $Fe_{65}Ni_{35}$ and a CTE of $0.01 \times 10^{-6}\ K^{-1}$.[2] Following this material, there were several oxides, cordierite ($Mg_2Al_4Si_5O_{18}$), zircon ($ZrSiO_4$), and silica glass (SiO_2) which were found to exhibit low thermal expansion.[2] These materials have frameworks built from corner sharing polyhedra bridged by oxygen atoms in the framework. Following these materials, came the discovery of a series of lithium aluminum silicates by Hummel beginning in 1948.[3, 4] The materials β-

spodumene, $Li_2Al_2Si_4O_{12}$, and β-eucryptite, $Li_2Al_2Si_2O_8$ were found to have CTEs of 0.9 x 10^{-6} K^{-1} and -6.2 x 10^{-6}, respectively.[2-4] In the 1980's, came the discovery of $NaZr_2(PO_4)_3$ (NZP) which has corner-sharing ZrO_6 octahedra and PO_4 tetrahedra.[5] Sodium ions in this structure occupy cavities. The CTE of NZP was found to be -0.4 x 10^{-6} K^{-1}, as seen in Table 1.1 with other important low and negative thermal expansion materials.[2, 5] The thermal expansion coefficients of materials in this family are altered as ions are interchanged, leading researchers to refocus on materials exhibiting negative thermal expansion.

Table 1.1. Coefficients of thermal expansion for some low and negative CTE materials.[2]

Material	Average CTE ($ºC^{-1}$ x 10^{-6})	Temperature range (ºC)
Beryl, $Be_3Al_2Si_6O_{18}$	2.0	25-1000
Cordierite, $Mg_2Al_4Si_5O_{18}$	1.4	25-800
PMN, $Pb(Mg_{1/3}Nb_{1/3})O_3$	1.0	-100-100
β-Spodumene, $Li_2O{\cdot}Al_2O_3{\cdot}4SiO_2$	0.9	25-1000
$Ca_{0.75}Sr_{0.25}Zr_4P_6O_{24}$ (NZP)	0.6	25-1000
SiO_2 glass	0.5	25-1000
Zerodur	0.12	20-600
$SiO_2{\cdot}TiO_2$ glasses	0.05-(-0.03)	25-800
Invar	0.01	5-30
NZP, $NaZr_2P_3O_{12}$	-0.4	25-1000
β-Eucryptite, $Li_2O{\cdot}Al_2O_3{\cdot}2SiO_2$	-6.2	25-1000

1.2 Negative Thermal Expansion

While many materials exhibit positive thermal expansion on heating, there are several examples where a contraction is observed over a given temperature range resulting in negative thermal expansion (NTE).[4-15] NTE materials are of importance because they can be combined with positive expansion materials to control the thermal expansion of a composite, possibly resulting in materials that exhibit zero thermal expansion. Significantly, this could improve the overall usability of ceramics or allow exact positioning of optics or electronics improving overall function. Given their potential, there has been much interest in NTE materials over the last fifteen years.[8-11, 13, 15-20]

The earliest known observance of NTE was probably for water.[21] Water's highest density is obtained at 4º C, thus from 0 to 4º C water exhibits NTE. In solids, negative coefficients of thermal expansion were first observed in 1907 for quartz at temperatures up to 100º C.[22]

The negative thermal expansion of these materials cannot be explained by the potential energy diagram seen in Figure 1.1.2, but the framework dynamics provide an explanation for this phenomenon. The frameworks of these materials consist of corner-sharing rigid polyhedra units which are connected through oxygen atoms with a two-fold coordination with M-O-M bond angles of approximately 180º. The connectivity of the framework leaves void space within the framework. As the material is heated, the transverse vibrations in the oxygen atoms cause the rigid polyhedra units to fill the void space in the framework decreasing the volume of the unit cell as seen in Figure 1.3.[18] The filling of the void space leaves the polyhedra almost unchanged since the expansion of the metal-oxygen bonds is negligible compared to the transverse motion of the oxygen

atoms. The transverse motion in turn causes the average metal-metal distances to become shorter at higher temperature. The transverse vibrational modes can make a negative contribution to the Grüneisen parameter. In ZrW_2O_8, HfW_2O_8, and $ZrMo_2O_8$, it has been shown that these low frequency vibrational modes, which contribute to the negative Grüneisen parameter, are responsible for the observed NTE.[23-25]

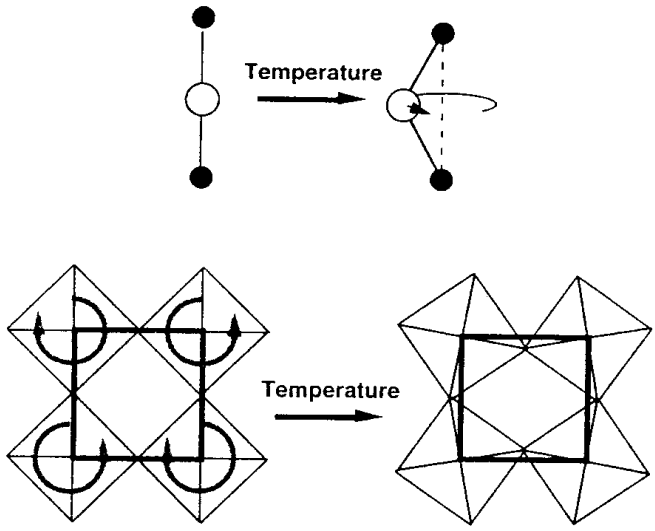

Figure 1.3. Diagram from Evans *et al.* [18] depicting the transverse vibrations of oxygen atoms (top) and the mechanism for negative thermal expansion in the frameworks with rigid polyhedra (bottom).

Research on materials exhibiting NTE has focused on corner-sharing frameworks. These frameworks have 1) void space within the framework, 2) oxygen atoms with a two-fold coordination, 3) strong metal-oxygen bonds, and 4) rigid polyhedra that remain practically unchanged on heating. Example structures showing NTE include: the $A_2M_3O_{12}$ family[9, 10, 19, 20, 26], the AX_2O_7 family[27-30], the AM_2O_8 family[8, 12, 31-33], the AMO_5 family[34, 35], and the AO_2 silicates and aluminophosphates (zeolites).[36-40] Additionally, it is

known that some members of the MX_3 family[41], which are frameworks constructed from corner-sharing octahedra (e.g ReO_3, NbO_2F, TaO_2F, and ScF_3), show low and negative thermal expansion.[41-45] This chapter will focus on the $A_2M_3O_{12}$, AX_2O_7, and AM_2O_8 families.

1.2.1 The $A_2M_3O_{12}$ Family

The $A_2M_3O_{12}$ (A = a variety of trivalent cations, Zr^{4+}, and Hf^{4+}; M = W, Mo, P) family of materials is interesting because some orthorhombic phases exhibit anisotropic negative thermal expansion.[9, 10, 18-20, 26, 46-48] The structure consists of corner sharing polyhedra, where A is in an octahedral environment surrounded by oxygen atoms, and M is in a tetrahedral environment of oxygen atoms. Figure 1.4 below shows the general crystal structure for members belonging to this family.

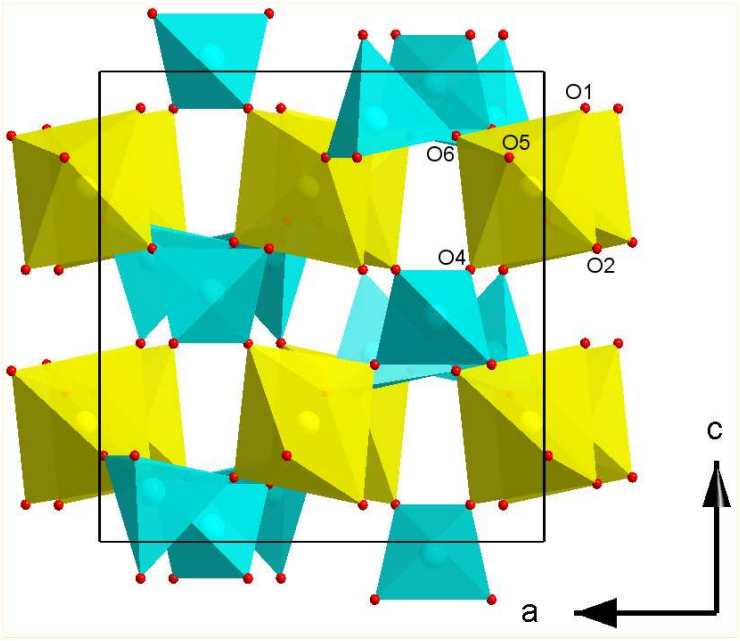

Figure 1.4. Crystal Structure of $Sc_2Mo_3O_{12}$, viewed down the b axis. Framework consists of ScO_6 octahedra (yellow) and MoO_4 tetrahedra (turquoise).

$Sc_2(WO_4)_3$ was the first material in this family known to exhibit NTE, followed shortly by $Sc_2(MoO_4)_3$.[9, 49] While many other materials with trivalent A cations exhibit anisotropic NTE, substitution with tetravalent Zr and Hf on the A site and PO_4 for charge balance, giving $Zr_2(PO_4)_2(WO_4)$ and $Zr_2(PO_4)_2(MoO_4)$, also leads to NTE.[9, 11] Other substitutions that are reported to exhibit the same structure are $(HfMg)(WO_4)_3$[50-52] and $Zr_2(PO_4)_2(SO_4)$.[53]

Measurements of NTE by dilatometer experiments and diffraction methods on members of the $A_2M_3O_{12}$ family have led to disagreements in the calculated expansion coefficients, suggesting an intrinsic and extrinsic contribution to the negative thermal expansion.[11] The extrinsic contribution to the NTE results from microcracking in the material due to anisotropic thermal expansion. When microcracking occurs, the apparent CTE may vary between temperature cycles.

1.2.2 The AX_2O_7 Family

Crystal structures of the AX_2O_7 family have been studied as early as 1935.[54] In this family, A is usually a tetravalent cation (Si, Ti, Ge, Zr, Nb, Mo, Sn, Hf, W, Re, Pb, Ce, Th, U, or Pu) in an octahedral environment, while X is a pentavalent atom (P, As, or V) in a tetrahedral environment.[13, 29, 54-65] The X_2O_7 group is formed through a bridging oxygen between a pair of tetrahedra resulting in a crystal structure ideally similar to that in Figure 1.5.

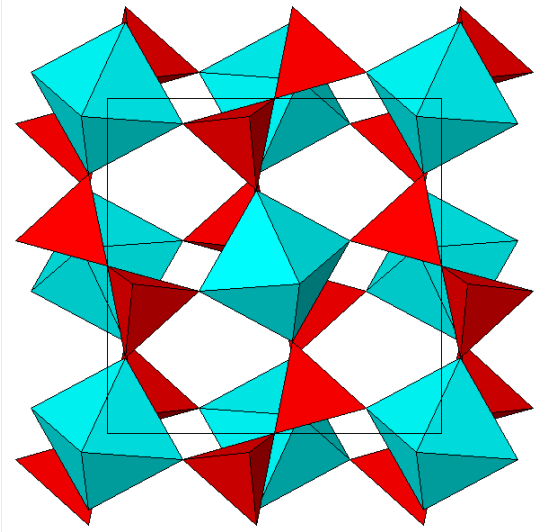

Figure 1.5. Crystal structure of ZrP_2O_7 above its phase transition temperature in space group *Pa-3*. ZrO_6 octahedra are shown in blue while PO_4 tetrahedra are shown in red.

At high temperatures, most of these materials crystallize in space group *Pa-3,* resulting in isotropic thermal expansion. However, at lower temperatures some of the members of this family exhibit a 3 x 3 x 3 superstructure, including TiP_2O_7[66, 67], ZrP_2O_7[28], SiP_2O_7[68], GeP_2O_7[64], HfV_2O_7[69], and ZrV_2O_7[29, 30, 70]. The superstructure in these materials results from the V-O-V, and P-O-P linkages, which at high temperature have average bond angles of 180º. At lower temperatures, these links adopt an ordered bent arrangement leading to the formation of the superstructure.

Thermal expansion studies of these materials have shown that materials containing small cations, like GeP_2O_7[64] and TiP_2O_7,[71] exhibit positive thermal expansion at all temperatures. Material containing larger ions, such as CeP_2O_7[13], UP_2O_7[72], and ThP_2O_7[73] show NTE at some temperatures. Additionally, when the P_2O_7 group is replaced with As_2O_7 or V_2O_7 as in $ZrAs_2O_7$[74] or HfV_2O_7[69], the larger tetrahedral environment increases the size of the framework. ZrV_2O_7[27] and HfV_2O_7[69] have been shown to exhibit NTE at some temperatures.

1.2.3 The AM_2O_8 Family

Members of the AM_2O_8 (A = Hf and Zr; M = Mo, W) family have been studied since the discovery of ZrW_2O_8 in 1959.[6] In this family, A is a tetravalent cation in an octahedral environment of oxygen atoms, while M is in a tetrahedral environment surrounded by oxygen atoms. Each tetrahedron bridges three AO_6 octahedra, with the fourth oxygen atom free within the structure (see Figure 1.6).[8]

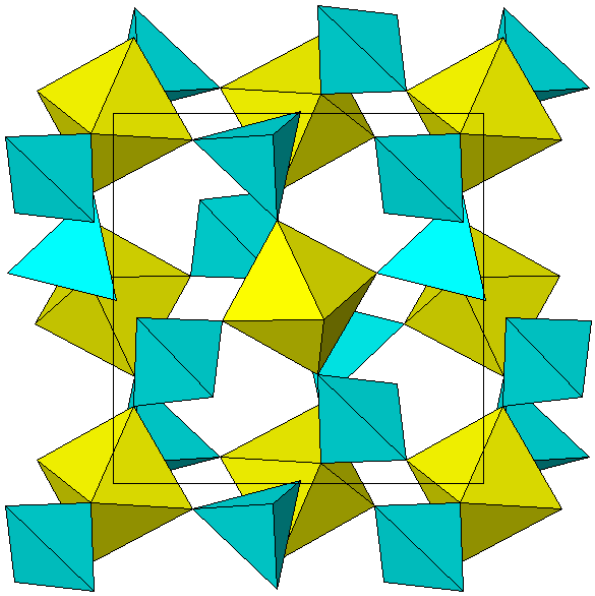

Figure 1.6. Crystal structure of α-ZrW_2O_8 in space group $P2_13$. ZrO_6 octahedra are represented in yellow and WO_4 tetrahedra in blue.

ZrW_2O_8 has been found to exhibit NTE up to its decomposition at 1050 K.[31] α-ZrW_2O_8 crystallizes in space group *P2₁3* at room temperature, and undergoes a cubic to cubic phase transition at 430 K to form β-ZrW_2O_8 in space group *Pa-3*.[75] The cubic form of $ZrMo_2O_8$, which has the same structure as β-ZrW_2O_8, was first synthesized by our research group in 1998.[12] Prior to this, $ZrMo_2O_8$ was only known to exist as monoclinic (*C2/c*)[76, 77] and trigonal (*P-3c*)[77-79] polymorphs. Cubic $ZrMo_2O_8$ crystallizes in the centro-symmetric space group *Pa-3,* and does not exhibit a phase transition from lower to higher symmetry on heating as observed for ZrW_2O_8.[12] It is stable up to 673 K and has a thermal expansion coefficient of -5.0 x 10^{-6} from 11 to 573 K.[12] Above 673 K, the material undergoes an irreversible phase transition to become the trigonal polymorph.

1.3 High Pressure and Negative Thermal Expansion

Materials exhibiting negative thermal expansion have potential for application in composites.[80-83] During their fabrication, there is a possibility of exposure to above ambient pressures, resulting in either a crystalline to crystalline phase transition[75, 84-87] or a crystalline to amorphous phase transition, otherwise known as pressure induced amorphization (PIA).[84, 88-94] Phase transitions occur on compressing these types of frameworks due to their low density. As pressure is applied to the material, the rigid polyhedral units tilt within the void space decreasing the volume and therefore increasing the density of the system.[94] Alteration of the material's crystal structure via phase transition, may result in a change of its thermal expansion characteristics. As NTE materials can be used in composites, it is essential to examine how these materials behave under pressure.

The open frameworks of oxides that exhibit NTE allows for a high compressibility and thus a low bulk modulus. For example, the bulk moduli for cubic ZrW_2O_8[95], cubic ZrV_2O_7, [96] cubic NbO_2F, [97] and orthorhombic $Zr_2(PO_4)_2(WO_4)$[98] were found to be 72.5, 18.0, 24.8, and 61.3 GPa, respectively. These are low when compared to materials such as γ-Fe_2O_3[99](hematite) and $MgCO_3$[100] (magnesite) which have bulk moduli of 165 and 117 GPa respectively. The NTE framework bulk moduli are more comparable to those for CsCl,[101] NaCl,[101] and LiF[102] which range from 18.1 to 65.3 GPa. This high compressibility is directly related to the low density of the NTE frameworks. Cubic ZrW_2O_8 has a density of 5.08 g/cm^3 while its component oxides, ZrO_2 and WO_3, have densities of 5.89 and 7.16 g/cm^3 respectively.

Upon compression, crystalline to crystalline phase transitions have been reported for many NTE materials including cubic ZrW_2O_8,[75, 86, 103-106] cubic $ZrMo_2O_8$,[107, 108] cubic HfW_2O_8,[86, 88] cubic $HfMo_2O_8$,[108] cubic ZrV_2O_7,[96] $Sc_2Mo_3O_{12}$,[109] $Sc_2W_3O_{12}$,[110] $Al_2W_3O_{12}$,[111] TaO_2F,[112] and NbO_2F.[112] As α-ZrW_2O_8 transforms to γ-ZrW_2O_8 in a cubic to orthorhombic transition at 0.21 GPa, the coefficient of NTE decreases by approximately one order of magnitude. The change in the thermal expansion coefficient under pressure significantly limits the application of this material in composites.

Pressure-induced amorphization has been reported for cubic ZrW_2O_8,[89] cubic $ZrMo_2O_8$,[84] $Sc_2Mo_3O_{12}$,[113] $Sc_2W_3O_{12}$,[114] and $Lu_2W_3O_8$,[115] and may be caused by the uncorrelated tilting of the polyhedral units, but other studies have shown that in materials such as ZrW_2O_8 the amorphization may involve an increase in cation coordination number. Studies on this material have shown that when heated under pressure, the coordination of the zirconium atom goes from six to a "6+1" coordination.[107] The change

in coordination suggested, that under pressure, the tungstate tetrahedra in cubic ZrW_2O_8 are unstable and they may be attempting to decompose to $ZrO_2 + WO_3$.

Additionally, there have been studies performed to determine the effect of pressure on the thermal expansion coefficient of materials. While pressure can cause crystalline to crystalline transition and PIA, the application of pressure may also directly affect the coefficient of thermal expansion. Recent work on the NTE material $Zn(CN)_2$[116] by Chapman *et al.* has shown that on increasing the pressure from 0.0 to 0.4 GPa, the linear thermal expansion coefficient goes from -17.4(2) x 10^{-6} K^{-1} to -19.4(2) x 10^{-6} K^{-1}.[116] This work showed that $Zn(CN)_2$ becomes softer upon compression. The changes in the linear coefficient of thermal expansion with pressure are related to the temperature dependence of the bulk modulus:[117]

$$\left(\frac{\partial \alpha_V}{\partial P}\right)_T = \frac{1}{K^2}\left(\frac{\partial K}{\partial T}\right)_P \tag{4}$$

where K is the bulk modulus and α_V is the volume coefficient of thermal expansion.

1.4 Goals of This Thesis

The main goal of this thesis is to determine how chemical changes in NTE frameworks affect the thermal expansion properties of the individual materials and collectively add to the knowledge of what is known about these frameworks. Firstly, we will examine the material $Zr_2(PO_4)_2(SO_4)$,[53] a member of the $A_2M_3O_{12}$ framework family, and determine if the substitution of sulfate in place of molybdate or tungstate has a significant effect on the thermal expansion characteristics of the material. We will then determine how the application of pressure affects its analogue $Hf_2(PO_4)_2(SO_4)$. We will then attempt to synthesize PbP_2O_7, a member of the AX_2O_7 family and characterize the

material. Finally, we are going to discuss how temperature and pressure affect the local structure of the NTE material α-$ZrMo_2O_8$.

1.5 References

1. Bruesch, P., *Phonons: Theory and Experiments*. Springer Verlag: Berlin, Germany, 1982; Vol. 1.

2. Roy, R.; Agrawal, D. K.; McKinstry, H. A., Very Low Thermal Expansion Coefficient Materials. *Annu. Rev. Mater. Sci.* **1989,** 19, 59-81.

3. Hummel, F. A., Thermal expansion properties of natural lithia minerals. *Foote Prints* **1948,** 20, 3-11.

4. Hummel, F. A., Thermal Expansion Properties of Some Synthetic Lithia Minerals. *J. Am. Ceram. Soc.* **1951,** 34, 235-239.

5. Boilot, J. P.; Salanie, J. P.; Desplanches, G.; Potier, D. L., Phase Transformation in $Na_{1+x}Si_xZr_2P_{3-x}O_{12}$ Compounds. *Mat. Res. Bull.* **1979,** 14, 1469-1477.

6. Graham, J.; Wadsley, A. D.; Weymouth, J. H.; Williams, L. S., A New Ternary Oxide, ZrW_2O_8. *J. Am. Ceram. Soc.* **1959,** 42, 570.

7. Sleight, A. W.; Thundathil, M. A.; Evans, J. S. O. Negative Thermal Expansion Materials. U. S. Patent 5,514,360, May 7, 1996, 1995.

8. Evans, J. S. O.; Mary, T. A.; Vogt, T.; Subramanian, M. A.; Sleight, A. W., Negative Thermal Expansion in ZrW_2O_8 and HfW_2O_8. *Chem. Mater.* **1996,** 8, 2809-2823.

9. Evans, J. S. O.; Mary, T. A.; Sleight, A. W., Negative Thermal Expansion in a Large Molybdate and Tungstate Family. *J. Solid State Chem.* **1997,** 133, 580-583.

10. Evans, J. S. O.; Mary, T. A.; Sleight, A. W., Negative Thermal Expansion in $Sc_2(WO_4)_3$. *J. Solid State Chem.* **1998,** 137, 148-160.

11. Mary, T. A.; Sleight, A. W., Bulk thermal expansion for tungstate and molybdates of the type $A_2M_3O_{12}$. *J. Mater. Res.* **1999,** 14, 912-915.

12. Lind, C.; Wilkinson, A. P.; Hu, Z.; Short, S.; Jorgensen, J. D., Synthesis and Properties of the Negative Thermal Expansion Material Cubic Zirconium Molybdate. *Chem. Mater.* **1998,** 10, 2335-2337.

13. White, K. M.; Lee, P. L.; Chupas, P. J.; Chapman, K. W.; Payzant, E. A.; Jupe, A. C.; Bassett, W. A.; Zha, C. S.; Wilkinson, A. P., Synthesis, Symmetry, and Physical Properties of Cerium Pyrophosphate. *Chem. of Mater.* **2008,** 20, 3728-3734.

14. Pryde, A. K. A.; Hammonds, K. D.; Dove, M. T.; Heine, V.; Gale, J. D.; Warren, M. C., Origin of the Negative Thermal Expansion in ZrW_2O_8 and ZrV_2O_7. *J. Phys. Condens. Matter* **1996,** 8, 10973-10982.

15. Varga, T.; Wilkinson, A. P.; Haluska, M.; Payzant, E. A., Preparation and thermal expansion of $(M^{III}_{0.5}M'^{V}_{0.5})P_2O_7$ with the ZrP_2O_7 structure. *J. Solid State Chem.* **2005,** 178, 3541-3546.

16. Sleight, A. W., Thermal Contraction. *Endeavour* **1995,** 19, 64-68.

17. Sleight, A. W., Compounds that Contract on Heating. *Inorg. Chem.* **1998,** 37, 2854-2860.

18. Evans, J. S. O.; Mary, T. A.; Sleight, A. W., Negative thermal expansion materials. *Physcia B* **1998,** 241-243, 311-316.

19. Forster, P. M.; Yokochi, A.; Sleight, A. W., Enhanced Negative Thermal Expansion in $Lu_2W_3O_{12}$. *J. Solid State Chem.* **1998,** 140, 157-158.

20. Forster, P. M.; Sleight, A. W., Negative thermal expansion in $Y_2W_3O_{12}$. *Int. J. Inorg. Mater.* **1999,** 1, 123-127.

21. Balashov, D. B.; Orlov, V. P., Thermal anomaly of water. I. Regional boundaries. Entropy. Heat capacities. *Zh. Fiz. Khim.* **1983,** 57, 2465-2468.

22. Scheel, K., Experiments on the Expansion of Solids and Measurements of Quartz in the Direction of the Principal Axis, Platinum, Palladium, and Quartz-glass, to the Temperature of Liquid Air. *Ber. physik Ges.* **1907,** 5, 3-23.

23. David, W. I. F.; Evans, J. S. O.; Sleight, A. W., Direct evidence for a low-frequency phonon mode mechanism in the negative thermal expansion compound ZrW_2O_8. *Europhys. Lett.* **1999,** 46, 661-666.

24. Yamamura, Y.; Nakajima, N.; Tsuji, T.; Iwasa, Y.; Saito, K.; Sorai, M., Heat capacity and Gruneisen functions of negative thermal expansion compound HfW_2O_8. *Solid State Commun.* **2002,** 121, 213-217.

25. Wang, K.; Reeber, R. R., Mode Gruneisen parameters and negative thermal expansion of cubic ZrW_2O_8 and $ZrMo_2O_8$. *Appl. Phys. Lett.* **2000,** 76, 2203-2204.

26. Woodcock, D. A.; Lightfoot, P.; Ritter, C., Negative Thermal Expansion in $Y_2(WO_4)_3$. *J. Solid State Chem.* **2000,** 149, 92-98.

27. Korthuis, V.; Khosrovani, N.; Sleight, A. W.; Roberts, N.; Dupree, R.; Warren, W. W., Negative Thermal Expansion and Phase Transitions in the $ZrV_{2-x}P_xO_7$ Series. *Chem. Mater.* **1995,** 7, 412-417.

28. Khosrovani, N.; Korthuis, V.; Sleight, A. W.; Vogt, T., Unusual 180° P-O-P Bond Angles in ZrP_2O_7. *Inorg. Chem.* **1996,** 35, 485-489.

29. Evans, J. S. O.; Hanson, J. C.; Sleight, A. W., Room-Temperature Superstructure of ZrV_2O_7. *Acta Cryst.* **1998,** B54, 705-713.

30. Withers, R. L.; Evans, J. S. O.; Hanson, J.; Sleight, A. W., An *In Situ* Temperature-Dependent Electron and X-ray Diffraction Study of Structural Phase transitions in ZrV_2O_7. *J. Solid State Chem.* **1998,** 137, 161-167.

31. Mary, T. A.; Evans, J. S. O.; Vogt, T.; Sleight, A. W., Negative Thermal Expansion from 0.3 to 1050 Kelvin in ZrW_2O_8. *Science* **1996,** 272, 90-92.

32. Closmann, C.; Sleight, A. W.; Haygarth, J. C., Low-temperature synthesis of ZrW2O8 and Mo-substituted ZrW2O8. *J. Solid State Chem.* **1998,** 139, 424-426.

33. Kameswari, U.; Sleight, A. W.; Evans, J. S. O., Rapid synthesis of ZrW_2O_8 and related phases, and structure refinement of $ZrWMoO_8$. *Int. J. Inorg. Mater.* **2000,** 2, 333-337.

34. Amos, T. G.; Yokochi, A.; Sleight, A. W., Phase Transitionand Negative Thermal Expansion in Tetragonal $NbOPO_4$. *J. Solid State Chem.* **1998,** 141, 303-307.

35. Amos, T. G.; Sleight, A. W., Negative Thermal Expansion in Orthorhombic $NbOPO_4$. *J. Solid State Chem.* **2001,** 160, 230-238.

36. Tschaufeser, P.; Parker, S. C., Thermal Expansion Behavior of Zeolites and $AlPO_4$s. *J. Phys. Chem.* **1995,** 99, 10609-10615.

37. Attfield, M. P.; Sleight, A. W., Exceptional Negative Thermal Expansion in $AlPO_4$-17. *Chem. Mater.* **1998,** 10, 2013-2019.

38. Attfield, M. P.; Sleight, A. W., Strong negative thermal expansion in siliceous faujasite. *Chem. Commun.* **1998**, 601-602.

39. Woodcock, D. A.; Lightfoot, P.; Ritter, C., Mechanism of low thermal expansion in the cation-ordered Nasicon structure. *Chem. Commun.* **1998**, 107-108.

40. Woodcock, D. A.; Lightfoot, P.; Villaescusa, L. A.; Díaz-Cabañas, M.-J.; Camblor, M. A.; Engberg, D., Negative Thermal Expansion in the Siliceous Zeolites Chabazite and ITQ-4: A Neutron Powder Diffraction Study. *Chem. Mater.* **1999,** 11, 2508-2514.

41. Frevel, L. K.; Rinn, H. W., The Crystal Structure of NbO_2F and TaO_2F. *Acta Crystallogr.* **1956,** 9, 626-627.

42. Chatterji, T.; Hansen, T. C.; Brunelli, M.; Henry, P. F., Negative thermal expansion of ReO3 in the extended temperature range. *Appl. Phys. Lett.* **2009,** 94, 24.

43. Dapiaggi, M.; Fitch, A. N., Negative (and very low) thermal expansion in ReO3 from 5 to 300 K. *J. Appl. Crystallogr.* **2009,** 42, 253-258.

44. Rodriguez, E. E.; Llobet, A.; Proffen, T.; Melot, B. C.; Seshadri, R.; Littlewood, P. B.; Cheetham, A. K., The role of static disorder in negative thermal expansion in ReO3. *J. Appl. Phys.* **2009,** 105, 11.

45. Tao, J. Z.; Sleight, A. W., Very low thermal expansion in TaO_2F. *J. Solid State Chem.* **2003,** 173, 45-48.

46. Sleight, A. W., Negative thermal expansion materials. *Current Opinion in Solid State and Materials Science* **1998,** 3, 128-131.

47. Sleight, A. W., Isotropic Negative Thermal Expansion. *Ann. Rev. Mater. Sci.* **1998,** 28, 29-43.

48. Imanaka, N.; Hiraiwa, M.; Adachi, G.; Dabkowska, H.; Dabkowski, A., Thermal contraction behavior in $Al_2(WO_4)_3$ single crystal. *J. Cryst. Growth* **2000,** 200, 176-179.

49. Evans, J. S. O.; Mary, T. A., Structural Phase Transitions and negative thermal expansion in $Sc_2(MoO_4)_3$. *Int. J. Inorg. Mater.* **2000,** 2, 143-151.

50. Suzuki, T.; Omote, A., Negative Thermal Expansion in $(HfMg)(WO_4)_3$. *J. Am. Ceram. Soc.* **2004,** 87, 1365-1367.

51. Suzuki, T.; Omote, A., Zero thermal expansion in $(Al\text{-}2x(HfMg)(1\text{-}x))(WO_4)_3$. *J. Am. Ceram. Soc.* **2006,** 89, 691-693.

52. Suzuki, T.; Omote, A., Pseudo binary HfW_2O_8-$MgWO_4$ thermal expansion control system. *J. Ceram. Soc. Jap.* **2006,** 114, 833-837.

53. Piffard, Y.; Verbaere, A.; Kinoshita, M., Beta-$Zr_2(PO_4)_2(SO_4)$- A Zirconium Phosphato-Sulfate With A $Sc_2(WO_4)_3$ Structure - A Comparison Between Garnet, NAISICON, and $Sc_2(WO_4)_3$ Structure Types. *J. Solid State Chem.* **1987,** 71, 121-130.

54. Levi, G. R.; Peyronel, G., Struttura Cristallografica del Gruppo Isomorfo (Si^{4+}, Ti^{4+},Zr^{4+},Sn^{4+},Hf^{4+})P_2O_7. *Z. Kristallogr.* **1935,** 92, 190-209.

55. Bjorklund, C. W., The Preparation of PuP_2O_7 and $PuPO_4$. *J. Am. Chem. Soc.* **1958,** 79, 6347-6350.

56. Hagman, L.-O.; Kierkegaard, P., Note on the Structures of $M^{IV}P_2O_7$ (M^{IV} = Ge, Zr, and U). *Acta Chem. Scand.* **1969,** 23, 327-328.

57. Liebau, V. F.; Bissert, G.; Koppen, N., Synthese und kristallographische Eigenschaften einiger Phasen im System SiO_2-P_2O_5. *Z. Anorg. Alleg. Chem.* **1968,** 359, 113-134.

58. Huang, C.-H.; Knop, O.; Othen, D. A., Pyrophosphates of Tetravalent Elements and a Mossbauer Study of SnP_2O_7. *Can. J. of Chem.* **1975,** 53, 79-91.

59. Vollenkle, H.; Wittmann, A.; Nowotny, H., Uber Diphosphate vom Typ Me(IV)P_2O_7. *Monatsh. Chem.* **1963,** 94, 956-963.

60. Burdese, A.; Lucco Borlera, M., Sul sistema tra i pirofosfati di uranio e torio. *Ann. Chim. (Rome)* **1963,** 53, 333-343.

61. Baran, E. J.; Gentil, L. A.; Pedregosa, J. C.; Aymonino, P. J., Divanadates of Thorium. *Z. Anorg. Allg. Chem.* **1974,** 410, 301-312.

62. Baran, E. J., The unit cell of hafnium divanadate. *J. Less Common Met.* **1976,** 46, 343-345.

63. Onken, H., Uber Zirkonpyroarsenat. *Naturwissenschaften* **1965,** 52, 344.

64. Losilla, E. R.; Cabeza, A.; Bruque, S.; Aranda, M. A. G.; Sanz, J.; Iglesias, J. E.; Alonso, J. A., Syntheses, Structures, and Thermal Expansion of Germanium Pyrophosphates. *J. Solid State Chem.* **2001,** 156, 213-219.

65. Peyronel, G., The existence, properties and crystalline structure of $Pb^{IV}P_2O_7$. *Gazz. Chim. Ital.* **1939,** 69, 254-262.

66. Sanz, J.; Iglesias, J. E.; Soria, J.; Losilla, E. R.; Aranda, M. A. G.; Bruque, S., Structural Disorder in the Cubic 3x3x3 Superstructure of TiP_2O_7. XRD and NMR Study. *Chem. Mater.* **1997,** 9, 996-1003.

67. Norberg, S. T.; Svensson, G.; Albertsson, J., A TiP_2O_7 superstructure. *Acta Crystallogr., Sect. C* **2001,** 57, 225-227.

68. Tillmans, E.; Gebert, W.; Baur, W. H., Computer Simulations of Crystal Structures Applied to the Solution of the Superstructure of Cubic Silicondiphosphate. *J. Solid State Chem.* **1973,** 7, 69-84.

69. Turquat, C.; Muller, C.; Nigrelli, E.; Leroux, C.; Soubeyroux, J.-L.; Nihoul, G., Structural investigation of temperature-induced phase transitions in HfV_2O_7. *The Euro. Phys. J. Appl. Phys.* **2000,** 10, 15-27.

70. Khosrovani, N.; Sleight, A. W.; Vogt, T., Structure of ZrV_2O_7 from -263 to 470 ^oC. *J. Solid State Chem.* **1997,** 132, 355-360.

71. Taylor, D., Thermal Expansion Data: XIII Complex Oxides with chain, ring and layer structures and apatites. *Br. Ceram. Trans. J.* **1988,** 87, 88-95.

72. Kirchner, H. P.; Merz, K. M.; Brown, W. R., Thermal Expansion of Uranium Pyrophosphate and Ceramic Bodies in the System UO_2-P_2O_7. *J. Am. Ceram. Soc.* **1963,** 46, 137-141.

73. Laud, K.; Hummel, F. A., The system ThO_2-P_2O_5. *J. Am. Ceram. Soc.* **1971,** 54, 296-298.

74. Karyakin, N. V.; Ghernorukov, G. N.; Bondareva, A. S., Thermochemistry of High-Temperature Phases of Zirconium and Hafnium Pyrophosphates and Pyroarsenates. *Russ. J. Inorg. Chem.* **2001,** 46, 701-704.

75. Evans, J. S. O.; Hu, Z.; Jorgensen, J. D.; Argyriou, D. N.; Short, S.; Sleight, A. W., Compressibility, Phase Transitions, and Oxygen Migration in Zirconium Tungstate, ZrW_2O_8. *Science* **1997,** 275, 61-65.

76. Auray, M.; Quarton, M., Revised Crystal Data of $Zr(MoO_4)_2$, L.T. Form. *Powder Diffraction* **1989,** 4, 29-30.

77. Auray, M.; Quarton, M.; Tarte, P., Crystal Data for Two Molybdates $M(MoO_4)_2$ with M = Zr, Hf. *Powder Diffraction* **1987,** 2, 36-38.

78. Auray, M.; Quarton, M.; Tarte, P., New Structure of High Temperature Zirconium Molybdate. *Acta Cryst.* **1986,** C42, 257-259.

79. Serezhkin, V. N.; Efremov, V. A.; Trunov, V. K., The Crystal Structure of α-$Zr(MoO_4)_2$, the High-temperature Modification of Zirconium Molybdate. *Russ. J. Inorg. Chem.* **1987,** 32, 1566-1570.

80. Wetherfold, R. C.; Wang, J., Tailoring thermal deformation by using layered beams. *Compos. Sci. Technol.* **1995,** 53, 1-6.

81. Fleming, D. A.; Lemaire, P. J.; Johnson, D. W. Temperature compensated optical fiber refractive index grating. EP 97-306798 19970902, 1998.

82. Fleming, D. A.; Johnson, D. W.; Lemaire, P. J. Article Comprising a Temperature Compensated Optical Fiber Refractive Index Grating. U. S. Patent 5,694,503, December 2, 1997.

83. Balch, D. K.; Dunand, D. C., Copper-Zirconium Tungstate Composites Exhibiting Low and Negative Thermal Expansion Influenced by Reinforcement Phase Transformations. *Metall. Mater. Trans. A* **2004,** 35A, 1159-1165.

84. Grzechnik, A.; Crichton, W. A., Structural transformations in cubic $ZrMo_2O_8$ at high pressures and high temperatures. *Solid State Sci.* **2002,** 4, 1137-1141.

85. Muthu, D. V. S.; Chen, B.; Wrobel, J. M.; Krogh Andersen, A. M.; Carlson, S.; Kruger, M. B., Pressure-induced phase transitions in α–$ZrMo_2O_8$. *Phys. Rev. B* **2002,** 65, 064101-1-5.

86. Jorgensen, J. D.; Hu, Z.; Short, S.; Sleight, A. W.; Evans, J. S. O., Pressure-induced cubic-to-orthorhombic phase transfromation in the negative thermal expansion material HfW_2O_8. *J. Appl. Phys.* **2001,** 89, 3184-3188.

87. Varga, T.; Wilkinson, A. P.; Lind, C.; Bassett, W. A.; Zha, C.-S., High pressure synchrotron x-ray powder diffraction study of $Sc_2Mo_3O_{12}$ and $Al_2W_3O_{12}$ *J. Phys.: Condens. Matter* **2005,** 17, 4271-4283.

88. Chen, B.; Muthu, D. V. S.; Liu, Z. X.; Sleight, A. W.; Kruger, M. B., High-pressure Raman and infrared study of HfW_2O_8. *Phys. Rev. B* **2001,** 64, 214111.

89. Perottoni, C. A.; de Jornada, J. A. H., Pressure-Induced Amorphization and Negative Thermal Expansion in ZrW_2O_8. *Science* **1998,** 280, 886-889.

90. Figueiredo, C. A.; Catafesta, J.; Zorzi, J. E.; Salvador, L.; Baumvol, I. J. R.; Gallas, M. R.; da Jornada, J. A. H.; Perottoni, C. A., Compression mechanism and pressure-induced amorphization of gamma-ZrW_2O_8. *Phys. Rev. B* **2007,** 76, 18.

91. Varga, T.; Wilkinson, A. P.; Jupe, A. C.; Lind, C.; Bassett, W. A.; Zha, C.-S., Pressure-induced amorphization of cubic ZrW_2O_8 studied in-situ and ex-situ by synchrotron x-ray absorption spectroscopy and diffraction. *Phys. Rev. B* **2005,** 72, 024117-1-10.

92. Varga, T.; Wilkinson, A. P.; Lind, C.; Basset, W. A.; Zha, C.-S., Pressure-induced amorphization of cubic $ZrMo_2O_8$ studied in-situ by x-ray absorption spectroscopy and diffraction. *Solid State Commun.* **2005,** 135, 739-744.

93. Arora, A. K.; Yagi, T.; Miyajima, N.; Mary, T. A., Amorphization and decomposition of scandium molybdate at high pressure. *J. Appl. Phys.* **2005,** 97, 1-8.

94. Yamanaka, T.; Nagai, T.; Tsuchiya, T., Mechanism of pressure-induced amorphization. *Z. Krist.* **1997,** 212, 401-410.

95. Jorgensen, J. D.; Hu, Z.; Teslic, S.; Argyriou, D. N.; Short, S.; Evans, J. S. O.; Sleight, A. W., Pressure -induced cubic-to-orthorhombic phase transition in ZrW_2O_8. *Phys. Rev. B* **1999,** 59, 215-225.

96. Carlson, S.; Krogh Andersen, A. M., High-pressure properties of TiP_2O_7, ZrP_2O_7 and ZrV_2O_7. *J. Appl. Cryst.* **2001,** 34, 7-12.

97. Carlson, S.; Larsson, A.-K.; Rohrer, F. E., High-pressure transformations of NbO_2F. *Acta Crystallogr., Sect. B* **2000,** 56, 189-196.

98. Cetinkol, M.; Wilkinson, A. P., Pressure Dependence of Negative Thermal Expansion in $Zr_2(WO_4)(PO_4)_2$. *Solid State Commun.* **2009,** 149, 421-424.

99. Jiang, J. Z.; Olsen, J. S.; Gerward, L.; Morup, S., Enhanced bulk modulus and reduced transition pressure in γ-Fe_2O_3 nanocrystals. *Europhys. Lett.* **1998,** 44, 620-626.

100. Ross, N. L., The equation of state and high-pressure behavior of magnesite. *Am. Mineral.* **1997,** 82, 682-688.

101. Decker, D. L., High-Pressure Equation of State for NaCl, KCl, and CsCl. *J. Appl. Phys.* **1971,** 42, 3239-3244.

102. Fei, Y., Thermal Expansion. In *Mineral Physics and Crystallography: A Handbook of Physical Constants*, American Geophysical Union: Washington, DC, 1995.

103. Ravindran, T. R.; Arora, A. K.; Mary, T. A., High Pressure Behavior of ZrW_2O_8: Gruneisen Parameter and Thermal Properties. *Phys. Rev. Lett.* **2000,** 84, 3879-3882.

104. Ravindran, T. R.; Arora, A. K.; Mary, T. A., Erratum: High Pressure Behavior of ZrW_2O_8: Gruneisen Parameter and Thermal Properties. *Phys. Rev. Lett.* **2000,** 85, 225.

105. Hu, Z.; Jorgensen, J. D.; Teslic, S.; Short, S.; Argyriou, D. N.; Evans, J. S. O.; Sleight, A. W., Pressure-induced phase transformation in ZrW_2O_8 - Compressibility and thermal expansion of the orthorhombic phase. *Physica B* **1998,** 241-243, 370-372.

106. Gallardo-Amores, J. M.; Amador, U.; Moran, E.; Alario-Franco, M. A., XRD study of ZrW_2O_8 versus temperature and pressure. *Int. J. Inorg. Mater.* **2000,** 2, 123-129.

107. Grzechnik, A.; Crichton, W. A.; Syassen, K.; Adler, P.; Mezouar, M., A New Polymorph of ZrW_2O_8 Synthesized at High Pressures and High Temperatures. *Chemistry of Materials* **2001,** 13, 4255-4259.

108. Lind, C.; VanDerveer, D. G.; Wilkinson, A. P.; Chen, J.; Vaughan, M. T.; Weidner, D. J., New high pressure form of the negative thermal expansion materials zirconium molybdate and hafnium molybdate. *Chem. Mater.* **2001,** 13, 487-490.

109. Paraguassu, W.; Maczka, M.; Souza Filho, A. G.; Freire, P. T. C.; Mendes Filho, J.; Melo, F. E. A.; Macalik, L.; Gerward, L.; Staun Olsen, J.; Waskowska, A.; Hanuza, J., Pressure-induced structural transformations in the molybdate $Sc_2(MoO_4)_3$. *Phys. Rev. B* **2004,** 69, 094111-1-5.

110. Varga, T.; Wilkinson, A. P.; Lind, C.; Bassett, W. A.; Zha, C.-S., In-situ high pressure synchrotron x-ray diffraction study of $Sc_2W_3O_{12}$ at up to 10 GPa. *Phys. Rev. B* **2005,** 71, 214106-1-8.

111. Maczka, M.; Paraguassu, W.; Souza Filho, A. G.; Freire, P. T. C.; Mendes Filho, J.; Melo, F. E. A.; Hanuza, J., High-pressure Raman study of $Al_2(WO_4)_3$. *J. Solid State Chem.* **2004,** 177, 2002-2006.

112. Cetinkol, M.; Wilkinson, A. P.; Lind, C.; Bassett, W. A.; Zha, C.-S., High-pressure powder diffraction study of TaO_2F. *J. Phys. Chem. Solids* **2007,** 68, 611-616.

113. Arora, A. K.; Nithya, R.; Yagi, T.; Miyajima, N.; Mary, T. A., Two-stage amorphziation of scandium molybdate at high pressure. *Solid State Commun.* **2004,** 129, 9-13.

114. Secco, R. A.; Liu, H.; Imanaka, N.; Adachi, G., Pressure-induced amorphization in negative thermal expansion $Sc_2(WO_4)_3$. *J. Mater. Sci. Lett.* **2001,** 20, 1339-1340.

115. Liu, H.; Secco, R. A.; Imanaka, N.; Adachi, G., X-ray diffraction study of pressure induced amorphization in $Lu_2(WO_4)_3$. *Solid State Commun.* **2002,** 121, 177-180.

116. Chapman, K. W.; Chupas, P. J., Pressure Enhancement of Negative Thermal Expansion Behavior and Induced Framework Softening in Zinc Cyanide. *J. Am. Chem. Soc.* **2007,** 129, 10090-10091.

117. Touloukian, Y. S.; Kirby, R. K.; Taylor, R. E.; Lee, T. Y. R., *Thermal Expansion: Nonmetallic Solids*. Plenum: New York, 1970; Vol. 13.

CHAPTER 2

THERMAL EXPANSION PROPERTIES OF β-$Zr_2(PO_4)_2(SO_4)$, A PHASE BELONGING TO THE $A_2M_3O_{12}$ FAMILY OF CORNER SHARING FRAMEWORKS

2.1 Introduction

There has been much recent interest in materials exhibiting negative thermal expansion (NTE). Incorporation of materials exhibiting NTE can enable overall control of the thermal expansion in a composite.[1-8] Much of the recent work done on materials with unusual thermal expansion has focused on compounds of the types AM_2O_8 (A = Zr^{4+}, Hf^{4+}; M = Mo, W),[1, 2, 9-15] $A_2M_3O_{12}$ (A = a variety of trivalent cations, Zr^{4+} and Hf^{4+}; M = Mo, W, and P),[2, 16-26] and AX_2O_7 (A = Si^{4+}, Ti^{4+}, Ce^{4+}, Th^{4+}, U^{4+}, Zr^{4+}, Hf^{4+}, Sn^{4+}, Pb^{4+}, and Ge^{4+} and mixed valent M^{III}/M^{V} systems; X = P, V, and As) as many compositions from these structural families exhibit NTE.[5, 6, 27-30]

In the $A_2M_3O_{12}$ family, the first material tested to show NTE was $Sc_2(WO_4)_3$ followed closely by $Sc_2(MoO_4)_3$.[23, 24] These materials crystallize in the orthorhombic space group *Pnca* and exhibit anisotropic NTE.[23, 24] Further studies have found that substituting the trivalent cations allows the thermal expansion properties to be tuned. For example, the linear coefficient of thermal expansion changes from $\alpha = -11 \times 10^{-6}\ K^{-1}$ for $Sc_2(WO_4)_3$ to nearly zero on going to $Al_{1.68}Sc_{0.02}In_{0.30}W_3O_{12}$.[18] Other studies have shown

that when materials of this type undergo a phase transition from monoclinic to orthorhombic, the thermal expansion can change from positive to negative.[18]

Further substitutions in this system have produced NTE compositions such as $MgHf(WO_4)_3$, $Zr_2(PO_4)_2(MoO_4)$, and $Zr_2(PO_4)_2(WO_4)$. In the latter materials, tetravalent zirconium can be substituted in place of trivalent species when phosphates replace some molybdates or tungstates to maintain charge balance.[31] Since $Sc_2(WO_4)_3$, $Zr_2(PO_4)_2(MoO_4)$, and $Zr_2(PO_4)_2(WO_4)$ all crystallize in space group *Pnca*(60), and β-$Zr_2(PO_4)_2(SO_4)$ has been reported in *Pbcn* (60), we wish to determine how sulfate substitution, in the $A_2M_3O_{12}$ family of frameworks, affects the thermal expansion characteristics of this framework type.[32]

Materials containing both sulfate and phosphate are quite unusual. Examples include $CaAl_3(PO_4)(SO_4)(OH)_6$, $SrAl_3(PO_4)(SO_4)(OH)_6$, $PbFe_3(PO_4)(SO_4)(OH)_6$, $Pb_4(PO_4)_2(SO_4)$, $Cd_2Cu_2(PO_4)_2(SO_4)(H_2O)_5$, $Pb_2Cu(PO_4)(SO_4)(OH)$, and $Pb_3Sr(PO_4)_2(SO_4)$.[33-39] Our study of $Zr_2(PO_4)_2(SO_4)$ provides some additional insight into mixed phosphate/sulfates.

$Zr_2(PO_4)_2(SO_4)$ can be prepared by the reaction of zirconium phosphate gels with sulfuric acid.[40] While reactions of this variety were reported as early as 1947, this composition was first characterized in 1984 by Alamo and Roy.[40, 41] Based off of starting material ratios of zirconium and phosphorus in the zirconium phosphate gel, refluxing in sulfuric acid resulted in either α or β phase structures closely related to that of $NaZr_2(PO_4)_3$ (NZP).[42] Further studies by Piffard *et al*. concluded that β-$Zr_2(PO_4)_2(SO_4)$ crystallized in space group *Pbcn* (60), with a structure (see Figure 2.1) similar to that of $Sc_2W_3O_{12}$, not NZP.[32] Other studies performed on β-$Zr_2(PO_4)_2(SO_4)$ have shown that this

material does not exhibit photoluminescence and it is believed that the material is disordered.[43]

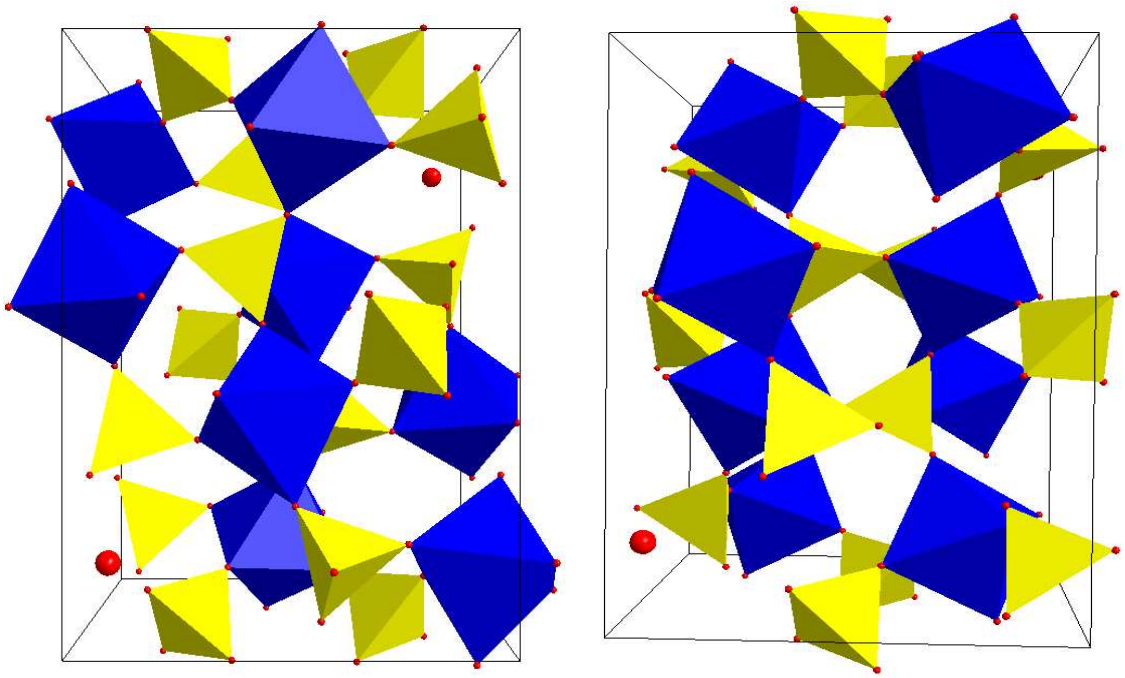

Figure 2.1. Crystal structure of β-$Zr_2(PO_4)_2(SO_4)$ viewed along the b (left) and c (right) axes. ZrO_6 octahedra are in blue and PO_4 and SO_4 tetrahedra are in yellow, while oxygen atoms are seen in red.

2.2 Experimental

2.2.1 Sample Preparation

$ZrO(NO_3)_2{\cdot}6H_2O$ (Aldrich), H_3PO_4 (Baker), and HNO_3 (Fisher) were used as purchased. A zirconium phosphate gel was made using a modification of the procedure reported by Piffard *et al.*[32] A solution of 1 M H_3PO_4 was added to a solution containing both 0.4 M $ZrO(NO_3)_2{\cdot}6H_2O$ and 0.1 M HNO_3 in a stoichiometric ratio of 10:4:1 for phosphorous, zirconium, and nitric acid. An open topped container of the resulting white

gel was placed in an oven and heated at 110 ºC for 1 h, followed by 150 ºC for an hour, and finally 200 ºC for 1 h under air producing a cake-like gel. The resulting material contained 0.17 g Zr per gram of gel and was ground using mortar and pestle and stored for subsequent use. The zirconium content of the dried gel was estimated from its final mass by assuming that all of the added zirconium was present in the gel.

Samples of $Zr_2(PO_4)_2(SO_4)$ were prepared by a modification of the procedure reported by Piffard *et al.*[32] H_2SO_4 (VWR) was used as purchased. In a Teflon-lined autoclave 12 mL of concentrated H_2SO_4 was added to ~1.0 g of the dried zirconium phosphate gel to form a suspension. After stirring the mixture, the autoclave was sealed and placed in an oven at 225 ºC. After four days, the oven was turned off and the autoclave was cooled to room temperature in the oven. The autoclave contained a clear solution over a white powder. The final product was recovered by filtration. It was washed with 2 x 15 mL H_2SO_4, followed by 2 x 15 mL acetonitrile, and finally air dried overnight.

2.2.2 Laboratory Powder X-ray Diffraction Measurements

Room temperature powder X-ray diffraction measurements were performed on a Scintag diffractometer with a copper tube and a Peltier cooled solid state detector. Data were collected over the range of 5-90º 2θ, at a rate of 2º/min.

2.2.3 Variable Temperature Synchrotron Experiments

$Zr_2(PO_4)_2(SO_4)$ samples were packed into a kapton capillary tube and mounted on a crystallographic goniometer head. Diffraction data were collected at the Advanced

Photon Source, Argonne National Lab, beam line 1-BM-C using x-rays with λ= .61848 Å. An Oxford Cryosystem's Cryostream 700 was used to ramp the sample temperature while x-ray data were acquired. 2D diffraction images were recorded on a MAR 345 detector. Each x-ray exposure lasted 45 s, followed by time to read the data off of the image plate totaling 140 s between exposures. During each exposure, the sample was rocked through a 20° range. The sample was oscillated to improve the powder average. Data were collected continuously while the sample was first cooled to 120 K at 6 K/min, as a lower temperature may have led to ice formation, then heated to 500 K, the upper temperature limit of the apparatus, at 3 K/min, cooled again to 120 K at 3 K/min, and finally reheated to 300 K at 6 K/min. The sample was held at temperature for 10 min between each heating and cooling segment.

FIT-2D was used to integrate the image plate data.[44] Reitveld analyses of the data were performed using the program GSAS with the EXPGUI interface.[45, 46]

2.2.4 Thermogravimetric Analysis Measurements

TGA measurement were performed on the Perkin Elmer TGA 7 Thermogravimetric Analyzer. Data were collected from 30-800 ºC at a rate of 3.3 ºC/min under a nitrogen atmosphere using a platinum pan as a sample holder.

2.2.5 Single Crystal Microdiffraction Experiment

Single crystal diffraction data were acquired for $Zr_2(PO_4)_2(SO_4)$ at a temperature of 95 K on a Bruker D8 diffractometer equipped with an Oxford Cryosystems nitrogen open flow apparatus using ChemMatCARS, Sector 15, Center for the Advanced Photon

Sources, University of Chicago at the APS, Argonne National Lab. Intensities of the reflections were recorded using a Bruker APEX II CCD. 30keV (λ = 0.41328 Å) x-rays were selected using a diamond (111) monochromator. The data were collected using Phi scans (0.5º) with several ω settings.

The data integration was done with reflection spot size optimization. Absorption corrections were made with the program SADABS (Bruker Diffractrometer, 2009). The structure was solved using direct methods procedure and refined by least-squares methods against F^2 using SHELXS-97 and SHELXL-97.[47, 48] All atoms were refined anisotropically.

2.2.6 Crystal Density Measurements

Density measurements for $Zr_2(PO_4)_2(SO_4)$ were performed using the flotation method.[49, 50] In a small vial, crystals of $Zr_2(PO_4)_2(SO_4)$ were added to liquid methylene iodide. The vial was then placed in a sonicator for 5 min to dislodge gas bubbles from the crystals. To the vial, dropwise, was added bromoform. Following the addition of each drop, the vial was sealed and shaken to generate a uniform solution. This procedure was repeated until the crystals neither floated to the top, or sank to the bottom of the solution. The density was calculated using the assumption that the solution was uniform throughout using the weight of the liquid in a 1.00 mL volumetric flask.

2.2.7 High Resolution Powder X-ray Diffraction

High resolution powder diffraction data were collected for $Zr_2(PO_4)_2(SO_4)$ at beamline 11-BM of the Advanced Photon Source, Argonne National Lab, using their 12-analyzer detector set-up.[51] 30 keV (λ = 0.413166 Å) x-rays were selected using a double-crystal monochromator. Lebail modeling of the data were performed using GSAS with the EXPGUI interface.[45, 46]

2.3 Results

2.3.1 Thermogravimetric Analysis

The thermogravimetric analysis (TGA) of $Zr_2(PO_4)_2(SO_4)$ from 30-800 ºC under a nitrogen atmosphere is shown in Figure 2.2. Calculations were based on the assumption that pure $Zr_2(PO_4)_2(SO_4)$ is found in the range of 150-370 ºC. From 30 ºC to 100 ºC, the material experiences a 0.5% weight loss, presumably, corresponding to the loss of water absorbed on the material's surface (0.13 mol H_2O). A second weight loss is observed for the material from 100-150 ºC, perhaps, corresponding to water loss/dehydroxylation from the crystal structure itself (0.30 mol H_2O). From this point the TGA curve plateaus and the material remains stable until 370 ºC, where the material begins a further weight loss. The sample loses weight rapidly from this point up to 500 ºC. The loss is equivalent to 0.26 mol SO_3, presumably, from the starting material. From this point the material undergoes a steady weight loss until 808.3 ºC, where the final weight of material is 92.42% of the initial mass measured inside of the instrument.

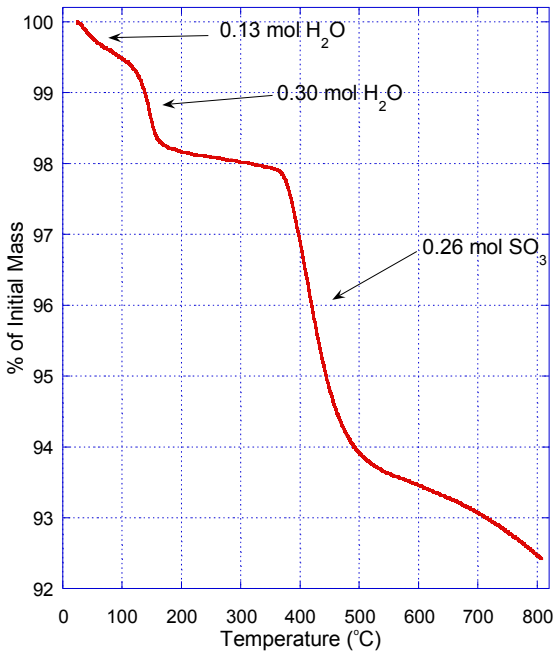

Figure 2.2. Thermogravimetric analysis of $Zr_2(PO_4)_2(SO_4)$. The sample was heated to 800 ºC at a rate of 3.3 ºC/min under a nitrogen atmosphere.

2.3.2 Variable Temperature Powder X-ray Diffraction Experiment

Figure 2.3 shows a Rietveld refinement to an x-ray diffraction pattern collected at 282 K during the variable temperature *in-situ* powder x-ray experiment that was describe in section 2.2.3. The *Pbcn* structural model proposed by Piffard *et al*.[32] gives reasonable agreement with these data.

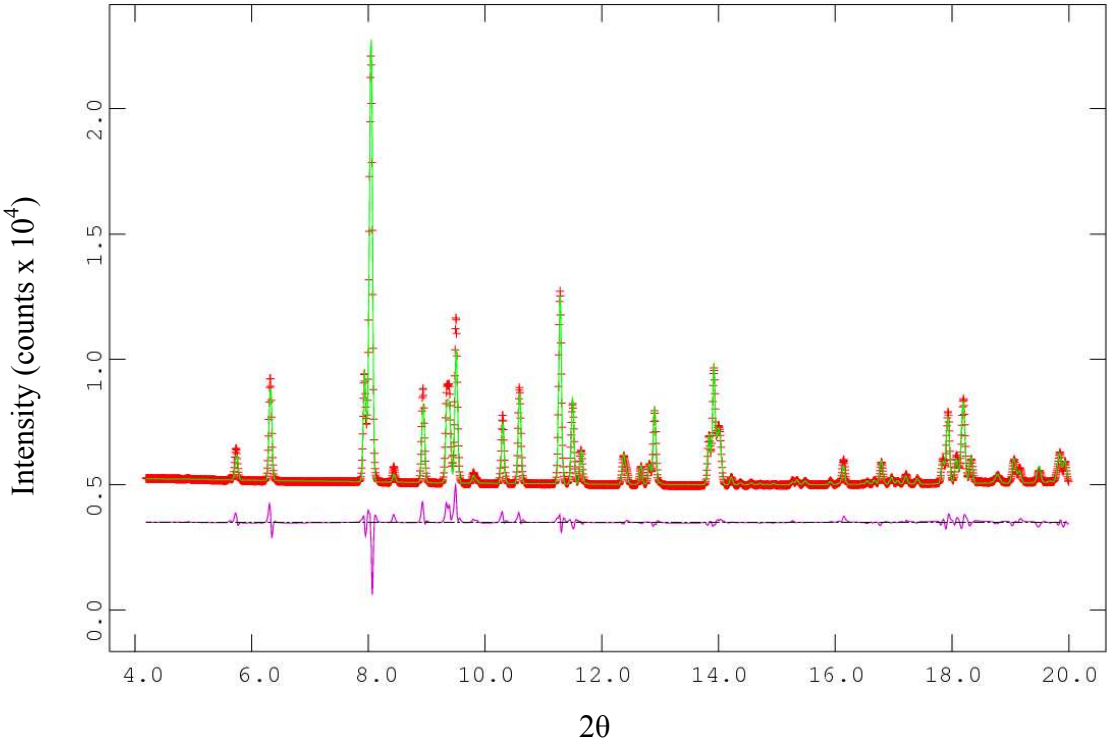

Figure 2.3. Powder x-ray diffraction pattern of $Zr_2(PO_4)_2(SO_4)$ taken at 282 K during variable temperature powder x-ray experiment at λ=0.61848 Å, in red, compared to the Rietveld model in space group *Pbcn* (green). The difference curve is shown in purple.

This model was used for Rietveld fits, using the sequential refinement feature of GSAS, to all of the diffraction patterns collected during the variable temperature measurement so that the material's lattice constants could be obtained as a function of temperature (see supplementary material Table S.1 and Figure 2.4). The temperature of the material was taken to be the average temperature during each exposure.

Figure 2.4a shows that lattice parameter *a* exhibits positive thermal expansion as it is initially heated from 120-500 K. From 120-360 K, *a* increases linearly from 12.3311(2) Å to 12.3531(2) Å. At 360 K there is a change of slope which is completed by 425 K. Thermal expansion then continues linearly until a maximum 12.3592(2) Å is obtained at 500 K. Upon the second cooling of the sample to 120 K, lattice parameter *a* shows almost linear thermal expansion to a minimum of 12.3256(2) Å, which is reversible on heating back to room temperature.

Figure 2.4b shows negative thermal expansion of lattice parameter *b*. As the sample is heated, *b* decreases steadily from 8.8566(2) Å to 8.8551(2) Å over the temperature range 120-360 K. At 360 K, *b* decreases more rapidly until a minimum is reached at 8.8524(2) Å at 500 K. As the sample is cooled for the second time to 120 K, *b* increases to a value of 8.8557(2) Å, this behavior is reversible on heating back to room temperature.

Figure 2.4c shows that lattice parameter *c* exhibits NTE as it is heated to 500 K. From 120-360 K *c* linearly decreases from 8.9395(2) Å to 8.9346(2) Å. At 360 K a change of slope is noticed and *c* further decreases to a minimum of 8.9309(2) Å at 500 K. During the second cooling *c* increases linearly to 8.9385(2) Å. This behavior is reversible on heating back to room temperature.

Figure 2.4d shows that the unit cell volume exhibits positive thermal expansion on heating from 120 to 360 K (the cell volume goes from 976.29(2) $Å^3$ to 977.34(2) $Å^3$). From 360-450 K the unit cell volume decreases to 977.03(2) $Å^3$ then resumes positive thermal expansion to 500 K where a volume of 977.11(3) $Å^3$ is observed. As the sample is cooled to 120 K the volume decreases linearly to a value of 975.65(2) Å, which is reversible on heating back to room temperature.

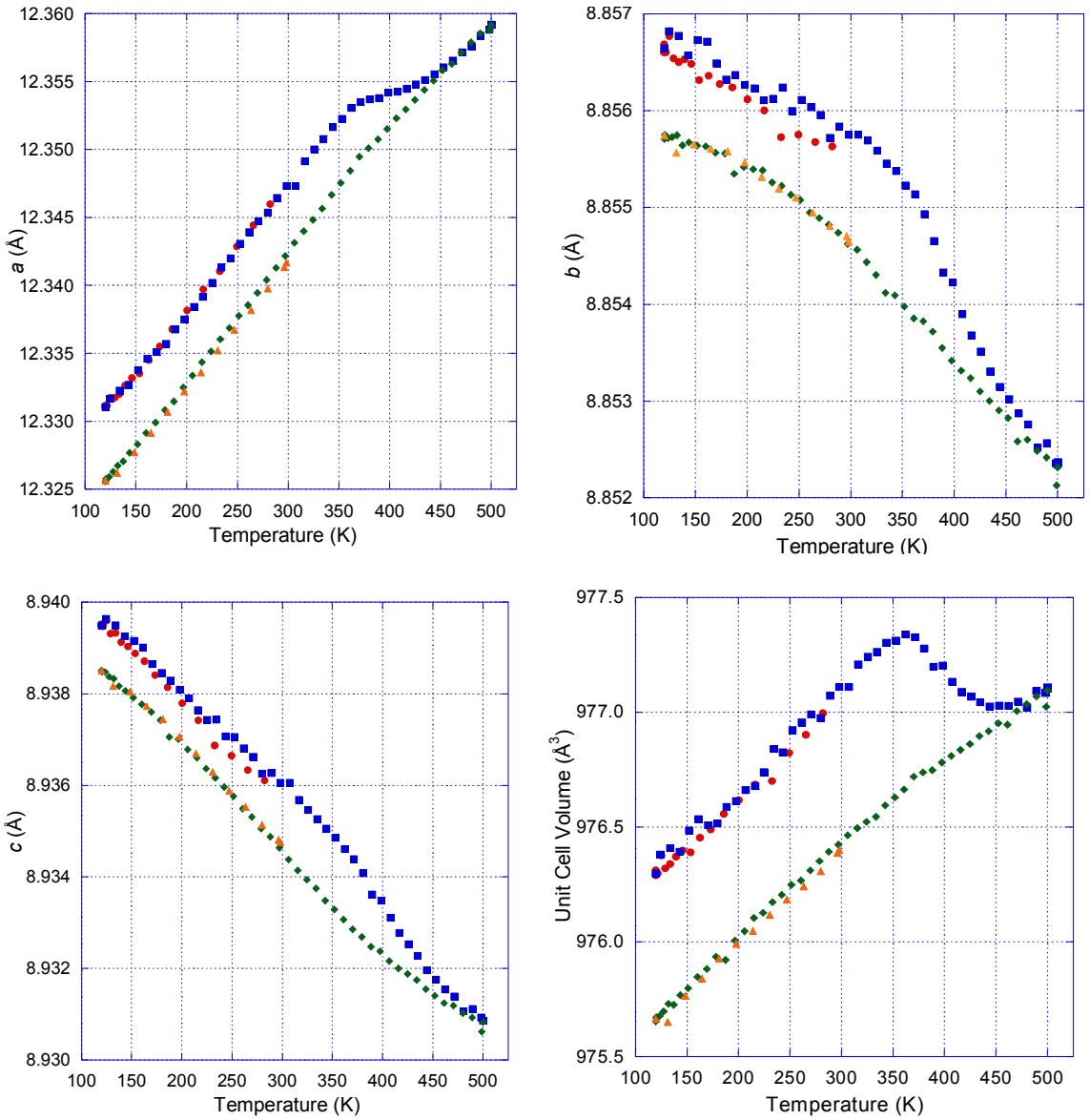

Figure 2.4. Graphs of lattice parameters *a* (top left), *b* (top right), *c* (bottom left) and unit cell volume (bottom right) vs. temperature for $Zr_2(PO_4)_2(SO_4)$ The sample was initially cooled at 6 K/min to 120 K (red circles), heated to 500 K at 3 K/min (blue squares), cooled again to 120 K at 3 K/min (green diamonds), and reheated to 300 K at 6 K/min (orange triangles).

Using linear fits to the unit cell volume values, and the *a* and *c* lattice constants, obtained during the second cooling of the sample from 500-120 K, α_V, α_a, and α_c were estimated to be 3.88(5)x10^{-6} K^{-1}, 7.36(5)x10^{-6} K^{-1}, and -2.41(2)x10^{-6} K^{-1} respectively. As the behavior of *b* versus T was strongly nonlinear, a quadratic fit (b = -1.2994x10^{-8} T^2 – 1.4813x10^{-6} T + 8.8562 where T is the temperature in Kelvin) was used to determine α_b. The R value for the quadratic fit was 0.99774. The coefficient of thermal expansion, α_b at room temperature was estimated to be -1.04x10^{-6} K^{-1}. As the temperature decreases from 500 K to 120 K, the coefficient of thermal expansion varies from -1.63x10^{-6} K^{-1} to -5.20x10^{-7} K^{-1} as shown in Figure 2.5.

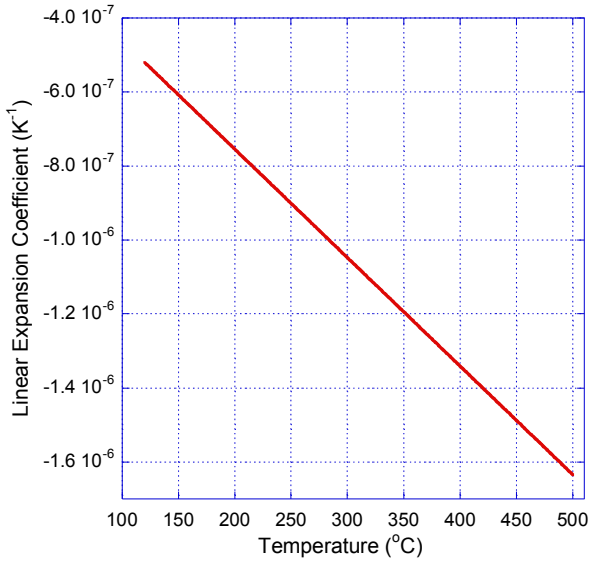

Figure 2.5. The temperature dependence of α_b. This was computed by differentiation of the quadratic that was fitted to the values of *b* determined from the diffraction data recorded as the sample was cooled from 500 to 120 K.

While, as noted earlier, the *Pbcn* structural model gave a reasonable fit to the x-ray data from the variable temperature measurements, a close examination (see Figure 2.6) of the low angle area in these x-ray diffraction data (λ = 0.61848 Å) showed the presence of peaks, [(100), (001), (010), (101), and (011)] that are not allowed for space group *Pbcn*, but are allowed for space groups *P222, P22m, P2mm,* and *Pmmm*.

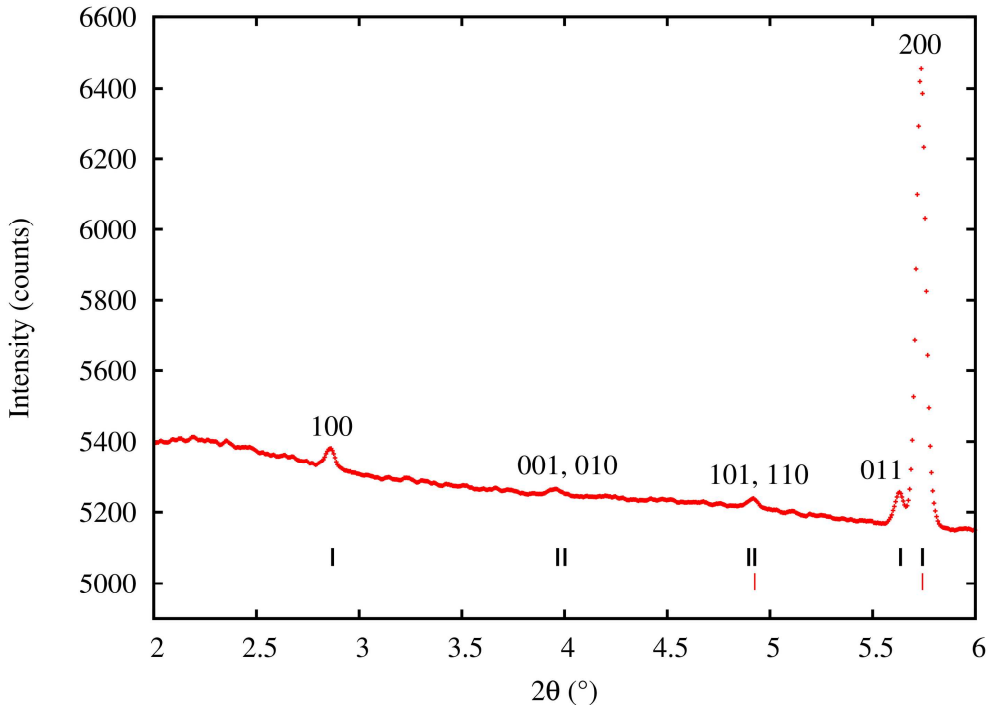

Figure 2.6. Low angle portion of a powder x-ray diffraction pattern collected at 282 K during the initial cooling of the $Zr_2(PO_4)_2(SO_4)$. Peaks expected for space group *Pbcn* are marked in red. Peaks expected for space group *P222* are marked in black.

The possibility that these extra peaks are an experimental artifact, perhaps due to λ/2 contamination or some other phenomenon seems unlikely, as the 1-BM beam line uses a Si(111) monochromator, that does reflect λ/2, and the mirror in the beam line cuts off the high energy photons from the synchrotron source. The observation of peaks that violate the systematic absence requirements of the previously reported space group throws into question the true symmetry of the material.

2.3.3 High resolution Powder X-ray Experiment

Figure 2.7 shows a Le Bail fit, using space group *Pbcn* as reported by Piffard *et al*.[32] to a high resolution powder x-ray diffraction pattern. The red tick marks in the figure indicate the locations of reflections that should be seen for this space group. The general fit quality is good, providing assurance that the material is orthorhombic, and not of lower metric symmetry. However, from 2-5º 2θ it is seen that there are four distinct peaks in the x-ray data collection pattern, but, only three of them are expected for the space group *Pbcn* (Figure 2.8). The peak at 3.28º 2θ corresponds to the (110) reflection, while the peaks at 3.83 and 4.22º 2θ correspond to the (200) and the (111) reflections respectively. While noise is very prevalent in this area, another peak in the diffraction data is noticed at 3.76º 2θ that is not expected for space group *Pbcn* (Figure 2.8).

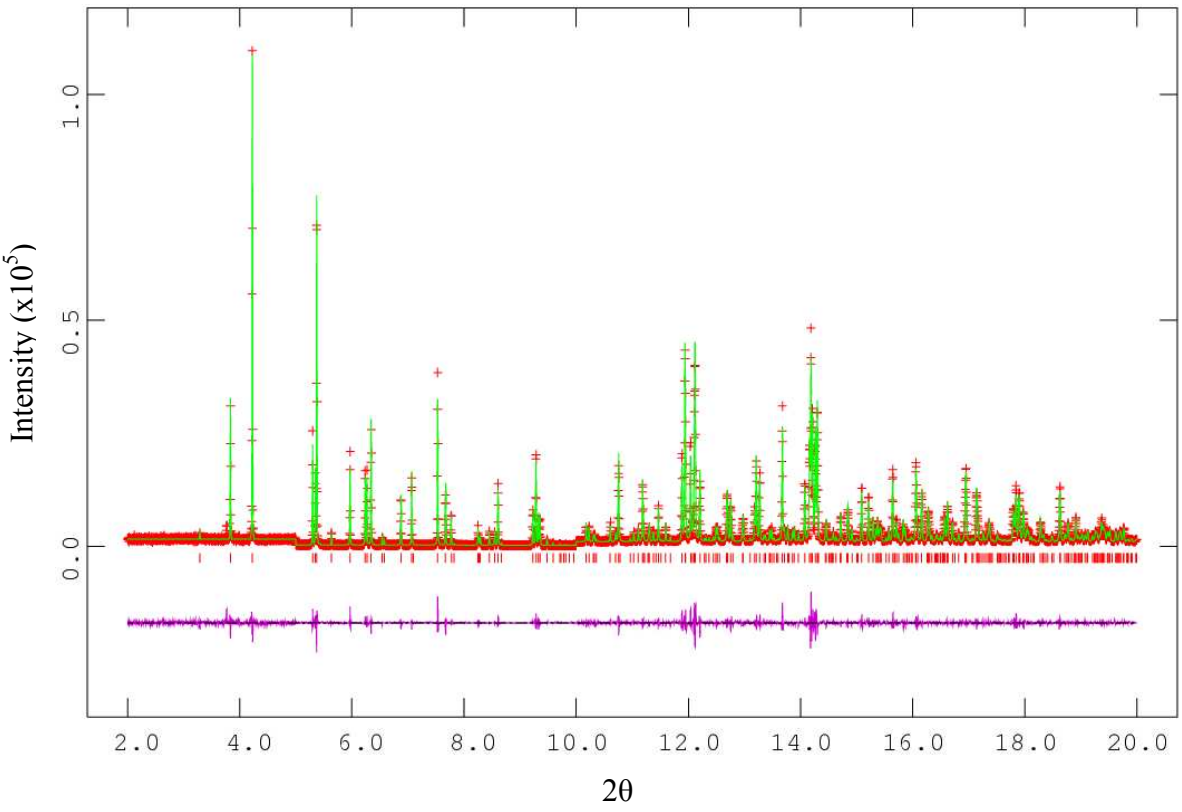

Figure 2.7. High resolution x-ray diffraction data for $Zr_2(PO_4)_2(SO_4)$ taken at $\lambda = 0.413166$ Å (in red), compared to a Le Bail fit in space group *Pbcn* (green). The difference curve is shown in purple. From 2 – 5º 2θ the intensity is multiplied by a factor of 5. From 5 – 10º 2θ the intensity is at normal scale, and from 10 – 20º 2θ the intensity is scaled by a factor of 5.

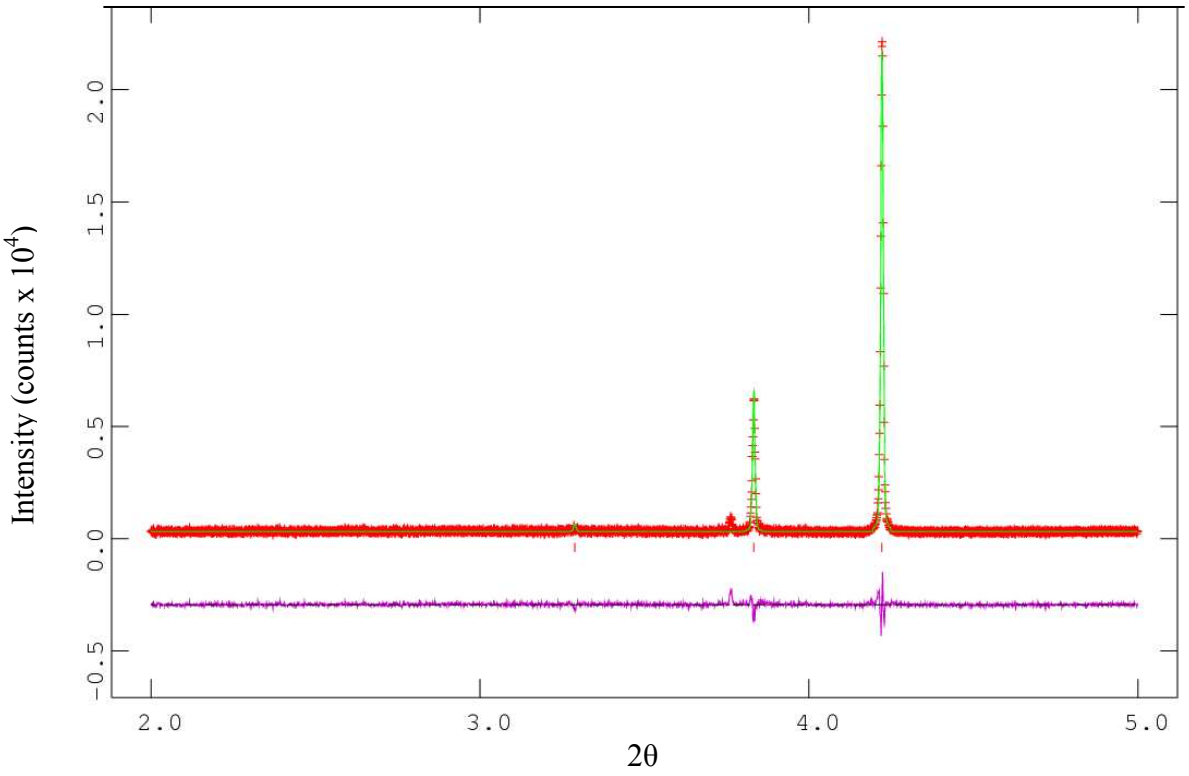

Figure 2.8. High resolution x-ray diffraction pattern (red) of $Zr_2(PO_4)_2(SO_4)$ with Le Bail fit (green) in space group *Pbcn* from 2 – 5º 2θ. The difference curve is shown below in purple. Red tick marks indicate where reflections should be for space group *Pbcn*.

2.3.4 Crystal Density Measurements

Crystal density measurements were performed, in triplicate, on $Zr_2(PO_4)_2(SO_4)$ using the flotation method. The obtained densities were 3.079g/cm^3, 3.157g/cm^3, and 3.133g/cm^3. Based on the reported *Pbcn* crystal structure, the density for $Zr_2(PO_4)_2(SO_4)$ was expected to be 3.168g/cm^3.[32]

2.3.5 Single Crystal X-ray Diffraction Measurement

Single crystal x-ray diffraction measurements were taken on a very small crystal at ChemMatCARS, Sector 15, Center for the Advanced Photon Sources, Argonne National

Lab. The data were indexed in space group *Pbna* with a unit cell of a = 8.8847(5) Å, b = 8.9595(5) Å, c = 12.3583(8) Å as indicated in Table 2.1. The atomic coordinates resulting from a complete structure refinement are given in Table 2.2. Table 2.3 shows that the calculated Zr-O bond lengths range from 2.036(8) Å to 2.086(7) Å, while P-O distances range from 1.495(8) to 1.503(7) Å, and S-O distances are 1.497(8) to 1.502(8) Å. The refinement is of low quality, as indicated by the high R factors. The merging R factor suggests that the data set itself was of low quality.

Table 2.1. Summary of the single crystal structure refinement for $Zr_2(PO_4)_2(SO_4)$.

Empirical formula	Zr2 P2 S O12
Formula weight	468.44
Temperature	95(2) K
Wavelength	0.41328 Å
Crystal system, space group	Orthorhombic, Pbna
Unit cell dimensions	a = 8.8847(5) Å alpha = 90.0073(17) deg.
	b = 8.9595(5) Å beta = 90.0285(17) deg.
	c = 12.3583(8) Å gamma = 90.0169(19) deg.
Volume	983.75(10) A^3
Z, Calculated density	4, 3.163 Mg/m^3
Absorption coefficient	7.253 mm^{-1}
F(000)	888
Theta range for data collection	1.64 to 22.14 deg.
Limiting indices	-14<=h<=12, -14<=k<=12, -22<=l<=22
Reflections collected / unique	69530 / 2677 [R(int) = 0.1173]
Completeness to theta = 22.14	85.7 %
Refinement method	Full-matrix least-squares on F^2
Data / restraints / parameters	2677 / 0 / 78
Goodness-of-fit on F^2	1.551
Final R indices [I>2σ(I)]	R_1 = 0.1467, wR_2 = 0.2253
R indices (all data)	R_1 = 0.1719, wR_2 = 0.2311
Largest diff. peak and hole	1.954 and -4.046 e.$Å^{-3}$

Table 2.2. Atomic coordinates and equivalent isotropic displacement parameters for $Zr_2(PO_4)_2(SO_4)$. U(eq) is defined as one third of the trace of the orthogonalized Uij tensor.

	x	y	z	U(eq)($Å^2$)
Zr(1)	0.7507(1)	0.0361(1)	0.3828(1)	0.008(1)
P(1)	0.3934(3)	-0.1117(3)	0.3541(2)	0.003(1)
S(1)	0.0344(3)	0.2500	0.5000	0.004(1)
O(1)	0.5614(9)	-0.0913(10)	0.3521(8)	0.017(2)
O(2)	0.9380(9)	0.1664(11)	0.4207(7)	0.018(2)
O(3)	0.8677(11)	-0.1434(10)	0.4388(8)	0.022(2)
O(4)	0.6437(9)	0.2293(8)	0.3286(6)	0.010(1)
O(5)	0.8263(10)	-0.0091(9)	0.2288(6)	0.013(2)
O(6)	0.6658(10)	0.0723(9)	0.5360(6)	0.013(1)

Table 2.3. Bond lengths [Å] and angles [deg] for $Zr_2(PO_4)_2(SO_4)$ derived from the single crystal x-ray structure refinement.

Zr(1)-O(3)	2.036(8)	O(3)-Zr(1)-O(5)	89.6(4)
Zr(1)-O(5)	2.059(8)	O(3)-Zr(1)-O(1)	92.4(4)
Zr(1)-O(1)	2.068(8)	O(5)-Zr(1)-O(1)	89.3(4)
Zr(1)-O(6)	2.065(8)	O(3)-Zr(1)-O(6)	89.9(4)
Zr(1)-O(4)	2.086(7)	O(5)-Zr(1)-O(6)	176.8(3)
Zr(1)-O(2)	2.085(8)	O(1)-Zr(1)-O(6)	87.5(3)
P(1)-O(4)#1	1.495(7)	O(3)-Zr(1)-O(4)	176.0(4)
P(1)-O(6)#2	1.499(8)	O(5)-Zr(1)-O(4)	90.9(3)
P(1)-O(5)#3	1.500(8)	O(1)-Zr(1)-O(4)	91.6(3)
P(1)-O(1)	1.503(9)	O(6)-Zr(1)-O(4)	89.8(3)
S(1)-O(3)#4	1.497(8)	O(3)-Zr(1)-O(2)	87.6(4)
S(1)-O(3)#5	1.497(8)	O(5)-Zr(1)-O(2)	93.3(3)
S(1)-O(2)	1.501(8)	O(1)-Zr(1)-O(2)	177.4(4)
S(1)-O(2)#6	1.502(8)	O(6)-Zr(1)-O(2)	89.9(3)
O(3)-S(1)#4	1.497(8)	O(4)-Zr(1)-O(2)	88.3(3)
O(4)-P(1)#7	1.495(7)	O(4)#1-P(1)-O(6)#2	109.7(4)
O(5)-P(1)#8	1.500(8)	O(4)#1-P(1)-O(5)#3	110.7(5)
O(6)-P(1)#2	1.499(8)	O(6)#2-P(1)-O(5)#3	109.5(5)
		O(4)#1-P(1)-O(1)	109.4(5)
		O(6)#2-P(1)-O(1)	109.6(5)
		O(5)#3-P(1)-O(1)	108.0(5)
		O(3)#4-S(1)-O(3)#5	108.9(9)
		O(3)#4-S(1)-O(2)	110.0(5)
		O(3)#5-S(1)-O(2)	108.7(5)
		O(3)#4-S(1)-O(2)#6	108.7(5)
		O(3)#5-S(1)-O(2)#6	110.1(5)
		O(2)-S(1)-O(2)#6	110.5(7)
		P(1)-O(1)-Zr(1)	150.6(6)
		S(1)-O(2)-Zr(1)	151.7(6)
		S(1)#4-O(3)-Zr(1)	166.5(6)
		P(1)#7-O(4)-Zr(1)	145.5(5)
		P(1)#8-O(5)-Zr(1)	151.8(5)
		P(1)#2-O(6)-Zr(1)	175.4(5)

2.4 Discussion

2.4.1 Difficulties in Sample Preparation

In the preparation of $Zr_2(PO_4)_2(SO_4)$, a white gel forms as soon as the phosphoric acid is added to the $ZrO(NO_3)\cdot 6\ H_2O$ and HNO_3 solution. If this wet gel is heated with sulfuric acid for the given time frame presented in section 2.2.1, no product is

recoverable. However, if the gel is dried to the cake-like material, it reacts with sulfuric acid to give the desired product. The solubility of the gel in sulfuric acid is between 0.2-0.3 g/12 mL of concentrated H_2SO_4. High quality single crystals of $Zr_2(PO_4)_2(SO_4)$ could not be grown. The largest crystals we have been able to generate were ~50 x 50 x 15 μm. Their small size prohibited the use of a home laboratory based single crystal diffractometer and led to our synchrotron study. The growth of larger crystals is limited by nucleation within the sulfuric acid. It has been noted that if the dried gel is ground to a finer powder larger crystals of the final product are able to be generated. Using traditional recrystalization methods is difficult for this material due to the high boiling point of sulfuric acid. If we can find a way to recrystallize this material out of the sulfuric acid we should be able to generate larger crystals to get better quality data sets out of the material.

2.4.2 Laboratory X-ray Diffraction

The powder diffraction patterns of $Zr_2(PO_4)_2(SO_4)$ collected on our home laboratory instrument were in generally good agreement with the pattern reported in the ICDD database. However, our experimental diffraction patterns display a very noticeable shoulder, at 14.02º 2θ, that is unaccounted for by the database pattern. This lead us to believe, initially, that the peak was due to an impurity. However, after appearing in the powder diffraction patterns of each batch synthesized, we believe that this peak is real and may be an important aspect to the further characterization of this material. This shoulder can be accounted for when a lower symmetry space group is assumed (see Figure 2.9).

.

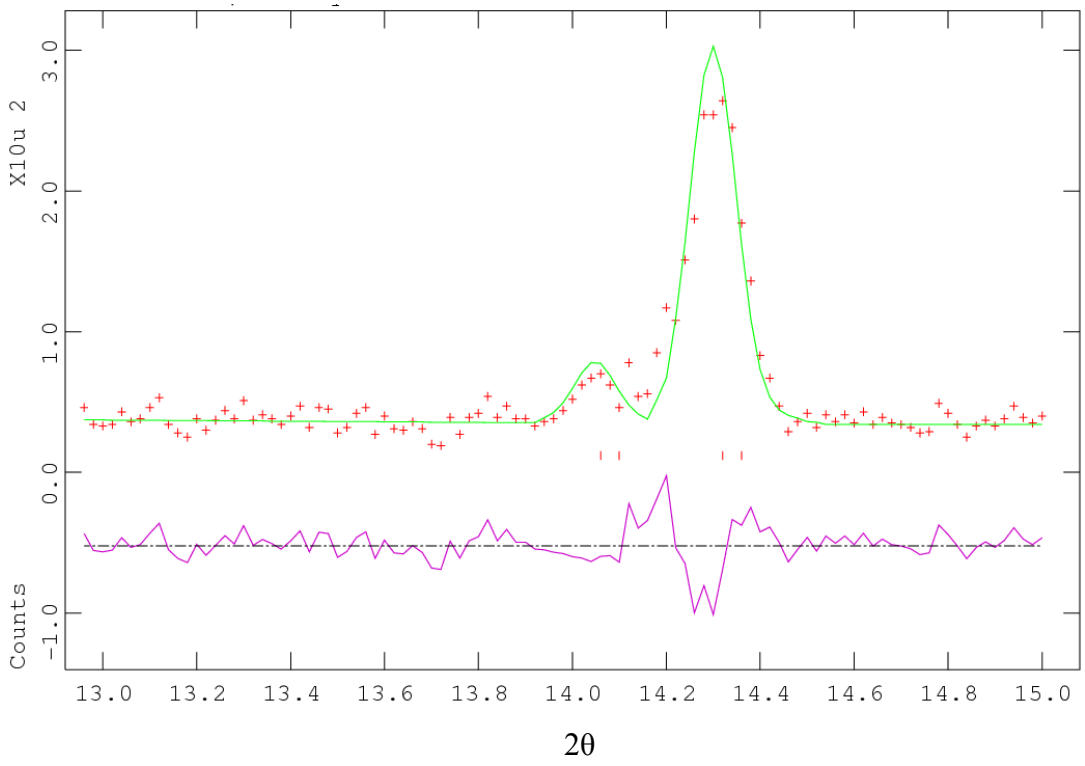

Figure 2.9. Low angle portion of x-ray data collected on $Zr_2(PO_4)_2(SO_4)$ in laboratory (red), compared to a Le Bail fit in *P222* (green). The difference curve can be seen in purple.

2.4.3 TGA Measurements

TGA measurements of $Zr_2(PO_4)_2(SO_4)$ reveal that the initial sample has three distinct weight losses from the starting material. The first weight loss of the sample occurs between 30-100 ºC and corresponds to a 0.5% loss from the initial starting material. Due to the fact that the starting zirconium material is reacted and stored in an open atmosphere, it can only be assumed that our final product has picked up some water on the outside of the crystal framework. Under the nitrogen flow within the apparatus along with heating, absorbed water would be the first thing to come off of the system. This results in 0.13 mole of water being lost per mole of sample.

The second loss observed in the TGA of $Zr_2(PO_4)_2(SO_4)$ occurs in the range from 100-150ºC and probably corresponds to 0.30 mole of water lost per mole of sample material. This weight loss suggests that the crystal may contain some hydroxyl defects or there could be some occluded water. The weight loss could result from the expulsion of occluded water or, as the sample is heated, the hydroxyl groups combining to form water that is then lost. The related material $Zr_{18}(OH)_{46}(SO_4)_{13}\cdot 33H_2O$[52] shows a weight loss due to dehyroxylation that extends up to 550 ºC, perhaps, suggesting that dehydroxylation should occur at a higher temperature than we observe for the weight loss in $Zr_2(PO_4)_2(SO_4)$. This $Ca(H_2PO_4)_2\cdot H_2O$ which has loss of 0.3 mol H_2O on heating from 100-170 ºC and suggests that there are vacancies on the metal center.[53]

From this point, the TGA curve plateaus and remains constant until 370 ºC, where further weight loss occurs. The weight loss begins to level off at 500 ºC. X-ray diffraction patterns of the recovered material reveal that it is still largely zirconium phosphate sulfate, thus it is assumed that the core structure of the material hasn't changed and the weight loss must be associated with either the decomposition of an impurity or a relatively subtle change in the composition and structure of the main phase. The observed weight loss would be consistent with the release of 0.26 mole of SO_3 gas for every mole of sample. In this situation no oxidation or reduction occurs making SO_3 the easiest substance to be removed from our system. However, since elemental analysis hasn't been performed on this sample, we cannot say for sure that the starting material is decomposing in this fashion.

While our hypothesis that the low temperature weight loss is due to the elimination of water from the "$Zr_2(PO_4)_2(SO_4)$" sample is supported by our *in-situ* x-ray measurements

at the same temperature, we do not have x-ray data above 500 K. A future *in-situ* x-ray study in the temperature range of the ~370 ºC weight loss would definitively determine if this weight loss is due to an impurity or a change in the composition of the main phase.

2.4.4 Variable Temperature X-ray Powder Diffraction Measurements

Variable temperature x-ray powder diffraction experiments reveal that the material $Zr_2(PO_4)_2(SO_4)$ exhibits anisotropic positive thermal expansion, as seen in Figure 2.4, with a volume coefficient of thermal expansion α_V of $3.88(5)x10^{-6}$ K^{-1} over the temperature range 120-500 K, based on data collected during the second cooling at 3 K/min. However, many members of this structural family show negative thermal expansion. For example, $Sc_2(WO_4)_3$, $Sc(MoO_4)_3$, $Al_2(WO_4)_3$, $Zr_2(PO_4)_2(WO_4)$, and $Zr_2(PO_4)_2(MoO_4)$ have volume CTEs of ~ -11×10^{-6}, -5×10^{-6}, -3×10^{-6}, -6×10^{-6}, and -6×10^{-6} K^{-1}.[23] The thermal expansion of $Zr_2(PO_4)_2(SO_4)$ is greater than that of $Al_{1.6}In_{0.4}(WO_4)_3$ which has a volume CTE of 1.5×10^{-6} K^{-1} and less than $In_2(WO_4)_3$ which has a volume CTE of $\sim 10 \times 10^{-6}$ K^{-1}.[23] The anisotropy of this material, however, is similar to $Sc_2(WO_4)_3$, $Zr_2(PO_4)_2(WO_4)$, and $Zr_2(PO_4)_2(MoO_4)$ and other members of the family in that two axes contract while the third expands with an increase in temperature.[23]

Upon the first heating of the sample from 120 K to 500 K a decrease in the volume is noticed in the temperature range of 360-450 K. Over this same temperature range, a change in slope is noticed for all of the lattice parameters. While in most instances, this change in volume might be accounted for by a phase transition, upon noticing that the lattice constants are not reversible upon reheating, this is highly unlikely. After correlating this data with the TGA data, the decrease in volume is due to the removal of

water or hydroxyl groups within the sample. As the water is removed from the structure, a change in lattice constants is observed. This change is irreversible upon cooling and reheating and thus is a loss to the system. The removal of water in the system decreases the overall volume of the cell and allows other atoms within the structure to occupy the space of the leaving group. During the first heating, above 450 K, the material experiences anisotropic positive thermal expansion.

During the first cooling and heating of the sample, it was noticed that while lattice parameters *a* and *c* and the unit cell volume appear reversible, while lattice parameter *b* has significant variation. In lattice parameter *b*, there appears to be approximately a 25 K shift to make lattice constants equal. Typically this would suggest that there is an error in the thermal calibration, however, since *a*, *c*, and the unit cell volume are reversible, this is highly unlikely. Rather, due to the slight variation in the curves for *a* and *c* it could be suggested that a shift in the wavelength has occurred during the experiment which can happen with a change of current in the synchrotron.

2.4.5 Single Crystal Experiment

Data collected in the single crystal experiment reveal that lattice parameters *a*, *b*, and *c* are 8.8847(5), 8.9595(5), and 12.3583(8) Å while $\alpha = 90.0073(17)^{\circ}$, $\beta = 90.0285(17)^{\circ}$, and $\gamma = 90.0169(19)^{\circ}$. In comparison, when the axes are aligned along the same direction the lattice constants at 120 K are 8.8566(2), 8.9392(2), and 12.3310(2) for *a, b,* and *c* respectively. Comparing the ratios of *a*:*b*:*c* for the single crystal versus powder diffraction, we find the ratios of single crystal are 1:1.0084:1.3910 compared to the powder diffraction ratios of 1:1.0093:1.3923. These values are not extremely consistant

with the values obtained from the powder diffraction experiments and the crystal may not be representative of the sample as a whole. The angles α, β, and γ are close enough to 90.00 degrees that this cell can be thought of as orthorhombic. However, when examining the values for the R indices R_1 is 0.1467 and wR_2 = 0.2253 while for all data R_1 = 0.1719 and wR_2 = 0.2311. These values indicate that the fit using the *Pbna* space group is not very good. This may be due to the previously mentioned space group problem. However, this could also be due to the low statistical quality of the single crystal data set. A larger crystal would be needed to obtain a significantly higher quality single crystal data set.

Measurements of the single crystal of $Zr_2(PO_4)_2(SO_4)$ were recorded for all reflections $-14 \leq h \leq 12$, $-14 \leq k \leq 12$, and $-22 \leq l \leq 22$ in *Pbna*. After reflections where $F_o^2 \leq 3\sigma$ were removed it was noticed that the (100), (010), (001), (110), (101), and (011) reflections were absent. This is inconsistent with the powder patterns that we have collected for this sample, which have these reflections present. Overall from this measurement we can suggest that either the single crystal used in this experiment is either not a good representative of the sample as a whole, or the diffraction data in was so weak that the true space group was not apparent.

The Zr-O, P-O, and S-O bond distances estimated from our single crystal refinement are in very good agreement with those reported by Piffard *et al*.[32] The P-O distances range from 1.495(7) to 1.503(8) Å. However, when compared to the P-O distances seen for well ordered phosphates, such as, Na_3PO_4, $Ca_3(PO_4)_2$, and $FePO_4$ (1.52-1.56 Å), these bond distances seem to be short.[54-56] In addition, our S-O experimental distances were in the range of 1.497(8)-1.502(8) Å. These values are too large when compared to the S-O distances in ordered sulfates such as Na_2SO_4, $CaSO_4$, and $Fe_2(SO_4)_3$ (1.46-1.48 Å).[57-59] It

is also noted that our P-O and S-O distances are the same length within experimental error. This leads to the conclusion that both the P and S sites within the crystal structure are interchangeable and there is no set order for these atoms within the unit cell. Disorder amongst phosphate and sulfate groups has previously been reported for $SrAl_3(PO_4)(SO_4)(OH)_6$, $CaAl_3(PO_4)(SO_4)(OH)_6$, and $Pb_4(PO_4)_2(SO_4)$.[33, 34, 36]

2.4.6 Crystal Density Measurements

The crystal density measurements for the $Zr_2(PO_4)_2(SO_4)$ sample average out to be a value of 3.123 g/cm^3. This is slightly lower than that reported in the literature 3.168 g/cm^3,[32] and calculated from our single crystal (3.163 g/cm^3) assuming that the sample is defect free. The observation that the experimental density is low compared to that expected for a perfect crystal is not consistent with the presence of occluded water in the structure as this would give a higher density. The decrease in density can be explained if there are vacancies in the crystal structure to allow for the incorporation of hydroxyl defects within the framework. Two possible stoichiometries that could accommodate the loss of 0.3 molof water on heating are $Zr_{1.85}(OH)_{0.6}P_2SO_{11.4}$ and $Zr_2(OH)_{0.6}P_2S_{0.9}O_{11.4}$. They have calculated densities of 3.077 and 3.145 g/cm^3 respectively. The former proposal seems inconsistent with our measured density, but the latter is in reasonable agreement with the measurements.

2.4.7 High Resolution X-ray Powder Diffraction Measurements

Examination of the high resolution x-ray powder diffraction pattern reveals that while the space group of the material is still unable to be obtained, we have been able to

determine that the overall metric symmetry of the framework cannot be any lower than orthorhombic. While we are able to get a good Le Bail fit of the data in space group *Pbcn*, the resolution of the peaks is so good that the (011) reflection in the diffraction pattern is clearly missed by the model. The signal to noise ratio at low angle is not large enough to allow the (100), (010), (001), (101), and (110) reflections to be visible making it difficult to tell what space group this material belongs in. We suggest that since these reflections are visible in the *in-situ* experiment and unaccounted for in the high resolution that $Zr_2(PO_4)_2(SO_4)$ could actually crystallize in space groups *Pmmm*, *P2mm*, *P22m*, or *P222* since these provide for no systematic absences in an orthorhombic crystal.

2.5 Conclusions

In $Zr_2(PO_4)_2(SO_4)$, we have learned that the material exhibits an overall anisotropic positive thermal expansion, with two of the three unit cell axes exhibiting NTE. Thermal expansion of this material is practically linear over the temperature range 120-500 K except from 360-450 K where the material loses water from the crystal framework. This is further confirmed through TGA measurements where a weight loss is observed in the same temperature range. Additional weight losses and crystal density measurements suggest that there are a few vacancies within the structure and hydroxyl groups are added for charge balance.

More importantly, we have concluded that $Zr_2(PO_4)_2(SO_4)$ has been characterized in the wrong space group due to the presence of several reflections at low angle that aren't as visible using a normal copper x-ray tube. Synchrotron radiation also has let us

determine that the metric symmetry of the system is orthorhombic. We have predicted that this material actually crystallizes in a lower symmetry orthorhombic space group such as *P222*, *P22m*, *P2mm*, or *Pmmm*.

2.6 References

1. Evans, J. S. O.; Mary, T. A.; Vogt, T.; Subramanian, M. A.; Sleight, A. W., Negative Thermal Expansion in ZrW_2O_8 and HfW_2O_8. *Chem. Mater.* **1996,** 8, 2809-2823.

2. Sleight, A. W., Compounds that Contract on Heating. *Inorg. Chem.* **1998,** 37, 2854-2860.

3. Mittal, R.; Chaplot, S. L.; Schobes, H.; Kolesnikov, A. I.; Loong, C.-K.; Lind, C.; Wilkinson, A. P., Negative thermal expansion in cubic $ZrMo_2O_8$: Inelastic neutron scattering and lattice dynamical studies. *Phys. Rev. B* **2004,** 70, 214303.

4. Xing, Q. F.; Xing, X. R.; Yu, R. B.; Du, L.; Meng, J.; Luo, J.; Wang, D.; Liu, G. R., Single crystal growth of ZrW_2O_8 by hydrothermal route. *J. Cryst. Growth* **2005,** 283, 208-214.

5. White, K. M.; Lee, P. L.; Chupas, P. J.; Chapman, K. W.; Payzant, E. A.; Jupe, A. C.; Bassett, W. A.; Zha, C. S.; Wilkinson, A. P., Synthesis, Symmetry, and Physical Properties of Cerium Pyrophosphate. *Chem. Mater.* **2008,** 20, 3728-3734.

6. Varga, T.; Wilkinson, A. P.; Haluska, M.; Payzant, E. A., Preparation and thermal expansion of $(M^{III}_{0.5}M'^{V}_{0.5})P_2O_7$ with the ZrP_2O_7 structure. *J. Solid State Chem.* **2005,** 178, 3541-3546.

7. Xiao, X. L.; Cheng, Y. Z.; Peng, J.; Wu, M. M.; Chen, D. F.; Hu, Z. B.; Kiyanagi, R.; Fieramosca, J. S.; Short, S.; Jorgensen, J., Thermal expansion properties of $A_2(MO_4)_3$ (A = Ho and Tm; M = W and Mo). *Solid State Sciences* **2008,** 10, 321-325.

8. Evans, J. S. O.; Mary, T. A.; Sleight, A. W., Structure of $Zr_2(WO_4)(PO_4)_2$ from Powder X-ray Data: Cation Ordering with No Superstructure. *J. Solid State Chem.* **1995,** 120, 101-104.

9. Mary, T. A.; Evans, J. S. O.; Vogt, T.; Sleight, A. W., Negative Thermal Expansion from 0.3 to 1050 Kelvin in ZrW_2O_8. *Science* **1996,** 272, 90-92.

10. Evans, J. S. O.; Mary, T. A.; Sleight, A. W., Negative thermal expansion materials. *Physcia B* **1998,** 241-243, 311-316.

11. Lind, C.; Wilkinson, A. P.; Hu, Z.; Short, S.; Jorgensen, J. D., Synthesis and Properties of the Negative Thermal Expansion Material Cubic Zirconium Molybdate. *Chem. Mater.***1998,** 10, 2335-2337.

12. Lind, C.; Wilkinson, A. P.; Rawn, C. J.; Payzant, E. A., Preparation of the negative thermal expansion material cubic $ZrMo_2O_8$. *J. Mater. Chem.* **2001,** 11, 3354-3359.

13. Yamamura, Y.; Nakajima, N.; Tsuji, T., Calorimetric and x-ray diffraction stduies of α-to-β structural phase transitions in HfW_2O_8 and ZrW_2O_8. *Phys. Rev. B* **2001,** 64, 184109.

14. Yamamura, Y.; Nakajima, N.; Tsuji, T.; Iwasa, Y.; Saito, K.; Sorai, M., Heat capacity and Gruneisen functions of negative thermal expansion compound HfW_2O_8. *Solid State Commun.* **2002,** 121, 213-217.

15. Kennedy, C. A.; White, M. A.; Wilkinson, A. P.; Varga, T., Low thermal conductivity of the negative thermal expansion material, $HfMo_2O_8$. *Appl. Phys. Lett.* **2007,** 90, 151906-3.

16. Sleight, A. W., Isotropic Negative Thermal Expansion. *Annual Review of Materials Science* **1998,** 28, 29-43.

17. Evans, J. S. O.; Mary, T. A.; Sleight, A. W., Negative Thermal Expansion in $Sc_2(WO_4)_3$. *J. Solid State Chem.* **1998,** 137, 148-160.

18. Mary, T. A.; Sleight, A. W., Bulk thermal expansion for tungstate and molybdates of the type $A_2M_3O_{12}$. *J. Mater. Res.* **1999,** 14, 912-915.

19. Forster, P. M.; Sleight, A. W., Negative thermal expansion in $Y_2W_3O_{12}$. *Int. J. Inorg. Mater.* **1999,** 1, 123-127.

20. Evans, J. S. O.; Jorgensen, J. D.; Short, S.; David, W. I. F.; Ibberson, R. M.; Sleight, A. W., Thermal expansion in the orthorhombic γ-phase of ZrW_2O_8. *Phys. Rev. B* **1999,** 60, 14643-14648.

21. Varga, T.; Wilkinson, A. P.; Lind, C.; Bassett, W. A.; Zha, C.-S., High pressure synchrotron x-ray powder diffraction study of $Sc_2Mo_3O_{12}$ and $Al_2W_3O_{12}$ *J. Phys.: Condens. Matter* **2005,** 17, 4271-4283.

22. Varga, T.; Wilkinson, A. P.; Jorgensen, J. D.; Short, S., Neutron powder diffraction study of the orthorhombic to monoclinic transition in $Sc_2W_3O_{12}$ on compression. *Solid State Sciences* **2006,** 8, 289-295.

23. Evans, J. S. O.; Mary, T. A.; Sleight, A. W., Negative Thermal Expansion in a Large Molybdate and Tungstate Family. *J. Solid State Chem.* **1997,** 133, 580-583.

24. Evans, J. S. O.; Mary, T. A., Structural Phase Transitions and negative thermal expansion in $Sc_2(MoO_4)_3$. *Int. J. Inorg. Mater.* **2000,** 2, 143-151.

25. Cetinkol, M.; Wilkinson, A. P.; Lee, P. L., Structural changes accompanying negative thermal expansion in $Zr_2(MoO_4)(PO_4)_2$. *J. Solid State Chem.* **submitted for publication**.

26. Cetinkol, M.; Wilkinson, A. P., Pressure Dependence of Negative Thermal Expansion in $Zr_2(WO_4)(PO_4)_2$. *Solid State Commun.* **2009,** 149, 421-424.

27. Korthuis, V.; Khosrovani, N.; Sleight, A. W.; Roberts, N.; Dupree, R.; Warren, W. W., Negative Thermal Expansion and Phase Transitions in the $ZrV_{2-x}P_xO_7$ Series. *Chem. Mater.* **1995,** 7, 412-417.

28. Losilla, E. R.; Cabeza, A.; Bruque, S.; Aranda, M. A. G.; Sanz, J.; Iglesias, J. E.; Alonso, J. A., Syntheses, Structures, and Thermal Expansion of Germanium Pyrophosphates. *J. Solid State Chem.* **2001,** 156, 213-219.

29. Cabeza, A.; Aranda, M. A. G.; Cantero, F. M.; Lozano, D.; Martinez-Lara, M.; Bruque, S., Synthesis, Structure, and Characterization of Uranium(IV) Phenyl Phosphonate, $U(O_3PC_6H_5)_2$, and Uranium(IV) Pyro Phosphate, UP_2O_7. *J. Solid State Chem.* **1996,** 12, 181-189.

30. Ota, T.; Yamai, I., Thermal expansion of ZrP_2O_7 and related solid solutions. *J. Mater. Sci.* **1987,** 22, 3762-3764.

31. Suzuki, T.; Omote, A., Negative Thermal Expansion in $(HfMg)(WO_4)_3$. *J. Am. Ceram. Soc.* **2004,** 87, 1365-1367.

32. Piffard, Y.; Verbaere, A.; Kinoshita, M., Beta-$Zr_2(PO_4)_2SO_4$ - A Zirconium Phosphato-Sulfate With a $Sc_2(WO_4)_3$ Structure - A Comparison Between Garnet, NASICON, and $Sc_2(WO_4)_3$. *J. Solid State Chem.* **1987,** 71, 121-130.

33. Pabst, A., SOME COMPUTATIONS ON SVANBERGITE, WOOD-HOUSEITE AND ALUNITE. *Am. Mineral.* **1947,** 32, 16-30.

34. Kato, T. M., Y., The Crystal Structure of Jarosite and Svanbergite. *Mineralogical Journal* **1977,** 8, 419-430.

35. Giuseppetti, G.; Tadini, C., Corkite, $PbFe_3(SO_4)(PO_4)(OH)_6$, its Crystal-Structure and Ordered Arrangement of the Tetrahedral Cations. *Neues Jahrbuch Fur Mineralogie-Monatshefte* **1987**, 2, 71-81.

36. Barbier, J., Refinement of the Eulytite-Type $Pb_4(PO_4)_2SO_4$ Structure. *Euro. J. Solid State Inorg. Chem.* **1994,** 31, 163-171.

37. Elliott, P.; Brugger, J.; Pring, A.; Cole, M. L.; Willis, A. C.; Kolitsch, U., Birchite, a new mineral from Broken Hill, New South Wales, Australia: Description and structure refinement. *Am. Mineral.* **2008,** 93, 910-917.

38. Fanfani, L.; Zanazzi, P. F., Structural Similarities of Some Secondary Lead Minerals. *Mineralogical Magazine and Journal of the Mineralogical Society* **1967,** 36, 522-&.

39. Durif, A., Sur Quelques Composes Isomorphes De Leulytine. *Comptes Rendus Hebdomadaires Des Seances De L Academie Des Sciences* **1957,** 244, 2815-2817.

40. Stumper, R.; Mettelock, P., *Chimie Physique - Cinetique de la Dissociation Thermique du Sulfo-Phosphate Bizirconique. *Comptes Rendus Hebdomadaires Des Seances De L Academie Des Sciences* **1947,** 224, 654-655.

41. Alamo, J.; Roy, R., Zirconium phospho-sulfates with $NaZr_2(PO_4)_3$-type structure. *J. Solid State Chem.***1984,** 51, 270-273.

42. Hong, H. Y.-P., Crystal Structures and Crystal Chemistry in the System $Na_{1+x}Zr_2Si_xP_{3-x}O_{12}$. *Mater. Res.Bull.* **1976,** 11, 173-182.

43. Blasse, G.; Piffard, Y.; Struye, L., The luminescence of [beta]-$Zr_2(PO_4)_2SO_4$ in comparison to that of isomorphous $Sc_2(WO_4)_3$. *Chem. Phys. Lett.* **1988,** 147, 514-516.

44. Hammersley, A. P.; Svensson, S. O.; Hanfland, M.; Fitch, A. N.; Hausermann, D., Two-dimensional detector software: From real detector to idealised image or two-theta scan. *High Pressure Research* **1996,** 14, 235-248.

45. Larson, A. C.; Von Dreele, R. B., *GSAS - General Structure Analysis System*. Report LA-UR-86-748: Los Alamos Laboratory, 1987.

46. Toby, B. H., EXPGUI, a graphical user interface for GSAS. *J. Appl. Crystallogr.* **2001,** 34, 210-213.

47. Sheldrick, G. M., *Program for the Solution of Crystal Structures*. University of Gottingen: Germany, 1986.

48. Sheldrick, G. M., *Program for Crystal Structure Determination*. Univ. of Gottingen: Germany, 1993.

49. Stout, G. H., *X-ray structure determination : a practical guide*. 2nd ed. ed.; Wiley: New York :, 1989.

50. Zamvil, S.; Pludow, R.; Fucaloro, A. F., Simple Method For Measuring Crystal Densities. *J. Appl. Crystallogr.* **1978,** 11, 163-163.

51. Lee, P. L.; Shu, D.; Ramanathan, M.; Preissner, C.; Wang, J.; Beno, M. A.; Von Dreele, R. B.; Ribaud, L.; Kurtz, C.; Antao, S. M.; Jiao, X.; Toby, B. H., A twelve-analyzer detector system for high-resolution powder diffraction. *J. Synchrotron Rad.* **2008,** 15, 427-432.

52. Ahmed, M. A. K.; Fjellvag, H.; Kjekshus, A., Synthesis and characterization of zirconium and hafnium sulfates, hydroxide sulfates and oxide sulfates. *Acta Chem. Scand.* **1999,** 53, 24-33.

53. Boonchom, B., Parallelogram-like microparticles of calcium dihydrogen phosphate monohydrate ($Ca(H_2PO_4)_2 \cdot H_2O$) obtained by a rapid precipitation route in aqueous and acetone media. *J. Alloys Compd.* **2009,** 482, 199-202.

54. Belik, A. A.; Bykov, A. B.; Verin, I. A.; Golubev, A. M.; Ivanov-Shitz, A. K.; Nistyuk, A. V., Structure and electric conductivity of Na_3PO_4 single crystals. *Crystallography Reports* **2000,** 45, 902-906.

55. Mathew, M.; Schroeder, L. W.; Dickens, B.; Brown, W. E., Crystal-Structure of Alpha-$Ca_3(PO_4)_2$. *Acta Crystallogr., Sect. B* **1977,** 33, 1325-1333.

56. Kostiner, E.; Rea, J. R., CRYSTAL-STRUCTURE OF FERROUS PHOSPHATE FE3(PO4)2. *Inorg. Chem.* **1974,** 13, 2876-2880.

57. Rasmussen, S. E.; Jorgensen, J. E.; Lundtoft, B., Structures and phase transitions of Na2SO4. *J. Appl. Crystallogr.* **1996,** 29, 42-47.

58. Bezou, C.; Nonat, A.; Mutin, J. C.; Christensen, A. N.; Lehmann, M. S., Investigation of the Crystal-Structure of Gamma-$CaSO_4$, $CaSO_4 \cdot 0.5\ H_2O$, and $CaSO_4 \cdot 0.6\ H_2O$ by Powder Diffraction Methods. *J. Solid State Chem.* **1995,** 117, 165-176.

59. Christidis, P. C.; Rentzeperis, P. J.; Kirfel, A.; Will, G., X-ray Determination of the Electron-Density Distribution in Monoclinic $Fe_2(SO_4)_3$. *Z. Kristallogr.* **1983,** 164, 219-236.

Supplimentary Materials

Table S.1. Table of lattice constants and standard deviations for the material $Zr_2(PO_4)_2(SO_4)$ calculated from Rietveld refinement of the *in-situ* X-ray data. Temperatures were recorded from the average of the temperature when the shutter opened and when the shutter closed.

Temperature K	*a*	σ *a*	*b*	σ *b*	*c*	σ *c*	V	σ V
282.32	12.3460	0.0002	8.8556	0.0002	8.9361	0.0002	976.99	0.02
265.79	12.3444	0.0002	8.8557	0.0002	8.9363	0.0002	976.90	0.02
249.35	12.3429	0.0002	8.8557	0.0002	8.9366	0.0002	976.82	0.02
232.95	12.3410	0.0002	8.8557	0.0002	8.9369	0.0002	976.70	0.02
216.55	12.3397	0.0002	8.8560	0.0002	8.9374	0.0002	976.68	0.02
200.46	12.3382	0.0002	8.8561	0.0002	8.9378	0.0002	976.62	0.02
185.91	12.3368	0.0002	8.8562	0.0002	8.9381	0.0002	976.56	0.02
173.52	12.3355	0.0002	8.8563	0.0002	8.9384	0.0002	976.49	0.02
162.90	12.3345	0.0002	8.8564	0.0002	8.9387	0.0002	976.45	0.02
153.79	12.3335	0.0002	8.8563	0.0002	8.9389	0.0002	976.39	0.03
146.18	12.3332	0.0002	8.8565	0.0002	8.9390	0.0002	976.40	0.02
139.62	12.3326	0.0002	8.8565	0.0002	8.9391	0.0002	976.37	0.02
133.97	12.3320	0.0002	8.8565	0.0002	8.9393	0.0002	976.34	0.03
129.12	12.3317	0.0002	8.8565	0.0002	8.9393	0.0002	976.32	0.02
125.07	12.3317	0.0002	8.8568	0.0002	8.9396	0.0002	976.38	0.02
121.68	12.3312	0.0002	8.8566	0.0002	8.9395	0.0002	976.30	0.02
119.71	12.3310	0.0002	8.8566	0.0002	8.9395	0.0002	976.29	0.02
119.97	12.3311	0.0002	8.8566	0.0002	8.9395	0.0002	976.30	0.02
120.00	12.3311	0.0002	8.8567	0.0002	8.9395	0.0002	976.31	0.02
120.00	12.3311	0.0002	8.8566	0.0002	8.9395	0.0002	976.30	0.02
124.50	12.3316	0.0002	8.8568	0.0002	8.9396	0.0002	976.38	0.02
133.82	12.3323	0.0002	8.8568	0.0002	8.9395	0.0002	976.41	0.02
143.01	12.3327	0.0002	8.8566	0.0002	8.9393	0.0002	976.39	0.02
152.14	12.3338	0.0002	8.8567	0.0002	8.9392	0.0002	976.48	0.02
161.32	12.3346	0.0002	8.8567	0.0002	8.9390	0.0002	976.53	0.02
170.43	12.3351	0.0002	8.8565	0.0002	8.9386	0.0002	976.51	0.02
179.60	12.3357	0.0002	8.8563	0.0002	8.9385	0.0002	976.52	0.02
188.74	12.3368	0.0002	8.8564	0.0002	8.9383	0.0002	976.59	0.02
197.88	12.3375	0.0002	8.8563	0.0002	8.9381	0.0002	976.61	0.02
206.99	12.3384	0.0002	8.8562	0.0002	8.9379	0.0002	976.66	0.02
216.07	12.3392	0.0002	8.8561	0.0002	8.9376	0.0002	976.68	0.02
225.10	12.3402	0.0002	8.8561	0.0002	8.9374	0.0002	976.74	0.02
234.27	12.3413	0.0002	8.8562	0.0002	8.9374	0.0002	976.84	0.02
243.38	12.3420	0.0002	8.8560	0.0002	8.9371	0.0002	976.83	0.02
252.55	12.3431	0.0002	8.8561	0.0002	8.9371	0.0002	976.92	0.02
261.66	12.3439	0.0002	8.8560	0.0002	8.9368	0.0002	976.96	0.02
270.76	12.3447	0.0002	8.8560	0.0002	8.9366	0.0002	976.99	0.02
279.87	12.3454	0.0002	8.8557	0.0002	8.9363	0.0002	976.97	0.02
289.07	12.3464	0.0002	8.8558	0.0002	8.9363	0.0002	977.07	0.02
298.14	12.3473	0.0002	8.8558	0.0002	8.9361	0.0002	977.11	0.02
307.32	12.3482	0.0002	8.8557	0.0002	8.9359	0.0002	977.16	0.02

316.43	12.3491	0.0002	8.8557	0.0002	8.9357	0.0002	977.21	0.02
325.53	12.3500	0.0002	8.8556	0.0002	8.9355	0.0002	977.24	0.02
334.71	12.3508	0.0002	8.8555	0.0002	8.9353	0.0002	977.26	0.02
343.83	12.3516	0.0002	8.8554	0.0002	8.9351	0.0002	977.30	0.02
352.90	12.3522	0.0002	8.8552	0.0002	8.9349	0.0002	977.31	0.02
362.05	12.3531	0.0002	8.8551	0.0002	8.9346	0.0002	977.34	0.02
371.18	12.3535	0.0002	8.8549	0.0002	8.9344	0.0002	977.33	0.02
380.27	12.3537	0.0002	8.8547	0.0002	8.9341	0.0002	977.28	0.02
389.42	12.3538	0.0002	8.8543	0.0002	8.9336	0.0002	977.20	0.02
398.55	12.3542	0.0002	8.8542	0.0002	8.9335	0.0002	977.20	0.02
407.60	12.3542	0.0002	8.8539	0.0002	8.9331	0.0002	977.13	0.02
416.73	12.3544	0.0002	8.8537	0.0002	8.9328	0.0002	977.09	0.02
425.82	12.3548	0.0002	8.8535	0.0002	8.9325	0.0002	977.07	0.02
434.93	12.3551	0.0002	8.8533	0.0002	8.9323	0.0002	977.04	0.02
444.05	12.3555	0.0002	8.8531	0.0002	8.9320	0.0002	977.03	0.02
453.21	12.3560	0.0002	8.8530	0.0002	8.9318	0.0002	977.03	0.03
462.30	12.3565	0.0002	8.8529	0.0002	8.9315	0.0002	977.03	0.02
471.36	12.3571	0.0002	8.8528	0.0002	8.9314	0.0002	977.05	0.03
480.36	12.3576	0.0002	8.8525	0.0002	8.9311	0.0002	977.02	0.03
489.42	12.3584	0.0002	8.8526	0.0002	8.9311	0.0002	977.09	0.03
498.15	12.3588	0.0002	8.8524	0.0002	8.9309	0.0002	977.08	0.02
500.04	12.3592	0.0002	8.8524	0.0002	8.9309	0.0002	977.10	0.02
500.03	12.3592	0.0002	8.8523	0.0002	8.9309	0.0002	977.11	0.03
500.00	12.3591	0.0002	8.8523	0.0002	8.9308	0.0002	977.09	0.02
498.91	12.3588	0.0002	8.8521	0.0002	8.9306	0.0002	977.02	0.02
489.18	12.3585	0.0002	8.8524	0.0002	8.9309	0.0002	977.07	0.03
479.98	12.3579	0.0002	8.8525	0.0002	8.9310	0.0002	977.04	0.02
470.41	12.3571	0.0002	8.8526	0.0002	8.9312	0.0002	977.01	0.02
461.29	12.3563	0.0002	8.8526	0.0002	8.9312	0.0002	976.95	0.02
452.17	12.3558	0.0002	8.8528	0.0002	8.9314	0.0002	976.95	0.02
443.07	12.3551	0.0002	8.8529	0.0002	8.9315	0.0002	976.92	0.02
433.95	12.3544	0.0002	8.8530	0.0002	8.9317	0.0002	976.90	0.02
424.85	12.3536	0.0002	8.8531	0.0002	8.9319	0.0002	976.86	0.02
415.68	12.3530	0.0002	8.8532	0.0002	8.9320	0.0002	976.84	0.02
406.64	12.3523	0.0002	8.8533	0.0002	8.9322	0.0002	976.81	0.02
397.46	12.3515	0.0002	8.8534	0.0002	8.9324	0.0002	976.78	0.02
388.35	12.3507	0.0002	8.8535	0.0002	8.9325	0.0002	976.75	0.02
379.24	12.3501	0.0002	8.8537	0.0002	8.9327	0.0002	976.74	0.02
370.21	12.3495	0.0002	8.8538	0.0002	8.9329	0.0002	976.72	0.02
361.05	12.3484	0.0002	8.8539	0.0002	8.9331	0.0002	976.66	0.02
351.81	12.3475	0.0002	8.8540	0.0002	8.9333	0.0002	976.63	0.02
342.70	12.3467	0.0002	8.8541	0.0002	8.9335	0.0002	976.59	0.02
333.65	12.3456	0.0002	8.8541	0.0002	8.9337	0.0002	976.54	0.03
324.43	12.3448	0.0002	8.8543	0.0002	8.9339	0.0002	976.52	0.02
315.35	12.3440	0.0002	8.8544	0.0002	8.9341	0.0002	976.49	0.02
306.20	12.3431	0.0002	8.8546	0.0002	8.9344	0.0002	976.46	0.02
297.05	12.3422	0.0002	8.8546	0.0002	8.9346	0.0002	976.42	0.02
287.89	12.3413	0.0002	8.8547	0.0002	8.9349	0.0002	976.39	0.02
278.79	12.3404	0.0002	8.8548	0.0002	8.9351	0.0002	976.35	0.02
269.64	12.3394	0.0002	8.8549	0.0002	8.9353	0.0002	976.31	0.02

260.56	12.3385	0.0002	8.8549	0.0002	8.9355	0.0002	976.27	0.02
251.45	12.3378	0.0002	8.8551	0.0002	8.9358	0.0002	976.25	0.02
242.30	12.3369	0.0002	8.8551	0.0002	8.9360	0.0002	976.21	0.02
233.17	12.3360	0.0002	8.8552	0.0002	8.9362	0.0002	976.17	0.02
224.08	12.3351	0.0002	8.8553	0.0002	8.9364	0.0002	976.13	0.02
214.96	12.3343	0.0002	8.8554	0.0002	8.9366	0.0002	976.10	0.02
205.86	12.3334	0.0002	8.8554	0.0002	8.9368	0.0002	976.05	0.02
196.74	12.3325	0.0002	8.8554	0.0002	8.9370	0.0002	976.01	0.02
187.60	12.3315	0.0002	8.8553	0.0002	8.9371	0.0002	975.92	0.02
178.47	12.3308	0.0002	8.8556	0.0002	8.9374	0.0002	975.93	0.02
169.38	12.3299	0.0002	8.8556	0.0002	8.9376	0.0002	975.88	0.02
160.24	12.3291	0.0002	8.8556	0.0002	8.9378	0.0002	975.85	0.02
151.40	12.3283	0.0002	8.8556	0.0002	8.9379	0.0002	975.80	0.02
143.76	12.3277	0.0002	8.8557	0.0002	8.9381	0.0002	975.77	0.02
137.46	12.3271	0.0002	8.8556	0.0002	8.9382	0.0002	975.73	0.02
132.08	12.3268	0.0002	8.8557	0.0002	8.9383	0.0002	975.73	0.02
127.44	12.3263	0.0002	8.8557	0.0002	8.9384	0.0002	975.70	0.02
123.68	12.3259	0.0002	8.8557	0.0002	8.9385	0.0002	975.68	0.02
120.51	12.3258	0.0002	8.8557	0.0002	8.9385	0.0002	975.67	0.02
119.88	12.3256	0.0002	8.8557	0.0002	8.9385	0.0002	975.65	0.02
119.98	12.3256	0.0002	8.8557	0.0002	8.9385	0.0002	975.66	0.02
131.59	12.3262	0.0002	8.8556	0.0002	8.9382	0.0002	975.65	0.02
148.34	12.3277	0.0002	8.8557	0.0002	8.9381	0.0002	975.77	0.02
164.77	12.3291	0.0002	8.8556	0.0002	8.9377	0.0002	975.84	0.02
181.27	12.3307	0.0002	8.8556	0.0002	8.9374	0.0002	975.93	0.03
197.68	12.3322	0.0002	8.8555	0.0002	8.9371	0.0002	975.99	0.03
214.20	12.3336	0.0002	8.8553	0.0002	8.9367	0.0002	976.05	0.02
230.52	12.3352	0.0002	8.8552	0.0002	8.9363	0.0002	976.12	0.02
246.99	12.3367	0.0002	8.8551	0.0002	8.9359	0.0002	976.18	0.02
263.35	12.3382	0.0002	8.8549	0.0002	8.9355	0.0002	976.24	0.02
279.84	12.3398	0.0002	8.8548	0.0002	8.9351	0.0002	976.31	0.02
296.21	12.3413	0.0002	8.8547	0.0002	8.9348	0.0002	976.39	0.02
298.17	12.3417	0.0002	8.8546	0.0002	8.9348	0.0002	976.40	0.02

CHAPTER 3

HIGH PRESSURE DIFFRACTION STUDY OF $Hf_2(PO_4)_2(SO_4)$, A MEMBER OF THE $A_2M_3O_{12}$ FAMILY

3.1 Introduction

Oxide frameworks exhibiting negative thermal expansion have recently received much attention from the scientific community.[1-15] Other than their scientific interest, NTE materials may be used in the manufacture of controlled thermal expansion composites, possibly resulting in materials exhibiting zero thermal expansion.[16-19] However, in the preparation and use of these composites, the NTE phase may experience quite high pressures. Under pressure, the structures of these materials may change, altering their thermal expansion characteristics and possibly eliminating NTE altogether. It is common for members of the AM_2O_8, AX_2O_7, and $A_2M_3O_{12}$ families, to undergo crystalline to crystalline transitions, and crystalline to amorphous transitions, otherwise known as pressure induced amorphization (PIA).[20-38] The transitions observed in these materials may be related to the low density and the high framework flexibility that is commonly found for NTE materials. It has also been shown that the phonon modes responsible for the negative Grüneisen parameters, needed for NTE, soften upon the reduction of the volume.[39-46] Pressure induced crystalline phase transitions and PIA will change the expansion properties.[47, 48]

High pressure experiments on NTE materials were initially performed on ZrW_2O_8, [20, 21, 49, 50] $ZrMo_2O_8$, [23, 51-53] and ZrV_2O_7[30] with work on the orthorhombic members of the $A_2M_3O_{12}$ family occurring later. At high pressures, $Sc_2W_3O_{12}$, [27, 54] $Sc_2Mo_3O_{12}$, [32, 37] and $Lu_2W_3O_{12}$[34] have been found to undergo an irreversible PIA that is complete by ~8 GPa, while $Al_2W_3O_{12}$[26, 55, 56] exhibits crystalline to crystalline transitions at 0.28 and 2.8 GPa.

The orthorhombic $A_2M_3O_{12}$ framework substitutions is amenable to generating a series of materials similar to $Sc_2W_3O_{12}$ reported in space group *Pnca*, such as $(ErIn)W_3O_{12}$, [3] $(HfMg)W_3O_{12}$, [57] $(ScAl)W_3O_{12}$, [3] $Zr_2(PO_4)_2(MoO_4)$, [3] $Zr_2(PO_4)_2(WO_4)$, [3] and $Zr_2(PO_4)_2(SO_4)$.[58] Recent high pressure studies of $Zr_2(PO_4)_2(WO_4)$ have shown that the material undergoes a phase transition from orthorhombic to monoclinic above 1.37 GPa, a transition to a second monoclinic phase above 3.7 GPa, and a transition to a triclinic phase above 7.4 GPa.[28] Above 14 GPa this material was found to undergo an irreversible transition to an amorphous phase.[28]

In the previous chapter, we found that $Zr_2(PO_4)_2(SO_4)$ does not display negative thermal expansion like most other members of this family, but is instead a low positive thermal expansion material with $\alpha_V = 3.88(5) \times 10^{-6}\ K^{-1}$. Additionally, contrary to previous reports, we found that this material, while still metrically orthorhombic, does not belong to space group *Pnca,* like the other members of this family. It is likely that $Hf_2(PO_4)_2(SO_4)$ will behave similarly to $Zr_2(PO_4)_2(SO_4)$, but no work on this material has been reported. This chapter focuses on the newly synthesized hafnium analog, and how it behaves under pressure.

3.2 Experimental

3.2.1 Preparation of $Hf_2(PO_4)_2(SO_4)$

$HfOCl_2 \cdot 8H_2O$ (Alfa Aesar), H_3PO_4 (Baker), and HNO_3 (Fisher) were used as purchased. A modification of the procedure reported by Piffard *et al.* for $Zr_2(PO_4)_2(SO_4)$ was used to make a hafnium phosphate gel.[58] A solution of 1 M H_3PO_4 was added to a solution containing both 0.4 M $HfOCl_2 \cdot 8H_2O$ and 0.1 M HNO_3 in a stoichiometric ratio of 10:4:1 for phosphorus, hafnium, and nitric acid. The resulting white gel was placed in an open top container in an oven at 125 ºC for 90 min in air. The oven temperature was then lowered to 95 ºC and kept there for 5 h, producing a white cake-like gel. Care was taken to not overheat the gel and form HfP_2O_7. The hafnium content of the gel was estimated from the weight of the recovered gel, assuming that all of the initially added hafnium was recovered. The resulting material contained 0.304 g hafnium per gram of gel. It was ground using a mortar and pestle and stored for subsequent use.

Samples of $Hf_2(PO_4)_2(SO_4)$ were prepared by a modification of the procedure reported by Piffard *et al.*[58] H_2SO_4 (VWR) was used as purchased. In a Teflon-lined autoclave, 12 mL of concentrated H_2SO_4 was added to 1.657 g of the dried hafnium phosphate gel to form a suspension. Immediately upon the addition of H_2SO_4, a yellowish tint in the solution was noticed along with the evolution of a gas. After stirring the mixture, the autoclave was sealed and placed in an oven at 225 ºC. After four days, the oven was turned off and the autoclave was cooled to room temperature in the oven. The autoclave contained a yellow-orange clear solution over a white powder. The final product was recovered by filtration. It was washed with 20 mL H_2SO_4, followed by 2 x 20 mL acetonitrile, and finally air dried overnight.

3.2.2 Laboratory Powder X-ray Diffraction

Room temperature powder X-ray diffraction measurements were performed on a Scintag diffractometer equipped with a copper tube and a Peltier cooled solid state detector. Data were collected over the range of 5-90º 2θ, at a rate of 2º/min.

3.2.3 Thermogravimetric Analysis

TGA measurements were performed on the Perkin Elmer TGA 7 Thermogravimetric Analyzer. Data were collected from 30-800 ºC at a rate of 3.3 ºC/min under a nitrogen atmosphere using a platinum pan as a sample holder.

3.2.4 Variable Pressure Powder X-ray Diffraction Measurements

Data were collected on $Hf_2(PO_4)_2(SO_4)$ at room temperature at up to ~9 GPa in a Diacell Bragg-(S) two screw DAC. The diamonds in this beryllium backed cell had 600 μm culets. A stainless steel, pre-indented gasket 111 μm thick was drilled using EDM to have a 285 μm diameter hole. Before loading, the samples were ground using a mortar and pestle to reduce the grain size of the sample, and, hence, improve the powder sampling statistics. A 4:1 mixture of methanol to ethanol was used as the pressure transmitting medium. This medium was chosen because it is reported to be hydrostatic up to 10.4 GPa, slightly above the maximum desired pressure.[59] Diffraction data were collected at the Advanced Photon Source, Argonne National Lab, beam line 1-BM-C using x-rays with λ= .61832 Å. 2D diffraction images were recorded on a MAR 345 detector. Each exposure lasted 45 s followed by time to read the data off of the image plate totaling 140s. Data were collected at sample to plate distances of ~300 mm and ~450 mm. The sample to plate distances were calibrated using LaB_6.[60] The shorter sample to plate distance gives a lower minimum d-spacing and the larger sample to plate

distance gives superior angular resolution. The pressure was increased manually after each set of measurements. The pressure in the DAC was estimated using the ruby fluorescence technique. The reported pressure is the average of those determined before and after each exposure.[61] Errors in pressure calibration for the ruby fluorescence technique have been shown to vary between 0.05 and 0.1 GPa.[59] FIT-2D was used to integrate the image plate data.[62] Le Bail fits to the data were performed using the program GSAS with the EXPGUI interface.[63, 64] Pressure-volume data were fit with a third-order Birch-Murnaghan equation of state using EOS-FIT 5.2.[65]

3.3 Results

3.3.1 Laboratory X-ray Powder Diffraction

Reaction of the hafnium gel in sulfuric acid, resulted in a white product that could not be identified using the ICDD database as a known hafnium containing phase. However, the diffraction data matched with that for $Zr_2(PO_4)_2(SO_4)$ (ICDD #00-041-0032) and as hafnium and zirconium have similar structural chemistry, this supports that the material was $Hf_2(PO_4)_2(SO_4)$. Figure 3.1 shows a Rietveld fit of a $Zr_2(PO_4)_2(SO_4)$ type model to observed diffraction data. Initial atomic coordinates were those reported for $Zr_2(PO_4)_2(SO_4)$, substituting Hf in place of Zr. The model gave a good fit to the data, strongly suggesting that $Hf_2(PO_4)_2(SO_4)$ is essentially isostructural with $Zr_2(PO_4)_2(SO_4)$.

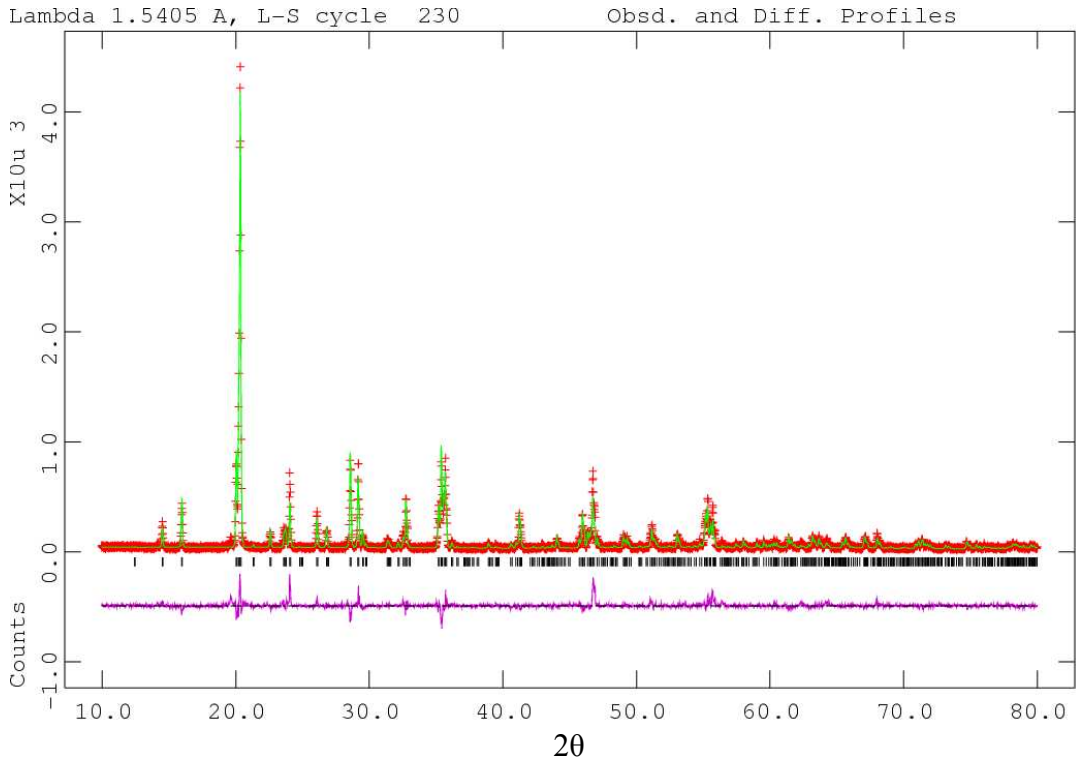

Figure 3.1. Powder x-ray diffraction data for $Hf_2(PO_4)_2(SO_4)$, taken at room temperature (λ = 1.5405 Å), in red, compared to the Rietveld model in space group *Pbcn* (green). The difference curve is shown in purple. Reflections expected for space group *Pbcn* are shown in black.

3.3.2 *In-situ* High Pressure Diffraction Measurements

X-ray powder diffraction patterns inside of the diamond anvil cell were collected from ambient pressure up to 8.23 GPa at λ = 0.61832 Å. Initial test diffraction patterns taken for $Hf_2(PO_4)_2(SO_4)$ showed were very spotty Debye rings. The sample was ground further in order to reduce the graininess of the sample. However, after grinding, no improvement was seen in the Debye rings, and the experiment was conducted with less than ideal sampling statistics.

A closer examination of the low angle diffraction pattern of $Hf_2(PO_4)_2(SO_4)$ (Figure 3.2) shows reflections at 2.87, 3.96, 4.92, 5.60, and 5.64º 2θ. The reflections expected for space group *Pbcn* are marked in black, while the reflections predicted for space group

P222 are marked in red. In the previous chapter, we were able to show that $Zr_2(PO_4)_2(SO_4)$ does not crystallize in space group *Pbcn* as previously reported. We suggested that $Zr_2(PO_4)_2(SO_4)$ crystallizes in one of the following space groups: *P222, P22m, P2mm,* or *Pmmm*. With the appearance of extra reflections in the pattern for $Hf_2(PO_4)_2(SO_4)$, we suggest that the hafnium analog behaves similarly to $Zr_2(PO_4)_2(SO_4)$.

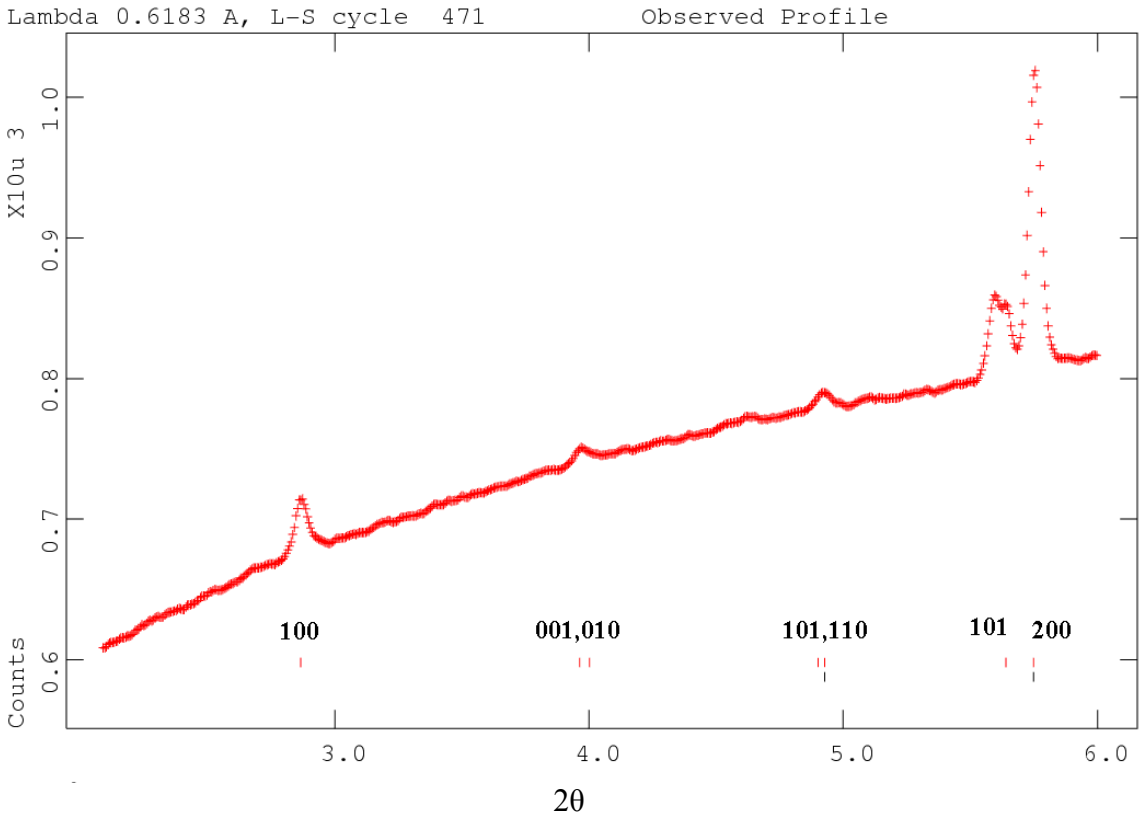

Figure 3.2. Low angle portion of the x-ray powder diffraction pattern collected for $Hf_2(PO_4)_2(SO_4)$ at ambient pressure. The reflections expected for space group *Pbcn* are in black (bottom of figure), while those expected for space group *P222* are marked in red (bottom of figure).

Powder diffraction patterns were collected inside of a two screw diamond anvil cell. The diffraction data acquired with a sample to plate distance of 450 mm were fit using GSAS with the EXPGUI interface, using the Le Bail method in space group *P222*.[63, 64] The unit cell constants from the fits are shown in Table 3.1.

Table 3.1. Lattice constants of orthorhombic $Hf_2(PO_4)_2(SO_4)$ as a function of pressure. Data were obtained using a 4:1 methanol to ethanol mixture as a pressure transmitting medium. The lattice constants were calculated from the Le Bail fit to the diffraction pattern in space group *P222* at the ~450mm sample to detector distance. Lattice constants collected at 1.30, 2.17, 3.33, 5.79, 6.53, 7.25, and 7.55GPa were estimated by Le Bail fits with the angular range ~17-18º 2θ excluded from the fitdue to presence of gasket peaks in the data. Measurements on decompression were not made as the gasket failed.

Pressure, Gpa	a, Å	b, Å	c, Å	Volume Å^3
0.00	12.2922(2)	8.8242(1)	8.9040(1)	965.81(3)
0.23	12.2610(1)	8.8103(1)	8.8917(1)	960.52(1)
0.57	12.2157(2)	8.7918(2)	8.8746(2)	953.12(5)
1.30	12.1310(3)	8.7245(2)	8.8199(3)	933.48(7)
2.17	12.0347(11)	8.6464(8)	8.7530(7)	910.81(21)
2.53	12.0053(8)	8.6231(6)	8.7234(6)	903.07(17)
2.88	11.9689(9)	8.5945(7)	8.6918(7)	894.10(18)
3.33	11.9304(9)	8.5664(7)	8.6620(6)	885.25(18)
4.14	11.8428(12)	8.4948(8)	8.5851(8)	863.68(23)
4.74	11.7925(11)	8.4601(8)	8.5438(7)	852.38(20)
5.47	11.7158(12)	8.3978(8)	8.4796(7)	834.28(22)
5.79	11.7054(13)	8.3918(10)	8.4706(8)	832.07(24)
6.53	11.6231(12)	8.3241(9)	8.4117(7)	813.84(22)
6.97	11.5611(11)	8.2773(8)	8.3799(7)	801.90(20)
7.25	11.5213(13)	8.2412(8)	8.3531(7)	793.13(21)
7.55	11.4878(9)	8.2194(4)	8.3306(4)	786.61(6)
7.90	11.4392(24)	8.1756(13)	8.2936(13)	775.65(36)
8.23	11.4159(30)	8.1518(14)	8.2690(16)	769.51(43)

Figure 3.3 shows the volume of the unit cell as a function of pressure. The volume varies almost linearly with pressure, and there is a ~20.3% volume reduction going on from ambient to 8.23 GPa. Fitting a third-order Birch-Murnaghan equation of state (EOS), gave a bulk modulus, K_0, of 36.9(6) GPa. The refined zero-pressure volume of the fit was 966.16(96) $Å^3$, while the pressure derivative of the bulk modulus was 0.92(9). When the pressure derivative is set at 4 in an attempt to obtain a fit to the Birch-Murnaghan EOS, the calculated V_0 changes by ~3% and the overall fit is poor.

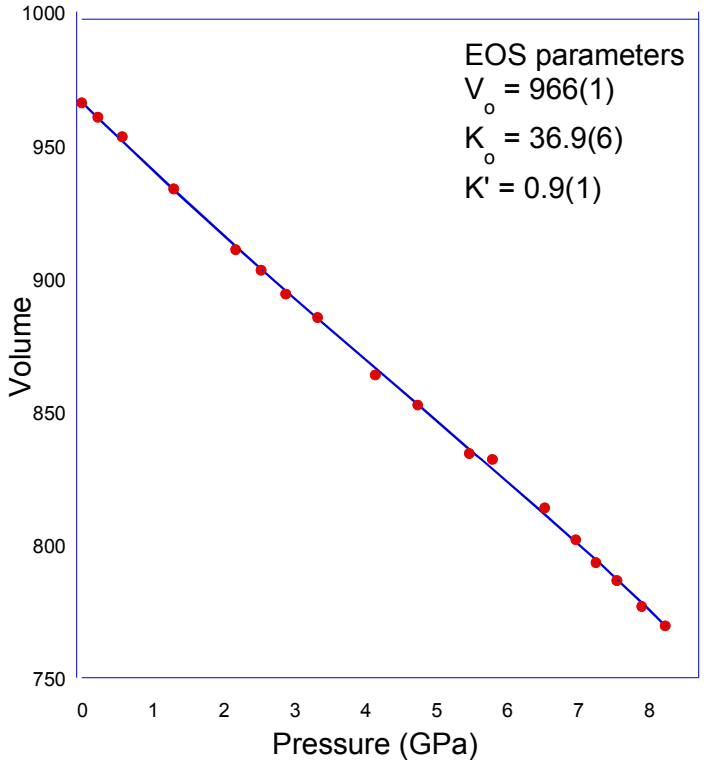

Figure 3.3. Volume vs. pressure for $Hf_2(PO_4)_2(SO_4)$ from 0 - 8.23 GPa. The point at 0 GPa was the first pressure point and was taken in the closed cell with no pressure transmission fluid. The pressure recorded in the absence of fluid was subtracted from the subsequent pressure measurements to account for spectrometer miscalibration.

Figure 3.4, shows normalized lattice constants as a function of pressure. From ambient pressure up to 0.57 GPa, the *a* axis is the most compressible, while *b* and *c* are compressed at roughly the same rate. Between 0.57 GPa and 1.30 GPa, lattice parameter *b* separates itself from *c*. This change in the compression of the lattice constants suggests a possible phase transition in the material. Above 2.17 GPa, *a* and *b* are practically isocompressible with *b* becoming the softest axis above 3.33 GPa. *b* remains the most compressible until the end of the experiment. Between 4.74 GPa and 6.53 GPa, *c* becomes more compressible than *a*, but above 6.53 GPa, *a* again becomes the more compressible axis. This suggests the possibly of another phase transition in the material. Linear compressibilities were estimated by plotting the natural log of the parameters versus the pressure up to 8.23 GPa, β_a is 8.74(10) x 10^{-3} GPa^{-1}, β_b is 9.47(13) x 10^{-3} GPa^{-1}, and β_c is 9.04(7) x 10^{-3} GPa^{-1}.

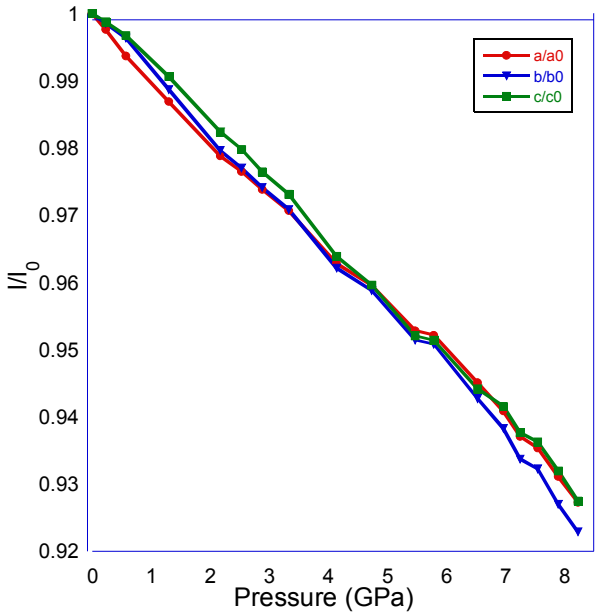

Figure 3.4. Normalized lattice constants as a function of pressure for $Hf_2(PO_4)_2(SO_4)$ up to 8.23 GPa. The line is only to be used to follow the points.

Further examination of the two-dimensional diffraction patterns, shown in Figure 3.5, reveals the formation of an additional Debye ring as the pressure is increased. As the pressure goes above 0.57 GPa, the Debye ring gets stronger and stronger suggesting that the additional peak is not from an impurity in the sample. The additional peak is more clearly seen above 2.88 GPa as the intensity of the Debye ring becomes stronger. At 5.47 GPa, the ring on this two dimensional pattern has an intensity slightly lower than the surrounding rings.

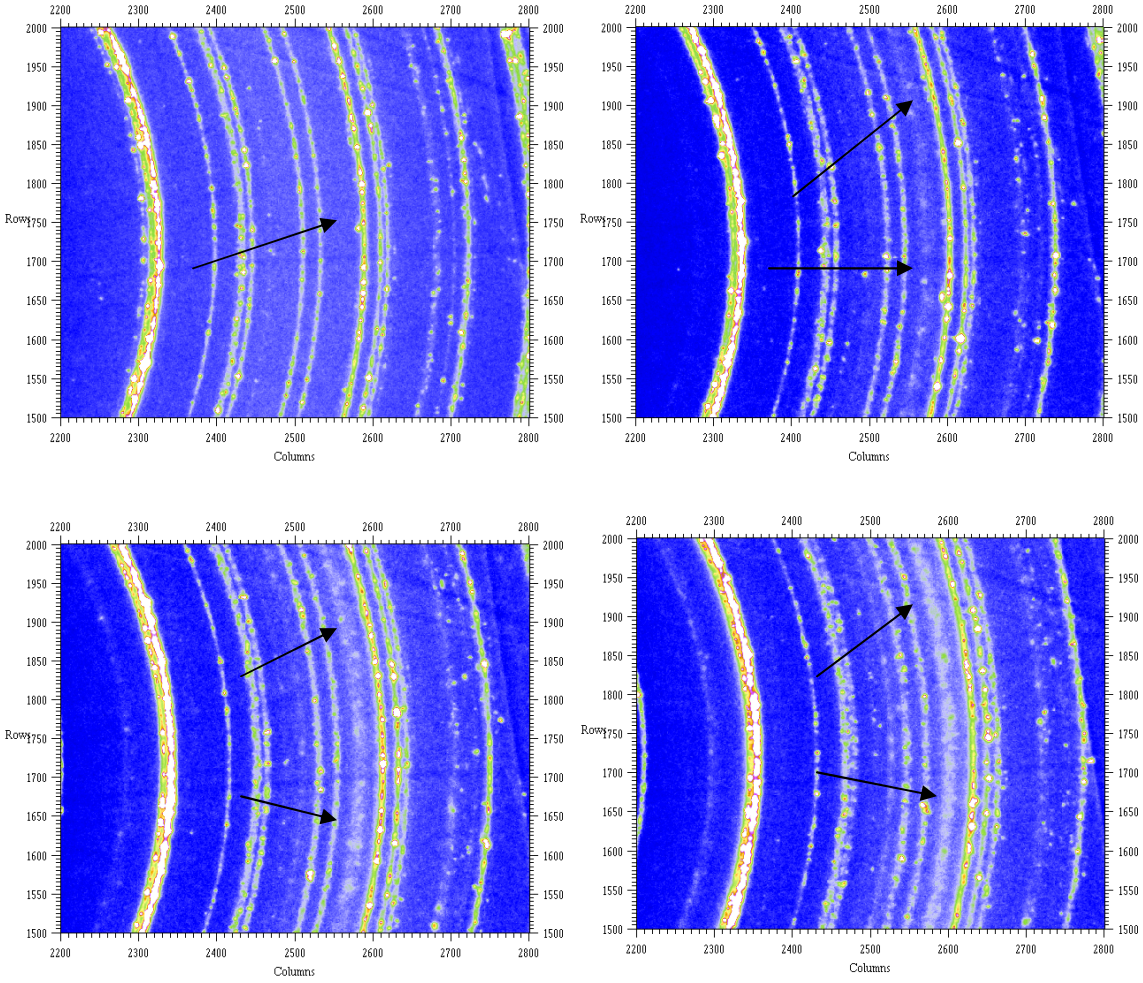

Figure 3.5. Zoomed in 2-D x-ray diffraction pattern collected from $Hf_2(PO_4)_2(SO_4)$ at 0.57GPa (top left), 2.17 GPa (top right), 2.88 GPa (bottom left), and 5.47 GPa (bottom right) showing the appearance of an unknown peak.

In the one-dimensional patterns (see Figures 3.6 to 3.8) the appearance of additional peaks becomes much more apparent. Data collected for $Hf_2(PO_4)_2(SO_4)$ modeled with a Lebail fit in space group *P222* are in good general agreement for each of the data sets collected up to 0.57 GPa, as seen in Figure 3.6. There also appear to be no additional reflections that cannot be explained in this low symmetry orthorhombic space group.

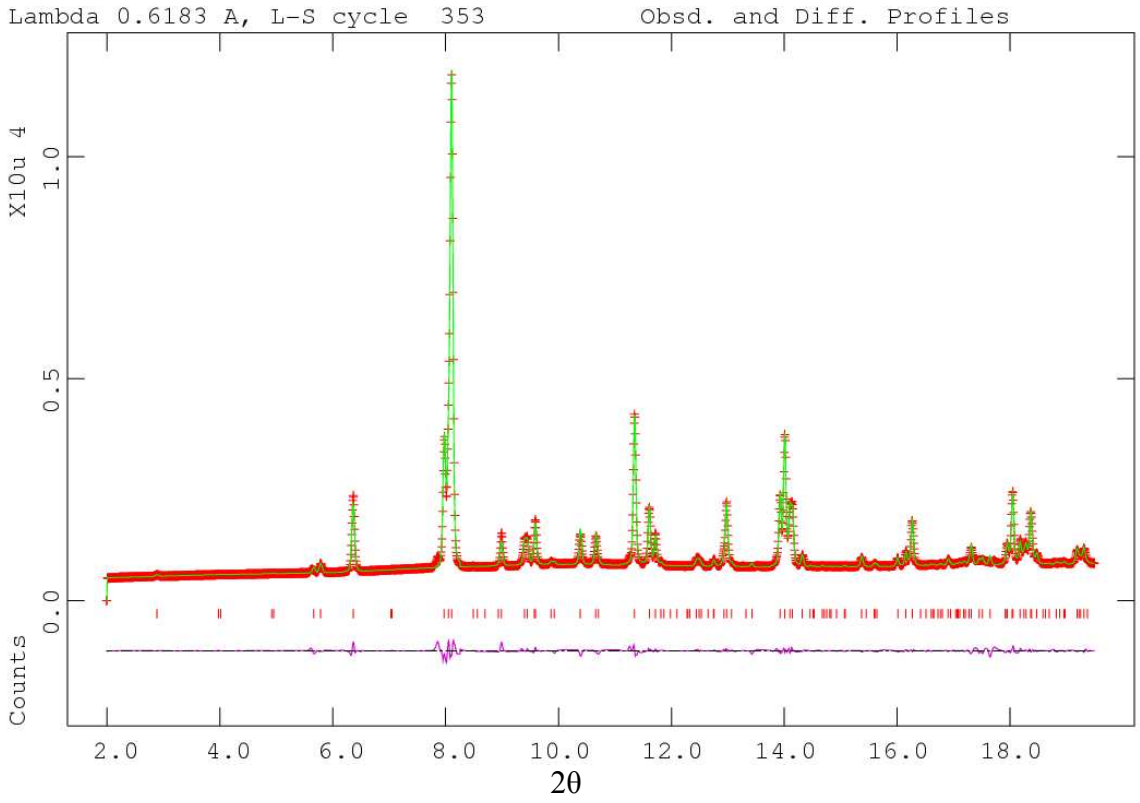

Figure 3.6. X-ray diffraction pattern of $Hf_2(PO_4)_2(SO_4)$ taken at 0.57 GPa during a powder x-ray experiment at λ= 0.61832 Å (red), compared to the Le Bail fit in space group *P222* (green). The difference curve is shown in purple.

As the pressure is increased further, the Le Bail fits to the diffraction patterns get much worse. Figure 3.7 shows the diffraction pattern for $Hf_2(PO_4)_2(SO_4)$ collected at 3.33 GPa. The diffraction pattern is in poor agreement with the Le Bail fit, when compared to the pattern collected at 0.57 GPa. A couple of new reflections become clearly visible at ~7.54, 10.23, and 11.25º 2θ. These reflections do not correspond to any possible reflections for space group *P222*. These extra peaks are presumably not due to an impurity, as they were not present at lower pressure. The reflections are not from the ruby chips in the sample, as comparison to the ICDD database #01-071-0958 only gives one

reflection close to these peaks at 10.17º 2θ, which under pressure would be shifted to lower d-spacing. These peaks are also not due to the presence of gasket in the x-ray beam as all of the diffraction patterns show these peaks at higher pressure and only a few of them had gasket in the sample. This leaves the possibility that the material undergoes a phase transition and is being fit in the wrong space group.

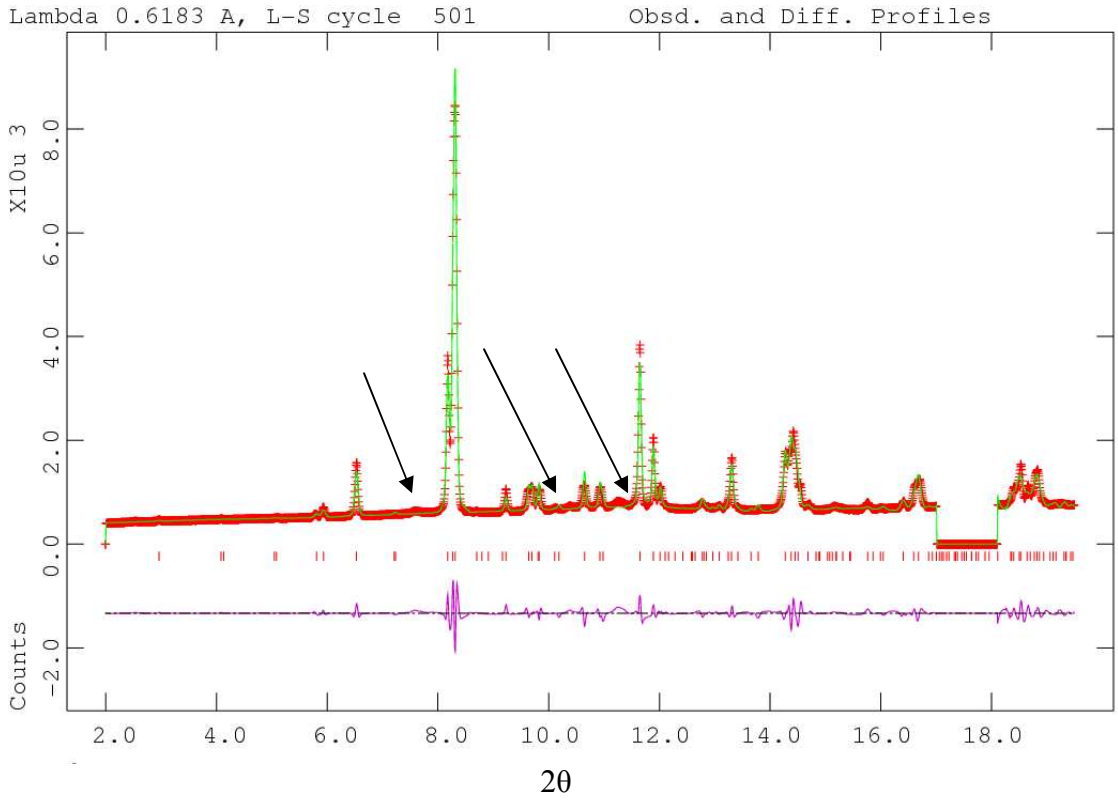

Figure 3.7. X-ray diffraction pattern of $Hf_2(PO_4)_2(SO_4)$ taken at 3.33 GPa during a powder x-ray experiment at λ = 0.61832 Å (red), compared to the Le Bail fit in space group *P222* (green). The difference curve is shown in purple. Extra peaks of an unknown phase or impurity are marked by black arrows. The data ranging from 17 – 18º 2θ had to be removed during fitting due to gasket interference with the x-ray beam.

For the remainder of the experiment, as pressure is increased, the data were fit using space group *P222*. While the diffraction peaks shift to lower d spacings, there is no evidence of pressure induced amorphization. We do not know if the observed changes are reversible on decompression as the gasket failed upon compression.

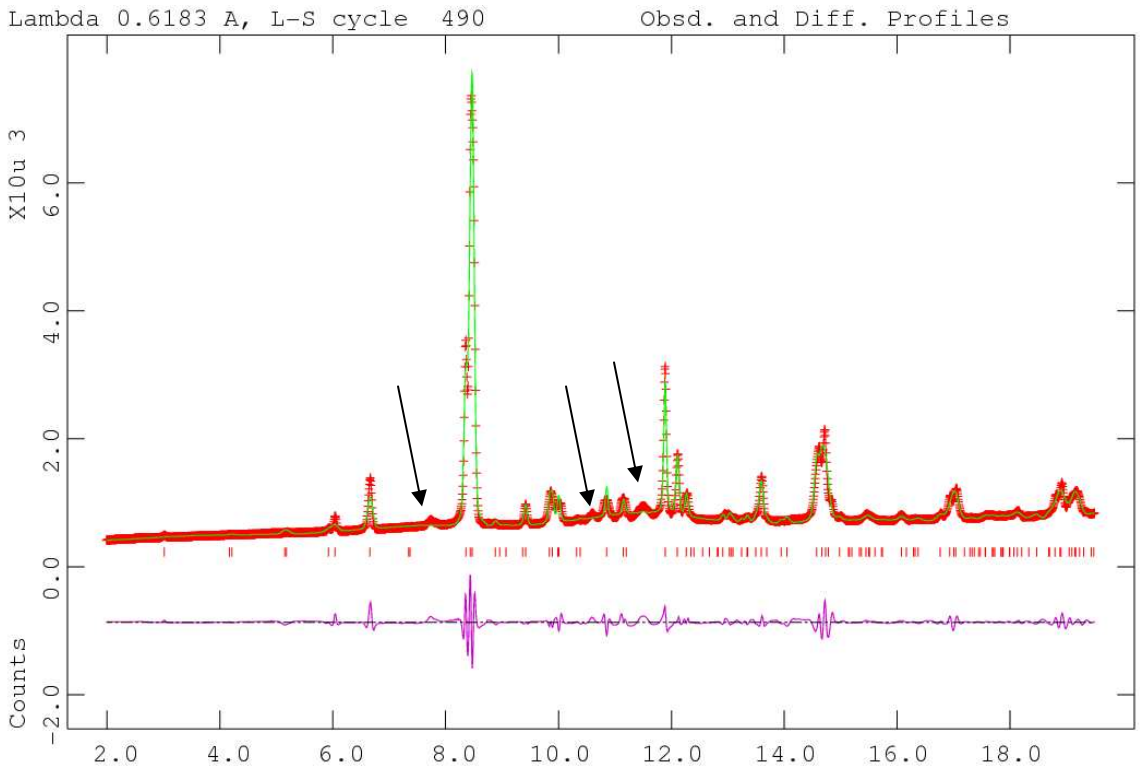

Figure 3.8. X-ray diffraction pattern of $Hf_2(PO_4)_2(SO_4)$ taken at 5.47 GPa during a powder x-ray experiment at $\lambda = 0.61832$ Å (red), compared to the Le Bail fit in space group *P222* (green). The difference curve is shown in purple. Extra peaks of an unknown phase or impurity are marked by black arrows.

3.3.3 Thermogravimetric Measurements

The TGA for $Hf_2(PO_4)_2(SO_4)$ is presented in Figure 3.9. It is very similar to that displayed for $Zr_2(PO_4)_2(SO_4)$ (Figure 2.2). The first significant weight loss occurs in the range 30 to 100 ºC (1.12% of its initial mass). As this weight loss occurs below 100 ºC, and the material was stored in an open atmosphere, it is probably due to the loss of absorbed water on the material (0.42 moles of water per mole of sample).

The next weight loss in the material occurs from 130 to 200 ºC and causes the percentage of initial mass to go from 98.54% to 96.32%. Being similar to the Zr product in both size and structure, according to the x-ray diffraction patterns, and knowing that Zr and Hf behave similarly chemically being in the same group, we reasoned that this weight loss corresponds to a loss of water as discussed in the previous chapter. While it is unlikely that water is actually lodged within the crystal, some hydroxyl groups may be in the framework. As the hydroxyls are heated they recombine to form water. While this is not definite because we do not have other *in-situ* temperature measurements on this sample, we suspect that because Hf and Zr are extremely similar in character that this weight loss is similar in both materials. Thus the 2.22% weight loss corresponds to 0.78 moles of water lost per mole of sample. If this is the situation, it suggests that there are defects in the crystal and that the material is not pure $Hf_2(PO_4)_2(SO_4)$ and instead a hydroxyl containing derivative. Another possibility is that the weight loss is derived from some impurity in the sample, but powder x-ray diffraction measurements suggest that the material has little to no visible impurities.

The next significant weight loss occurs from 460 to 530 ºC making the percentage of initial mass go from 95.65% to 94.17%. Assuming all water/hydroxyl groups have been

removed from the sample and no obvious reduction has occurred in the material, the weight loss corresponds to the loss of a neutral gas, most likely SO_3. The 1.48% loss thus corresponds to 0.14 moles of SO_3 gas per mole of sample, and is the beginning of sample decomposition.

From 530 ºC until the end of the experiment the material is undergoing constant weight loss. This may be associated with further loss of SO_3. Future *in-situ* high temperature diffraction measurements may shed light on these decomposition processes.

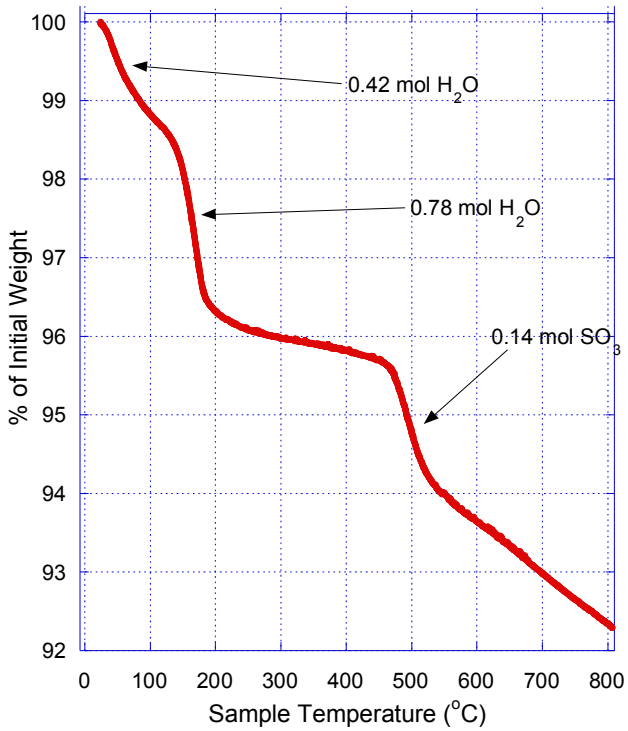

Figure 3.9. TGA of $Hf_2(PO_4)_2(SO_4)$. The sample to 800 ºC at 3.3 ºC/min under a nitrogen atmosphere.

3.4 Discussion

In the reaction of the hafnium phosphorus gel with sulfuric acid, it was noted that gas was evolved upon the addition of sulfuric acid to the gel. This was not observed in our $Zr_2(PO_4)_2(SO_4)$ syntheses. A possible reason for gas evolution, is the presence of chloride in the hafnium gel. Upon the addition of sulfuric acid, the chloride ions form HCl, which is lost from the reaction vessel. A similar result was noted when the zirconium gel was made from $ZrOCl_2 \cdot 8H_2O$. The discoloration in the solution over the final product suggests that an impurity was present in the reaction vessel before it was placed in the oven. However, there was no apparent adverse effect on the formation of $Hf_2(PO_4)_2(SO_4)$.

The ambient pressure x-ray diffraction patterns of $Hf_2(PO_4)_2(SO_4)$ were examined closely for extra peaks. As with the zirconium derivative, a small shoulder was initially seen on the left side of the first visible peak at 14.40º 2θ, suggesting the presence of an extra peak not allowed in space group *Pbcn*. At low angles, in the diffraction pattern (Figure 4.3.2), (100), (010), (001), (101) and (011) reflections were also visible. These suggest that $Hf_2(PO_4)_2(SO_4)$ does not crystallize in the *Pbcn* space group as reported for $Zr_2(PO_4)_2(WO_4)$[15, 66], $Zr_2(PO_4)_2(MoO_4)$[3], $Sc_2(WO_4)_3$[67]. These additional reflections are similar to those in $Zr_2(PO_4)_2(SO_4)$. Hafnium and zirconium have been found to be largely interchangeable within materials exhibiting negative thermal expansion as they belong to the same group and only differ in atomic radius by 0.01 Å. Similar thermal expansion coefficients have been reported for $HfMo_2O_8$[68] and $ZrMo_2O_8$[4], and additionally most starting chemicals containing hafnium or zirconium contain up to 2% of the other metal. Thus it is not unreasonable that both of these phosphate-sulfates exhibit similar structures.

Upon increasing the pressure, the diffraction data for $Hf_2(PO_4)_2(SO_4)$ could be modeled using the orthorhombic space group *P222,* giving generally good agreement between the diffraction patterns and the model up to 0.57 GPa. Above this pressure, extra peaks became visible in the diffraction patterns that could not be attributed to the orthorhombic phase. The slow appearance of peaks at ~7.54, 10.23, and 11.25º 2θ suggest that these peaks are not the result of an impurity in the sample, since they are not present at low pressures, and they increase in intensity as the pressure is increased. The appearance of these peaks is not due to the ruby chips added to the sample, as some of the peaks expected for ruby are not present. The slow appearance of the additional peaks, suggests that this material is going through a phase transition that may be similar to other members of the $A_2M_3O_{12}$ family. $Sc_2W_3O_{12}$[35, 69] has been shown to go from orthorhombic to monoclinic at 0.32 GPa in isopropanol, while $Al_2W_3O_{12}$[36], $Zr_2(PO_4)_2(WO_4)$[28], and $Zr_2(PO_4)_2(MoO_4)$[70] have a transition from orthorhombic to monoclinic at ~ 0.1, 1.4, and 1.5 GPa respectively. We have not been able to identify a unit cell for this new phase.

Further evidence for a phase transition in the material is provided by the behavior of the unit cell volume and the lattice constants as a function of pressure. Their dependence on the pressure is rather unusual. When the P-V data were fit to a third order Birch-Murnaghan EOS, the pressure derivative of the bulk modulus was found to be 0.92(9). For a typical material this value is often 4. When the lattice constants are normalized and plotted versus the pressure, it can be seen that the *b* and *c* lattice parameters of the unit cells are compressed at a nearly identical rate up to 0.57 GPa. Above this pressure these lattice parameters diverge and *b* becomes more compressible than *c*, and eventually becomes the most compressible axis. This change in the compressibility is very similar to

that found for $Sc_2W_3O_{12}$[26], where two of the axis are isocompressible, but after a phase change at approximately 0.25 GPa have different values. Thus we believe that this material experiences a phase transition between 0.57 and 1.30 GPa, but we do not know the space group of the product phase.

Further examination of the normalized lattice constants reveals that between 3.33 and 5.47 GPa, all three axes become practically isocompressible again only to diverge above this pressure. As explained above, this sudden change in the compressibility may be correlated to a second phase transition. This was seen for $Zr_2(PO_4)_2(WO_4)$[28] which transforms to a second monoclinic phase at 6.3 GPa and for $Sc_2W_3O_{12}$[35] which goes to $P2_1/n$ at 2.7 GPa. The change in slope at this point of the volume versus pressure curve may be a sign of a second phase transition right at or above 5.47 GPa.

The estimated bulk modulus, K_0, of the material was 36.9(6) GPa. This is softer than that of $Al_2W_3O_{12}$[36], $Zr_2(PO_4)_2(WO_4)$[28], and $Zr_2(PO_4)_2(MoO_4)$[70] which have bulk moduli of 48, 49, and 45 GPa in their orthorhombic phases respectively. This material, however, is more comparable to the orthorhombic phase of $Sc_2(WO_4)_3$[35] and $Sc_2(MoO_4)_3$[71] which have bulk moduli of 31(3) and 32(2) GPa respectively. However, the estimated bulk modulus should be treated with suspicion as the pressure range employed in the fit may include one or more phase transitions.

TGA measurements of $Hf_2(PO_4)_2(SO_4)$ are very similar to those of $Zr_2(PO_4)_2(SO_4)$ as presented in the previous chapter. The initial weight loss between 30 and 100 ºC is suspected to be due to the loss of absorbed water. The flow of nitrogen gas would easily remove all water adsorbed on the material. Significantly this shouldn't change the reversibility of the lattice constants for this material as the temperature is cycled in this

range. However, no diffraction measurements have been taken while heating this material. The second weight loss observed between 130 and 200 ºC should be similar to the second weight loss seen for $Zr_2(PO_4)_2(SO_4)$. While we don't have the lattice constants at various temperatures, we suggest that this material, like the zirconium analog, will experience an irreversible change in the lattice parameters on heating as hydroxyl defects are eliminated from the material. If we assume that this structure has defects, we propose that our "$Hf_2(PO_4)_2(SO_4)$" sample is really either $Hf_{1.61}(OH)_{1.56}P_2SO_{10.44}$ or $Hf_2(OH)_{1.56}P_2S_{0.74}O_{10.44}$ but as the crystal density is not known for $Hf_2(PO_4)_2(SO_4)$, we cannot be sure as to what the actual formula of this material is. The crystal density of this material should, however, be higher than that of $Zr_2(PO_4)_2(SO_4)$ and may be difficult to measure by the floatation method as there are not as many readily available high density liquids. The final distinct weight loss from 460 to 530 ºC is also similar to the weight loss observed in the previous chapter, which we attributed to loss of a neutral gas such as SO_3. Thus we suggest that due to the similarity of hafnium and zirconium chemistry that this loss can be attributed to the same reason.

3.5 Conclusions

Examination of "$Hf_2(PO_4)_2(SO_4)$" has shown that like the zirconium derivative, this material is orthorhombic at ambient pressure, and has lower symmetry than *Pbcn* as reported by Piffard.[58] X-ray diffraction patterns displayed additional reflections at low angle that were not consistent with *Pbcn*. Upon increasing the pressure inside of the DAC, extra reflections suggesting a phase transition appear in the x-ray diffraction patterns. Phase transitions in this material are further indicated by the unusual pressure

derivative of the bulk modulus and changes in compressibility of the unit cell axes as the pressure is increased. We have suggested that "$Hf_2(PO_4)_2(SO_4)$" experiences at least one and possibly a second phase transition over the pressure range studied. If it is assumed that Zr and Hf are interchangeable in both size and chemical properties, $Zr_2(PO_4)_2(SO_4)$ should behave in a similar manner under pressure.

Additionally TGA measurements have been performed on "$Hf_2(PO_4)_2(SO_4)$" and show similar results to the zirconium derivative. The weight loss between 130 and 200 ºC suggests the loss of water from the material. This loss is either due to hydroxyl defects being present in the structure suggesting possible formulas of $Hf_{1.61}(OH)_{1.56}P_2SO_{10.44}$ or $Hf_2(OH)_{1.56}P_2S_{0.74}O_{10.44}$, or the decomposition of an amorphous impurity. Future work on this material may include *in-situ* variable temperature diffraction experiments, crystal density measurements, and single crystal diffraction measurements on high quality crystals.

3.6 References

1. Sleight, A. W., Compounds that Contract on Heating. *Inorg. Chem.* **1998,** 37, 2854-2860.

2. Evans, J. S. O.; Mary, T. A.; Sleight, A. W., Negative Thermal Expansion in $Sc_2(WO_4)_3$. *J. Solid State Chem.* **1998,** 137, 148-160.

3. Evans, J. S. O.; Mary, T. A.; Sleight, A. W., Negative Thermal Expansion in a Large Molybdate and Tungstate Family. *J. Solid State Chem.* **1997,** 133, 580-583.

4. Lind, C.; Wilkinson, A. P.; Hu, Z.; Short, S.; Jorgensen, J. D., Synthesis and Properties of the Negative Thermal Expansion Material Cubic Zirconium Molybdate. *Chem. Mater.* **1998,** 10, 2335-2337.

5. Baiz, T. I.; Gindhart, A. M.; Kraemer, S. K.; Lind, C., Synthesis of $MgHf(WO_4)_3$ and $MgZr(WO_4)_3$ using a non-hydrolytic sol-gel method. *J. Sol-Gel Sci. Tech.* **2008,** 47, 128-130.

6. Evans, J. S. O.; Mary, T. A.; Vogt, T.; Subramanian, M. A.; Sleight, A. W., Negative Thermal Expansion in ZrW_2O_8 and HfW_2O_8. *Chem. Mater.* **1996,** 8, 2809-2823.

7. White, K. M. Low Temperature Synthesis and Characterization of some Low positive and Negative Thermal Expansion Materials. Ph.D., Georgia Institute of Technology, Atlanta, 2006.

8. Pryde, A. K. A.; Hammonds, K. D.; Dove, M. T.; Heine, V.; Gale, J. D.; Warren, M. C., Origin of the Negative Thermal Expansion in ZrW_2O_8 and ZrV_2O_7. *J. Phys. Condens. Matter* **1996,** 8, 10973-10982.

9. Varga, T.; Wilkinson, A. P.; Haluska, M.; Payzant, E. A., Preparation and thermal expansion of $(M^{III}_{0.5}M'^{V}_{0.5})P_2O_7$ with the ZrP_2O_7 structure. *J. Solid State Chem.* **2005,** 178, 3541-3546.

10. Losilla, E. R.; Cabeza, A.; Bruque, S.; Aranda, M. A. G.; Sanz, J.; Iglesias, J. E.; Alonso, J. A., Syntheses, Structures, and Thermal Expansion of Germanium Pyrophosphates. *J. Solid State Chem.* **2001,** 156, 213-219.

11. Mary, T. A.; Evans, J. S. O.; Vogt, T.; Sleight, A. W., Negative Thermal Expansion from 0.3 to 1050 Kelvin in ZrW_2O_8. *Science* **1996,** 272, 90-92.

12. Rodrigo, J. L., Thermal Expansion of $NaTi_2(PO_4)_3$ Studied by Rietveld Method from X-ray Diffraction Data. *Mat. Res. Bull.* **1989,** 24, 611-618.

13. Oota, T.; Yamai, I., Thermal Expansion Behavior of $NaZr_2(PO_4)_3$-Type Compounds. *J. Am. Ceram. Soc.* **1986,** 69, 1-6.

14. Rodrigo, J. L.; Alamo, J., Phase Transitions in $NaSn_2(PO_4)_3$ and Thermal Expansion of $NaM_2^{IV}(PO_4)_3$; M^{IV} = Ti, Sn, Zr. *Mat. Res. Bull.* **1991,** 26, 475-480.

15. Evans, J. S. O.; Mary, T. A.; Sleight, A. W., Structure of $Zr_2(WO_4)(PO_4)_2$ from Powder X-ray Data: Cation Ordering with No Superstructure. *J. Solid State Chem.* **1995,** 120, 101-104.

16. Wetherfold, R. C.; Wang, J., Tailoring thermal deformation by using layered beams. *Compos. Sci. Technol.* **1995,** 53, 1-6.

17. Fleming, D. A.; Johnson, D. W.; Lemaire, P. J. Article Comprising a Temperature Compensated Optical Fiber Refractive Index Grating. 5,694,503, December 2, 1997, 1997.

18. Fleming, D. A.; Lemaire, P. J.; Johnson, D. W. Temperature compensated optical fiber refractive index grating. EP 97-306798 19970902, 1998.

19. Balch, D. K.; Dunand, D. C., Copper-Zirconium Tungstate Composites Exhibiting Low and Negative Thermal Expansion Influenced by Reinforcement Phase Transformations. *Metall. Mater. Trans. A* **2004,** 35A, 1159-1165.

20. Evans, J. S. O.; Hu, Z.; Jorgensen, J. D.; Argyriou, D. N.; Short, S.; Sleight, A. W., Compressibility, Phase Transitions, and Oxygen Migration in Zirconium Tungstate, ZrW_2O_8. *Science* **1997,** 275, 61-65.

21. Perottoni, C. A.; de Jornada, J. A. H., Pressure-Induced Amorphization and Negative Thermal Expansion in ZrW_2O_8. *Science* **1998,** 280, 886-889.

22. Grzechnik, A.; Crichton, W. A., Structural transformations in cubic $ZrMo_2O_8$ at high pressures and high temperatures. *Solid State Sci.* **2002,** 4, 1137-1141.

23. Muthu, D. V. S.; Chen, B.; Wrobel, J. M.; Krogh Andersen, A. M.; Carlson, S.; Kruger, M. B., Pressure-induced phase transitions in α–$ZrMo_2O_8$. *Phys. Rev. B* **2002,** 65, 064101-1-5.

24. Jorgensen, J. D.; Hu, Z.; Short, S.; Sleight, A. W.; Evans, J. S. O., Pressure-induced cubic-to-orthorhombic phase transfromation in the negative thermal expansion material HfW_2O_8. *J. Appl. Phys.* **2001,** 89, 3184-3188.

25. Varga, T.; Wilkinson, A. P.; Lind, C.; Basset, W. A.; Zha, C.-S., Pressure-induced amorphization of cubic $ZrMo_2O_8$ studied in-situ by x-ray absorption spectroscopy and diffraction. *Solid State Commun.* **2005,** 135, 739-744.

26. Varga, T.; Wilkinson, A. P.; Lind, C.; Bassett, W. A.; Zha, C.-S., High pressure synchrotron x-ray powder diffraction study of $Sc_2Mo_3O_{12}$ and $Al_2W_3O_{12}$ *J. Phys.: Condens. Matter* **2005,** 17, 4271-4283.

27. Varga, T.; Wilkinson, A. P.; Lind, C.; Bassett, W. A.; Zha, C.-S., In-situ high pressure synchrotron x-ray diffraction study of $Sc_2W_3O_{12}$ at up to 10 GPa. *Phys. Rev. B* **2005,** 71, 214106-1-8.

28. Cetinkol, M.; Wilkinson, A. P.; Lind, C., In situ high-pressure synchrotron x-ray diffraction study of $Zr_2(WO_4)(PO_4)_2$ up to 16 GPa. *Phys. Rev. B* **2009,** 79, 22.

29. Sakuntala, T.; Arora, A. K.; Sivasubramanian, V.; Rao, R.; Kalavathi, S.; Deb, S. K., Pressure-induced amorphization and decomposition in ZrV_2O_7: A Raman spectroscopic study. *Phys. Rev. B* **2007,** 75, 174119.

30. Carlson, S.; Krogh Andersen, A. M., High-pressure properties of TiP_2O_7, ZrP_2O_7 and ZrV_2O_7. *J. Appl. Cryst.* **2001,** 34, 7-12.

31. Mukherjee, G. D.; Vijaykumar, V.; Karandikar, A. S.; Godwal, B. K.; Achary, S. N.; Tyagi, A. K.; Lausi, A.; Busetto, E., Compressibility anomaly and amorphization in the anisotropic negative thermal expansion material $NbOPO_4$ under pressure. *J Solid State Chem.* **2005,** 178, 8-14.

32. Arora, A. K.; Yagi, T.; Miyajima, N.; Mary, T. A., Amorphization and decomposition of scandium molybdate at high pressure. *J. Appl. Phys.* **2005,** 97, 013508-1-8.

33. Karmakar, S.; Deb, S. K.; Tyagi, A. K.; Sharma, S. M., Pressure-induced amorphization in $Y_2(WO_4)_3$: in situ X-ray diffraction and Raman studies. *J. Solid State Chem.* **2004,** 177, 4087-4092.

34. Liu, H.; Secco, R. A.; Imanaka, N.; Adachi, G., X-ray diffraction study of pressure induced amorphization in $Lu_2(WO_4)_3$. *Solid State Commun.* **2002,** 121, 177-180.

35. Garg, N.; Murli, C.; Tyagi, A. K.; Sharma, S. M., Phase transitions in $Sc_2(WO_4)_3$ under high pressure. *Phys. Rev. B* **2005,** 72, 064106.

36. Garg, N.; Panchal, V.; Tyagi, A. K.; Sharma, S. M., Pressure-induced phase transitions in $Al_2(WO_4)_3$. *J. Solid State Chem.* **2005,** 178, 998-1002.

37. Arora, A. K.; Nithya, R.; Yagi, T.; Miyajima, N.; Mary, T. A., Two-stage amorphziation of scandium molybdate at high pressure. *Solid State Commun.* **2004,** 129, 9-13.

38. Paraguassu, W.; Maczka, M.; Souza Filho, A. G.; Freire, P. T. C.; Mendes Filho, J.; Melo, F. E. A.; Macalik, L.; Gerward, L.; Staun Olsen, J.; Waskowska, A.; Hanuza, J., Pressure-induced structural transformations in the molybdate $Sc_2(MoO_4)_3$. *Phys. Rev. B* **2004,** 69, 094111-1-5.

39. Mittal, R.; Chaplot, S. L.; Schober, H.; Mary, T. A., Origin of Negative Thermal Expansion in Cubic ZrW_2O_8 Revealed by High Pressure Inelastic Neutron Scattering. *Phys. Rev. Lett.* **2001,** 86, 4692-4695.

40. Mittal, R.; Chaplot, S. L.; Schober, H.; Mary, T. A.; Lind, C.; Wilkinson, A. P., Origin of negative thermal expansion in cubic ZrW_2O_8 and $ZrMo_2O_8$: High pressure inelastic neutron scattering study. *Solid State Phys. (India)* **2001,** 44, 656.

41. Ravindran, T. R.; Arora, A. K.; Mary, T. A., High Pressure Behavior of ZrW_2O_8: Gruneisen Parameter and Thermal Properties. *Phys. Rev. Lett.* **2000,** 84, 3879-3882.

42. Ravindran, T. R.; Arora, A. K.; Mary, T. A., High-pressure Raman spectroscopic study of zirconium tungstate. *J. Phys. Condens. Matter.* **2001,** 13, 11573-11588.

43. Yamamura, Y.; Nakajima, N.; Tsuji, T.; Koyano, M.; Iwasa, Y.; Katayama, S.; Saito, K.; Sorai, M., Low-temperature heat capacities and Raman spectra of negative thermal expansion compounds ZrW_2O_8 and HfW_2O_8. *Phys. Rev. B* **2002,** 66, 014301.

44. Bennington, S. M.; Li, J.; Harris, M. J.; Ross, K. D., Phonon softening in ice Ih. *Physica B* **1999,** 263-264, 396-399.

45. Chen, B.; Muthu, D. V. S.; Liu, Z. X.; Sleight, A. W.; Kruger, M. B., High-pressure Raman and infrared study of HfW_2O_8. *Phys. Rev. B* **2001,** 64, 214111.

46. Mittal, R.; Chaplot, S. L.; Kolesnikov, A. I.; Loong, C.-K.; Mary, T. A., Inelastic neutron scattering and lattice dynamical calculation of negative thermal expansion in HfW_2O_8. *Phys. Rev. B* **2003,** 68, 054302.

47. Holzer, H.; Dunand, D. C., Phase transformation and thermal expansion of Cu/ZrW_2O_8 metal matrix composites. *J. Mater. Res.* **1999,** 14, 780-789.

48. Yilmaz, S., Phase transformations in thermally cycled Cu/ZrW_2O_8 composites investogated by synchrotron x-ray diffraction. *J. Phys. Condens. Matter.* **2002,** 14, 365-375.

49. Hu, Z.; Jorgensen, J. D.; Teslic, S.; Short, S.; Argyriou, D. N.; Evans, J. S. O.; Sleight, A. W., Pressure-induced phase transformation in ZrW_2O_8 -

Compressibility and thermal expansion of the orthorhombic phase. *Physica B* **1998,** 241-243, 370-372.

50. Jorgensen, J. D.; Hu, Z.; Teslic, S.; Argyriou, D. N.; Short, S.; Evans, J. S. O.; Sleight, A. W., Pressure -induced cubic-to-orthorhombic phase transition in ZrW_2O_8. *Phys. Rev. B* **1999,** 59, 215-225.

51. Carlson, S.; Krogh Andersen, A. M., High-pressure transitions of trigonal α-$ZrMo_2O_8$. *Phys. Rev. B* **2000,** 61, 11209-11212.

52. Krogh Andersen, A. M.; Carlson, S., High-pressure structures of α- and δ-$ZrMo_2O_8$. *Acta Cryst. B* **2001,** 57, 20-26.

53. Lind, C.; VanDerveer, D. G.; Wilkinson, A. P.; Chen, J.; Vaughan, M. T.; Weidner, D. J., New high pressure form of the negative thermal expansion materials zirconium molybdate and hafnium molybdate. *Chem. Mater.* **2001,** 13, 487-490.

54. Secco, R. A.; Liu, H.; Imanaka, N.; Adachi, G., Pressure-induced amorphization in negative thermal expansion $Sc_2(WO_4)_3$. *Journal of Materials Science Letters* **2001,** 20, 1339-1340.

55. Achary, S. N.; Mukherjee, G. D.; Tyagi, A. K.; Vaidya, S. N., Preparation, thermal expansion, high pressure and high temperature behavior of $Al_2(WO_4)_3$. *J. Mater. Sci.* **2002,** 37, 2501-2509.

56. Mukherjee, G. D.; Vijaykumar, V.; Achary, S. N.; Tyagi, A. K.; Godwal, B. K., Phase transitions in $Al_2(WO_4)_3$: high pressure investigations of low frequency dielectric constant and crystal structure. *J. Phys.: Condens. Matter* **2004,** 16, 7321-7330.

57. Suzuki, T.; Omote, A., Negative Thermal Expansion in $(HfMg)(WO_4)_3$. *Journal of the American Ceramic Society* **2004,** 87, 1365-1367.

58. Piffard, Y.; Verbaere, A.; Kinoshita, M., Beta-$Zr_2(PO_4)_2SO_4$ - A Zirconium Phosphato-Sulfate With a $Sc_2(WO_4)_3$ Structure - A Comparison Between Garnet, NASICON, and $Sc_2(WO_4)_3$ Structure Types. *J. Solid State Chem.* **1987,** 71, 121-130.

59. Miletich, R.; Allan, D., R.; Kuhs, W., F., High-Pressure Single-Crystal Techniques. *Rev. Mineral. Geochem.* **2001,** 41, (High-Temperature and High-Pressure Crystal Chemistry), 445-519.

60. Zhdanov, G. S.; Zhuralev, N. N.; Stepanova, A. A.; Umanskii, M. M., Crystal Chemistry of the Metal Hexaborides. *Soviet Physics, Crystallography* **1957,** 2, 284-285.

61. Barnett, J. D.; Block, S.; Piermarini, G. J., An Optical Fluorescence System for Quantitative Pressure Measurement in the Diamond-Anvil Cell. *Rev. Sci. Instrum.* **1973,** 44, 1.

62. Hammersley, A. P.; Svensson, S. O.; Hanfland, M.; Fitch, A. N.; Hausermann, D., Two-dimensional detector software: From real detector to idealised image or two-theta scan. *High Press. Res.* **1996,** 14, 235-248.

63. Larson, A. C.; Von Dreele, R. B., *GSAS - General Structure Analysis System*. Report LA-UR-86-748: Los Alamos Laboratory, 1987.

64. Toby, B. H., EXPGUI, a graphical user interface for GSAS. *J. Appl. Crystallogr.* **2001,** 34, 210-213.

65. Angel, R. J. *EOS-FIT*, 5.2; Virginia Tech: Blacksburg, VA, 2001.

66. Tsvigunov, A. N.; Sirotinkin, V. P., Preparation of $Zr_2WO_4(PO_4)_2$ and indexing of its X-ray diffraction pattern. *Russ. J. Inorg. Chem.* **1990,** 35, 1740.

67. Abrahams, S. C.; Bernstein, J. L., Crystal Structure of the Transition-Metal Molybdates and Tungstates. II. Diamagnetic $Sc_2(WO_4)_3$. *J. Chem. Phys.* **1966,** 45, 2745-2752.

68. Lind, C. Negative Thermal Expansion Materials Related to Cubic Zirconium Tungstate. Ph.D. Thesis, Georgia Institute of Technology, Atlanta, GA, 2001.

69. Varga, T.; Wilkinson, A. P.; Jorgensen, J. D.; Short, S., Neutron powder diffraction study of the orthorhombic to monoclinic transition in $Sc_2W_3O_{12}$ on compression. *Solid State Sci.* **2006,** 8, 289-295.

70. Cetinkol, M. Structural and high pressure studies of some low and negative thermal expansion materials. Ph.D., Georgia Institute of Technology, United States -- Georgia, 2008.

71. Evans, J. S. O.; Mary, T. A., Structural Phase Transitions and negative thermal expansion in $Sc_2(MoO_4)_3$. *Int. J. Inorg. Mater.* **2000,** 2, 143-151.

CHAPTER 4

THE PREPARATION OF PbP_2O_7 FROM $Pb(HPO_4)_2 \cdot xH_2O$; AN *IN-SITU* DIFFRACTION STUDY

4.1 Introduction

PbP_2O_7 belongs to the AX_2O_7 family of frameworks, whose structures have been widely studied starting as early as 1935.[1] In this family of frameworks, A is usually a tetravalent cation (Si, Ti, Zr, Hf, Th, Ge, U, Pu, Ce, or Sn) in an octahedral environment, and X is a pentavalent species (P, As, or V) in a tetrahedral environment.[2-12] However, mixed III/V valent materials $M^{III}_{0.5}M^{V}_{0.5}P_2O_7$ (M^{III} = Bi, Sb, Nd, Eu, Al, Fe, Ga, In, and Y; M^{V} = Ta and Nb) are also known.[13, 14] Octahedra and tetrahedra share corners creating the framework shown in Figure 4.1(left). This structure is closely related to that of the NTE material α-ZrW_2O_8 (see Figure 4.1, right).[15]

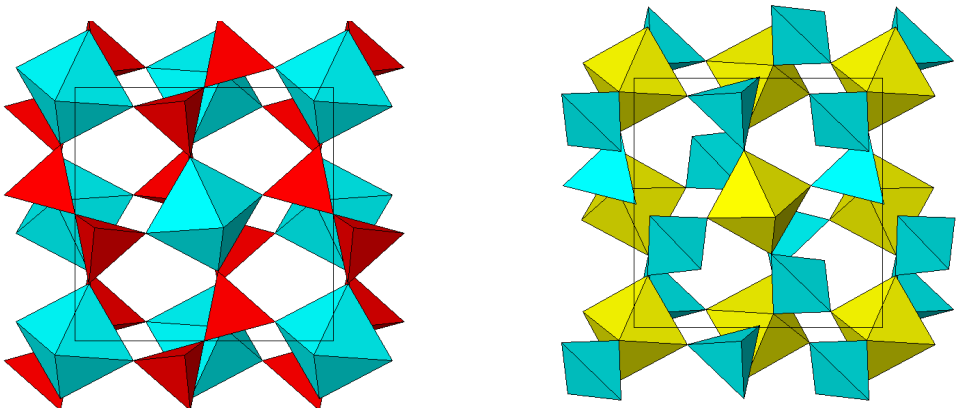

Figure 4.1. Crystal structure of AX_2O_7 (ZrP_2O_7, left) vs. α-ZrW_2O_8 (right). ZrO_6 represented by blue octahedra on left and yellow octahedra on the right. PO_4 are red tetrahedra on left, WO_4 are blue tetrahedra on right.

The thermal expansion characteristics of AX_2O_7 family members were examined as early as 1954.[16] Work on ZrP_2O_7, established that, above a phase transition at 290 ºC, the material exhibits a linear coefficient of thermal expansion (CTE) of $3.5x10^{-6}$ K^{-1}.[17, 18] Putting small M^{4+} cations into the framework to generate TiP_2O_7[19] and GeP_2O_7[12] leads to positive thermal expansion at all temperatures, but materials with larger M^{4+}, particularly, CeP_2O_7[8], UP_2O_7[20], ThP_2O_7[21], and ZrV_2O_7[22], show negative thermal expansion at some temperatures. Below in Figure 4.2 is a diagram taken from Sleight showing the thermal expansion properties of some AX_2O_7 materials.[23] PbP_2O_7 is a material of interest because while its thermal expansion properties have been explored by one of our former group members, Kathy, while nothing on the material has been published.

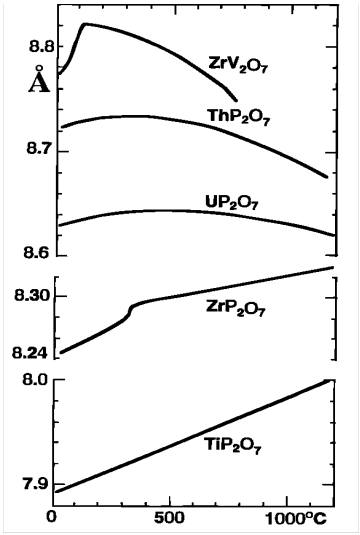

Figure 4.2. Thermal expansion trends of various members of the AX_2O_7 structural family taken from Sleight. [23]

The structure of PbP_2O_7,[24] is also of interest to us because it stands out from other member of the AX_2O_7 family with various M^{4+} cations. Figure 4.3 shows the lattice constants for various members of the AP_2O_7 family plotted versus the ionic radii of the tetravalent cations. If a trendline is drawn correlating the radius and the lattice constant of the material, Pb^{4+} falls off of this line. We also wish to understand why PbP_2O_7 does not lie on this trend line.

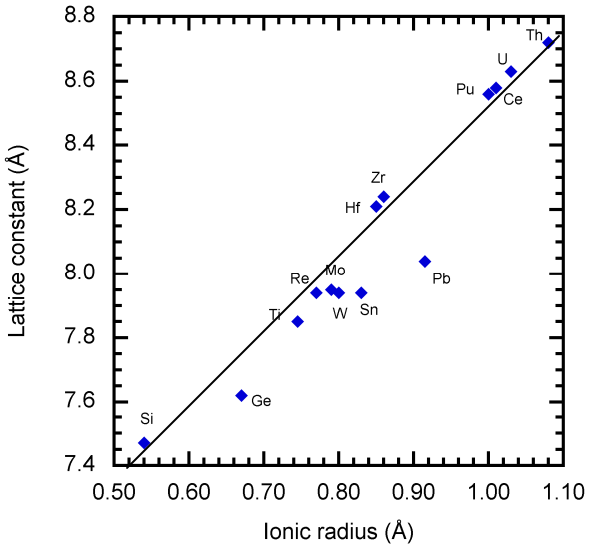

Figure 4.3. Graph of room temperature pseudo cubic lattice constants vs. ionic for AX_2O_7 family members containing various M^{4+}.

4.2 Experimental

4.2.1 Synthesis of $Pb(HPO_4)_2 \cdot H_2O$ Precursors

As part of our efforts to produce a $Pb(HPO_4)_2.xH_2O$ precursor that reliably and cleanly decomposed to give PbP_2O_7, several modifications to the previously reported synthetic procedure, for this precursor were explored.[25] Lead(IV) acetate (Strem) was recrystallized before use, while, acetic acid (VWR), phosphoric acid (Baker, Fisher), and nitric acid (Fisher) were used as purchased. The variations to the procedure included but were not limited to using new starting materials, the speed of phosphoric acid addition, reflux variation times, changes in the reaction temperature, the nitric acid addition method, the ammonium hydroxide addition method (in an attempt to control the pH), and the water addition method. With all of these variations failing to result in a reproducible procedure to produce high quality PbP_2O_7, some detailed diffraction studies of precursor

decomposition were undertaken in an effort to better understand what was limiting the formation of the desired product. This chapter focuses on a detailed examination of the precursors from three of the variations that were tried. The only difference in procedure for the first two precursors synthesized was the source starting phosphoric acid. While both batches were made using phosphoric acid from the same company, a different bottle of acid was used. However, attempts to repeat procedures even with the same chemicals could not reproduce the results.

4.2.1.1 Synthesis of Precursor Batch A; A Material That Readily Produces PbP_2O_7 on Decomposition.

In a reaction vessel fitted with a reflux condenser, 1.689 g (3.81 mmol) $Pb(OAc)_4$ (OAc = acetate) was added to 17.0 mL of hot glacial acetic acid. The solution was heated to reflux while stirring to produce a clear colorless solution. 22.0 mL of 85% H_3PO_4 (Fisher) was quickly added to the solution down the side of the flask. A milky white suspension immediately formed. Distilled water, 12.0 mL, was added to the suspension 10 min later. The suspension was allowed to reflux for 48 h. 1.5 mL of concentrated HNO_3 was then added down the side of the flask, and the suspension refluxed for an additional 44 h. It was then cooled to room temperature in air. The white product was recovered by filtration, washed with 20 mL 0.1 M HNO_3, 15 mL of distilled water, and 2 x 15 mL of acetone before finally being air dried overnight. Yield 0.894 g (2.14 mmol $Pb(HPO_4)_2 \cdot H_2O$).

4.2.1.2 Synthesis of Precursor Batch B; A Material That Shows Two Weight Losses Above 350 ºC

In a reaction vessel fitted with a reflux condenser, 1.635 g (3.69 mmol) $Pb(OAc)_4$ was added to 17.0 mL of hot glacial acetic acid. The mixture was heated to reflux while stirring, producing a clear colorless solution. 21.0 mL of 85% H_3PO_4 (Fisher) was quickly added down the side of the flask. A milky white suspension formed immediately. Distilled water, 12.0 mL, was added 5 min later. The suspension was held at reflux for 48 h. Then 1.5 mL of concentrated HNO_3 was added down the side of the flask. The mixture was allowed to reflux for an additional 44 h and then cooled back to room temperature in air. The white product was recovered by filtration, and washed with 20 mL 0.1 M HNO_3 and 20 mL distilled water. The white powder gained some brown discoloration when the water was in contact with the sample. This was followed by washing with 2 x 20 mL acetone, and finally air drying overnight leading an off-white powder. Yield 1.111 g (2.66 mmol $Pb(HPO_4)_2 \cdot H_2O$).

4.2.1.3 Synthesis of Precursor Batch C Using a Shortened Reaction Time

In a reaction vessel fitted with a reflux condenser, 1.885 g (4.25 mmol) $Pb(OAc)_4$ was added to 17.0 mL hot glacial acetic acid. The solution was heated to reflux forming a clear yellow tinted solution. The yellowish tint in the solution is due to $Pb(OAc)_4$ dissolving in acetic acid as noticed from the recrystallization of the material. As more $Pb(OAc)_4$ is dissolved in acetic acid the solution becomes more yellow. Heating was ceased and 20.0 mL 85% H_3PO_4 (Baker) was added, leading to a milky white suspension. Distilled water 12.5 mL was immediately added to the suspension. After stirring for 15

minutes, 1.5 mL of concentrated nitric acid was added down the side of the flask, followed by an additional 15 min of stirring. A white product was recovered by filtration, and then washed with 30 mL 0.1 M HNO_3, 30 mL distilled water, 2 x 15 mL acetone, and was finally air dried overnight. Yield 0.862 g (2.07 mmol $Pb(HPO_4)_2 \cdot H_2O$).

4.2.2 Synthesis of PbP_2O_7

In a predried crucible was weighed 0.490 g (1.17 mmol) of precursor batch A of $Pb(HPO_4)_2 \cdot H_2O$. The crucible was placed in an oven for 2.5 h at 310 ºC because this was a temperature where the plateau was seen on the TGA that was thought to give the desired PbP_2O_7 product. The oven was turned off and the crucible was removed from the oven and allowed to cool, leaving a solid white product. Yield 0.446 g (1.17 mmol). The weight loss of the material in this scenario is associated with the decomposition of $Pb(HPO_4)_2 \cdot H_2O$ to PbP_2O_7.

4.2.3 Laboratory Powder X-ray Diffraction

Room temperature powder X-ray diffraction measurements were performed on a Scintag diffractometer equipped with a copper tube and a Peltier cooled solid state detector. Data were collected over the range of 5-90º 2θ, at a rate of 2º/min. Additional measurements of the precursor forming the well defined PbP_2O_7 material were collected over the range of 5-140º 2θ, at a rate of 0.2º/min. Presented in Figure 4.4 is an overlay of the three diffraction patterns of the materials along with reflections corresponding to $Pb(HPO_4)_2 \cdot H_2O$.

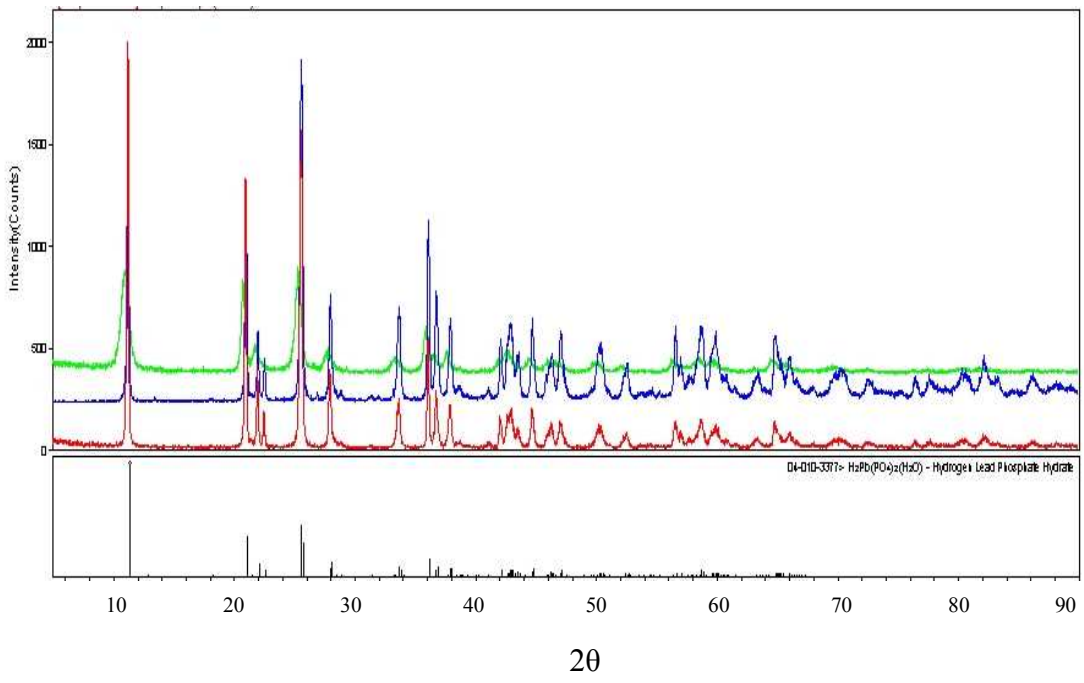

Figure 4.4. Overlay of powder x-ray diffraction patterns (top) collected for batches A (red, bottom), B (blue, center), and C (green, top), with reflections expected for $Pb(HPO_4)_2 \cdot H_2O$ (bottom).

4.2.4 Thermogravimetric Analysis of $Pb(HPO_4)_2 \cdot H_2O$

TGA measurements were performed on the $Pb(HPO_4)_2 \cdot H_2O$ precursor batches using a Perkin Elmer TGA 7 Thermogravimetric Analyzer. Data were collected from 30 to 550 ºC at 10 ºC/min using a platinum pan as a sample holder under an argon atmosphere. Care was taken to not go above 600 ºC in order to avoid the evaporation of lead compounds or the formation of platinum/lead alloys in the sample pan (See Figure 4.5).

4.2.5 *In-situ* High Temperature Diffraction Measurements

Samples of $Pb(HPO_4)_2 \cdot H_2O$ were packed into quartz capillaries and placed inside a flow furnace designed by Chupas *et. al*.[26] Diffraction data were collected at the Advanced Photon Source, Argonne National Lab, beam line 1-BM-C using x-rays with λ= 0.61832 Å. 2D images were recorded on a MAR 345 detector. Each x-ray exposure lasted 36 s, followed by time to read the data off of the image place totaling 130 s. During each exposure, the sample was rocked through a 6º range. The sample was oscillated to improve the powder average. Data were collected continuously while the sample temperature was ramped up. The samples were initially heated to 50 ºC, and then the temperature was ramped at a rate of 3 ºC/min up to 600 ºC, at which point, the heating program was stopped. The reported temperature for each diffraction pattern is the average temperature of the sample when the shutter opened and when the shutter closed. The image plate data were integrated with FIT-2D.[27]

4.2.6 SEM Measurements

The surface morphology of the three batches of $Pb(HPO_4)_2 \cdot H_2O$ were investigated by scanning electron microscopy, using a Hitachi 800 scanning electron microscope (SEM) equipped with a Kevex energy dispersive X-ray detector. Samples were coated with a thin gold layer prior to use in the instrument.

4.3 Results

4.3.1 Synthesis of $Pb(HPO_4)_2 \cdot xH_2O$

For each of the precursor preparations described in the previous section a white or off-white product was recovered via filtration. During filtration, batch A remained a white powder, while, in batches B and C, a brown discoloration was noticed while washing the product with water. This slight color change suggests the presence of PbO or PbO_2, as these are reddish brown and brown respectively. Upon washing the product with acetone, however, these materials lost their discoloration returning to an off-white product, suggesting a reaction between the material and acetone. Laboratory x-ray powder diffraction of these materials shows all three batches to be $Pb(HPO_4)_2 \cdot H_2O$ by comparison to the ICDD database.

4.3.2 Thermogravimetric Analysis of $Pb(HPO_4)_2 \cdot xH_2O$ Batches

The TGA of all three batches of material were recorded under identical conditions and are displayed in Figure 4.5. While laboratory x-ray diffraction suggests that all of the samples contain $Pb(HPO_4)_2 \cdot xH_2O$, the TGA results show very different behavior for each batch. TGA of every individual batch synthesized led to a curve similar to the three discussed in this chapter.

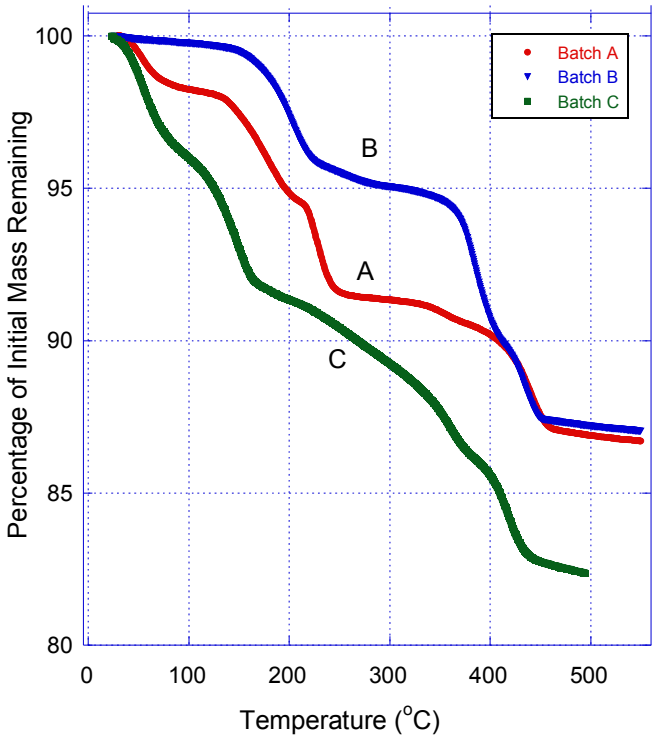

Figure 4.5. TGA curves of the three distinct batches of $Pb(HPO_4)_2 \cdot xH_2O$ produced from various alterations in experimental procedure. Batch A producing quality PbP_2O_7 is seen in red, with batch B with two weight losses after 350ºC in blue, and batch C from the shortened reaction time in green. Each sample was heated at a rate of 10ºC/min under an argon atmosphere.

Batch A exhibits a series of weight losses over the temperature range 30 to 550 ºC as seen in Figure 4.6. The first weight loss occurs from 50 to 90 ºC and is equivalent to a 1.51% weight loss from the starting sample. Since this sample was reacted, filtered, and stored in an open atmosphere it can only be assumed that the weight loss corresponds to either absorbed water and the material is losing 0.32 moles of water per mole of sample or amorphous impurity that cannot be identified. The second weight loss in batch A occurs from 150 to 200 ºC and the percentage remaining of the starting material goes from 97.45% to 94.84%. Assuming that we have a hydrated materials with water incorporated into the structure of the material, we assume that the material is again

experiencing a water loss. The weight loss corresponds to 0.79 moles of water per mole of sample. The next weight loss occurs from 210 to 250 ºC taking the mass of sample remaining from 94.58% to 91.59%. Assuming that the sample is now undergoing further decomposition this loss is presumed to be from the dehydroxylation of $Pb(HPO_4)_2$ to PbP_2O_7 recombining the hydrogen phosphate group into a pyrophosphate group. This loss can then be calculated to be 0.75 mol of water lost per mole of sample. The next weight loss appears as a shoulder on the TGA curve and occurs from 350 to 370 ºC. This weight loss takes the percentage remaining of the starting material down from 90.96% to 90.64%. If we assume that all of the remaining HPO_4 of the material is not decomposed, this additional weight loss corresponds to dehydroxylation and a calculated water weight loss of 0.12 mol of water per mole of sample. However, if we were to assume that the material undergoes complete dehydroxylation, we would overall have 1.00 mol of water loss and suggests that the starting material may not be pure $Pb(HPO_4)_2 \cdot H_2O$. The final weight loss of this material occurs from 420 to 470 ºC taking the weight percentage of the original starting material from 89.61% to 87.05%. At this stage, if we assume all hydrogen atoms have left the sample in the form of water and we have purely PbP_2O_7 the next decomposition would most logically be oxygen loss. Thus from the calculated weight loss it is estimated that this weight loss corresponds to 0.41 mol of O_2 being lost per mole of sample forming PbP_2O_6. Again if this were pure starting material this weight loss would be 0.50 mol of O_2 per mole of sample. With the weight losses of this material being off both the dehyroxylation and the oxygen loss step, it is a possibility that ~20% of this material is an impurity or another phase of material with hydroxyl groups within its structure.

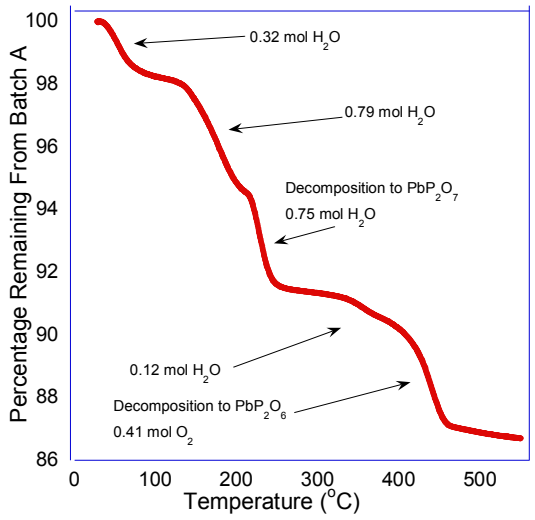

Figure 4.6. TGA curve of batch A of $Pb(HPO_4)_2 \cdot H_2O$ taken from 30 to 550 ºC under an argon atmosphere. The sample was heated at 10 ºC/min.

The TGA weight loss curve for batch B is displayed in Figure 4.7. Four distinct weight losses are visible on the curve with the first occurring from 160 to 220 ºC and corresponding to 3.22% as the percentage of original mass goes from 99.29 to 96.07%. If we assume that the starting material is $Pb(HPO_4)_2 \cdot H_2O$, at this temperature range we would dehydrate the sample to $Pb(HPO_4)_2$. Calculations suggest that this material is losing 0.89 moles of water per mole of sample. The next weight loss is displayed as a shoulder in the range 250 to 280 ºC, with a weight loss of 0.35%. If we assume that the sample is beginning to undergo decomposition from $Pb(HPO_4)_2$ to PbP_2O_7 and we have dehydroxylation, or the material still hasn't fully lost water from the hydrated material, this weight loss can be accounted for with 0.14 moles of water per mole of sample material. The third weight loss occurs from 360 to 410 ºC taking the mass percentage

from 94.42% to 90.06%. At this step, we can assume that $Pb(HPO_4)_2$ is completely anhydrous and is experiencing a weight loss from dehydroxylation. This weight loss is calculated to come from 1.02 moles of water from the dehydroxylation step per mole of sample. The final weight loss in the sample occurs from 410 to 460 ºC, taking the mass percentage of the starting material from 90.06% to 87.38%. If we assume all dehydroxylation is completed at this point and we have no hydrogen remaining in the sample, presumably, oxygen loss would occur. The final weight loss can be explained with 0.35 mole O_2 lost per mole of sample. While this value is slightly low for the expected 0.50 mole O_2, part of this weight loss maybe included in the previous weight loss seeing as there is no clear plateau in the diagram and oxygen loss may occur at a lower temperature. It could also indicate that the starting material is not purely $Pb(HPO_4)_2 \cdot H_2O$ and may contain ~20% impurities or other lead containing phase.

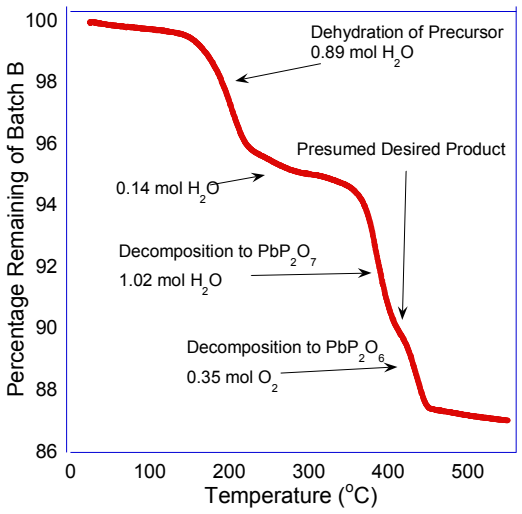

Figure 4.7. TGA weight loss curve of precursor batch B of $Pb(HPO_4)_2 \cdot xH_2O$. The sample was heated at a rate of 10 ºC/min under an argon atmosphere.

The TGA curve for batch C is displayed in Figure 4.8 and has a series of distinct weight losses from 30 to 500 ºC. The first weight loss in the material occurs from 50 to 90 ºC and takes the mass percentage of the original weight from 98.70% to 96.29%. Since our material was stored in an open atmosphere it is assumed that this weight loss comes from extra absorbed water. Calculations of this weight loss suggest that 0.90 moles of water are being lost per mole of sample. The next weight loss in the sample occurs from 110 to 160 ºC and is presumed to be associated with the dehydration of the starting material to give $Pb(HPO_4)_2$. The percentage of the initial sample weight goes from 95.68% to 92.19% and assuming that the starting material is $Pb(HPO_4)_2 \cdot H_2O$ this weight loss corresponds to 1.01 mole of water per mole of sample. From 200 to 385 ºC the TGA curve doesn't plateau and shows continuous weight loss over the entire temperature range. The percentage of the initial mass goes from 91.34% to 86.11%. If we assume the sample had not fully undergone dehydration and also experienced dehydroxylation to form PbP_2O_7 from $Pb(HPO_4)_2$ this weight loss has been calculated to be equivalent to 1.35 moles of water per mole of sample. The final weight loss in this material occurs from 385 to 450 ºC, bringing the percentage of the original sample mass from 86.11% to 82.75%. If we assume no hydrogen remains in the sample and we have PbP_2O_7 the most logical weight loss would result from loss of oxygen. From the original starting material, calculations result in a loss of 0.49 moles of O_2 per mole of sample producing PbP_2O_6.

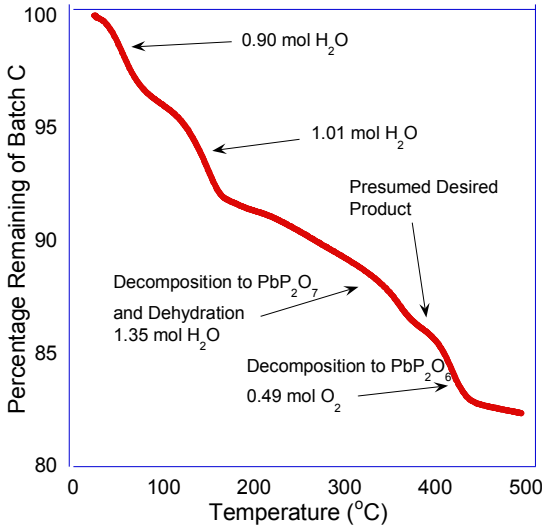

Figure 4.8. TGA of $Pb(HPO_4)_2 \cdot xH_2O$ precursor batch C taken from 30-500 ºC. The sample was heated at a rate of 10 ºC/min under an argon atmosphere.

4.3.3 *In-situ* Diffraction Measurements

Each precursor batch was examined using, *in-situ*, variable temperature, x-ray diffraction. Each sample was heated to 600 ºC at 3 ºC/min under flowing air. The x-ray powder diffraction patterns collected for batch A are presented as a 2D contour plot in Figure 4.9. Reflections from $Pb(HPO_4)_2 \cdot H_2O$ are visible from 45 ºC up to a maximum of 190 ºC. A comparison with ICDD pattern #04-010-3377 suggests that there are no crystalline impurities. On heating to 160 ºC, new reflections become visible at 4.68, 6.06, 8.17, 9.48, 12.39, 14.20, 14.99, 16.43, 16.73, 17.10, 19.10, 21.80, 22.30, and 24.74º 2θ. The reflections for $Pb(HPO_4)_2 \cdot H_2O$ slowly disappear and are no longer detectable by 198ºC. The new reflections did not match any material in the ICDD database. However, the largest intensity d-spacings were close to those reported for the related material α-$Zr(HPO_4)_2$,[28] which is expected to be structurally related to $Pb(HPO_4)_2$. So it was assumed that the new phase forming at above 160 ºC was anhydrous $Pb(HPO_4)_2$.

Anhydrous $Pb(HPO_4)_2$ is obtainable in this batch from 198 to 233 ºC with no detection of other materials. At 233 ºC new reflections become visible at 7.64, 8.83, 14.66, 15.23, 17.76, 19.31, 19.72, 21.70, and 23.08º 2θ. When the new reflections are compared to those of known compounds listed in the ICDD database, it is obvious that the material has started to dehydroxylate to form PbP_2O_7. $Pb(HPO_4)_2$ and PbP_2O_7 coexist, with $Pb(HPO_4)_2$ as the predominant phase until the temperature is ~378 ºC, at which point PbP_2O_7 becomes the majority phase. At 403 ºC, there appears to be a shift in position for the reflections at ~4.68 and ~9.48º 2θ to 5.10 and 9.65º 2θ respectively. The shifted peaks do not correspond to those of any known phase. However, the new phase is presumed to be a structural relative of $Pb(HPO_4)_2$. Increasing the temperature further to 478 ºC allows for $Pb(HPO_4)_2$ reflections to completely disappear. Additionally, many new reflections appear. By 500 ºC reflections corresponding to PbP_2O_7 are barely noticeable. Comparison of the new reflections with materials in the ICDD database reveals that the material has decomposed further to PbP_2O_6[29] with no obvious impurities. The reflections remain unchanged until the end of the experiment at 600 ºC.

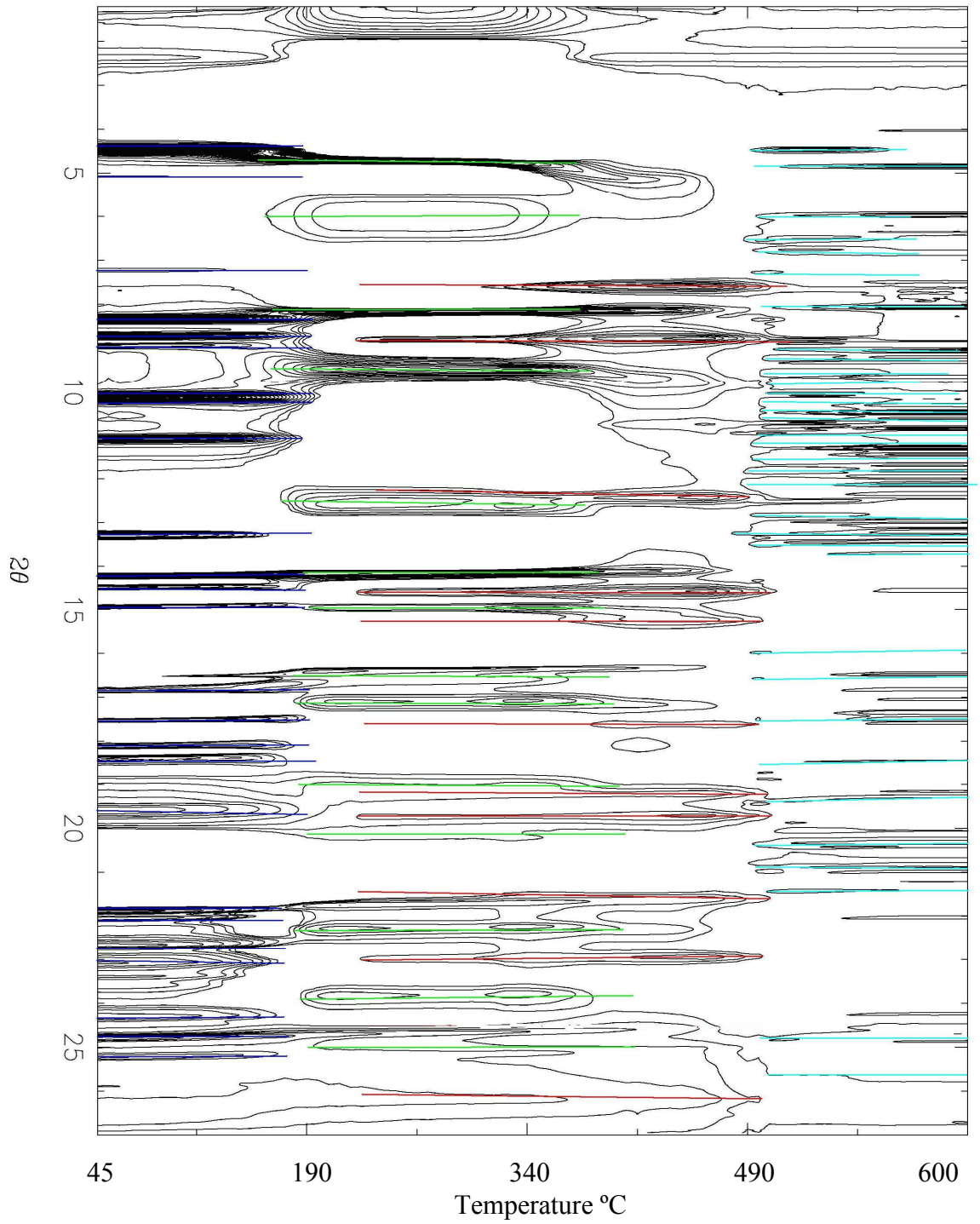

Figure 4.9. A 2D contour plot of the diffraction data acquired during the *in-situ* x-ray experiment on batch A of $Pb(HPO_4)_2{\cdot}H_2O$ precursor. The sample was heated at 3 ºC/min inside a tube furnace under flowing air. Reflections for $Pb(HPO_4)_2{\cdot}xH_2O$ are marked in dark blue, with $Pb(HPO_4)_2$ in green, PbP_2O_7 in red and PbP_2O_6 in light blue.

Figure 4.10 shows a contour plot of the diffraction data acquired while precursor batch B was heated. The first pattern was recorded at 55 ºC. Comparison of the reflections to the materials in the ICDD database, reveals that the initial sample is pure $Pb(HPO_4)_2 \cdot H_2O$ (marked in dark blue). The reflection at 2.68º 2θ is not from the sample and may be due to the beam stop on the diffractometer at the synchrotron.

As the sample is heated, new reflections begin to appear at 4.68, 8.17, 9.46, 12.55, 14.23, 14.95, 16.43, 16.73, 17.12, 17.52, 22.36 and 24.76º 2θ at 136 ºC and are predominant at 190 ºC, with little to no remaining peaks from $Pb(HPO_4)_2 \cdot H_2O$ at this temperature. While these peaks (marked in green) cannot be identified through the ICDD database, comparison of the largest intensity d-spacing show that the material is related to α-$Zr(HPO_4)_2$[28] suggesting that the material has undergone a dehydration to form crystalline α-$Pb(HPO_4)_2$. Unlike batch A, the material shows no signs of decomposition or new material forming until 325 ºC. These peaks become more distinct on the contour plot at ~340 ºC. At this temperature, reflections begin to appear at 7.61, 8.80, 14.60, 19.30, 19.76, 21.70, and 22.99º 2θ. Compared to the ICDD database, these reflections correspond to the material PbP_2O_7 (marked in red) suggesting that $Pb(HPO_4)_2$ decomposes to this material by dehydroxylation. PbP_2O_7 doesn't become a dominant phase in this precursor batch as seen with batch A and as the temperature is increased to 402 ºC peaks corresponding to the phase PbP_2O_6[29] (marked in yellow) form showing oxygen loss within the sample. At this temperature other reflections are present at 9.33, 11.33, 11.93, 12.92, 13.57, 14.36, 15.98, 17.62, 18.70, 19.36, 19.80, 21.58, and 23.35º. Comparison with the ICDD database suggests these reflections may correspond to contamination of the final PbP_2O_6 product with PbO_2 (PDF# 98-000-0386, marked in

light blue). However, due to the many reflections observed for PbP_2O_6, some peaks do overlap with those expected for PbO_2. Additionally, the presence of PbO_2 correlates with the observance of a brownish product during filtration and further suggests contamination is highly likely in batch B of $Pb(HPO_4)_2 \cdot xH_2O$. Previous literature has reported that PbO_2 is thermally stable up to 257 ºC and decomposes to $Pb_{12}O_{17}$ up to 459 ºC before decomposing to PbO at 521 ºC.[30] If our sample decomposes to PbO_2 at some point it would be stable in this temperature range and reflections would be visible. Reflections of the other materials may not be visible if they are decomposition products of this minor impurity and may be a fraction of a percent of the impurity. Reflections for the product PbP_2O_6 are observed up until the final temperature of 600 ºC.

At ~382 ºC, it appears that the reflections for $Pb(HPO_4)_2$ at 4.68, 9.46, and 12.45º 2θ disappear and form a broad series of weak reflections characteristic of PbP_2O_6 suggesting that the material doesn't have to go through the PbP_2O_7 intermediate before fully decomposing. If $Pb(HPO_4)_2$ decomposes directly into PbP_2O_6, this will lead to less of the desired PbP_2O_7 product and may hinder exploration as to the synthesis of this material.

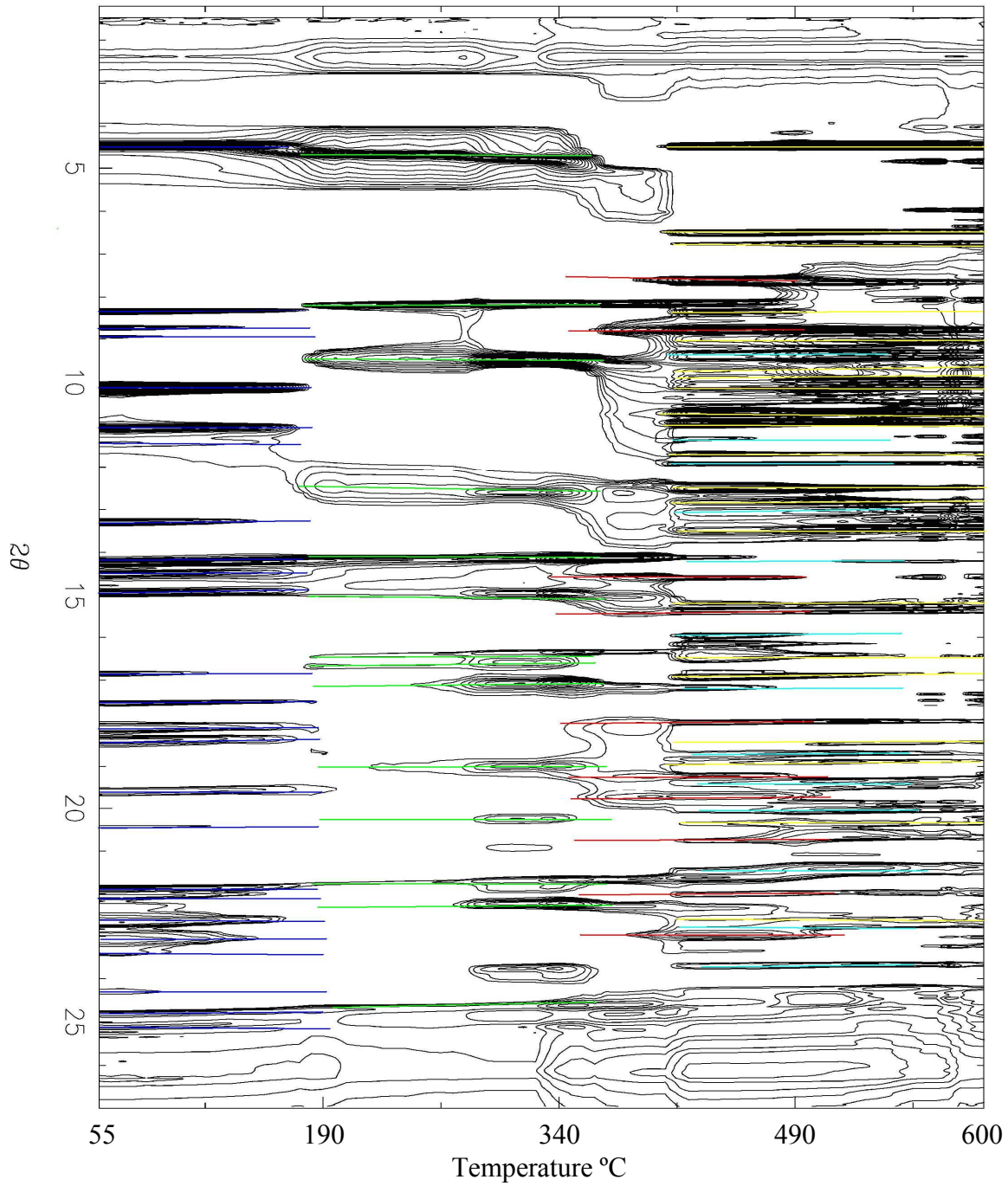

Figure 4.10. A 2D contour plot of the diffraction data acquired during *in-situ* x-ray experiment on batch B of precursor $Pb(HPO_4)\cdot xH_2O$. The sample was heated at 3 ºC/min inside a tube furnace under flowing air. Reflections observed for $Pb(HPO_4)_2\cdot H_2O$ are in dark blue, $Pb(HPO_4)_2$ in green, PbP_2O_7 in red, PbP_2O_6 in yellow. The impurity PbO_2 is observed in light blue.

Figure 4.11 shows the x-ray diffraction data collected for precursor batch C, during the *in-situ* measurements. The first diffraction data set was collected at a temperature of 50 ºC. The x-ray reflections of the initial material were compared to those of materials in the ICDD database. The starting material was $Pb(HPO_4)_2 \cdot H_2O$ (marked in dark blue), with no clear evidence of impurities within the sample. There was a severe amount of fluctuation in the background of the one dimensional patterns, and the peaks were more broad than in precursor batches A and B.

As the sample was heated, the appearance of additional reflections was noticed as the temperature reached 107 ºC. They were dominant by 137 ºC. The new reflections occurred at 4.68, 8.20, 9.48, 12.55, 14.30, 15.05, 16.47, 17.16, 19.10, 20.32, 21.87, 22.40, 23.91, and 24.80º 2θ. They were ascribed anhydrous $Pb(HPO_4)_2$ (marked in green) as explained in the section on precursors A and B.

While heating the material, peak intensities of the material gradually become weaker and when the temperature reaches 340 ºC, additional peaks arise from the baseline of the diffraction pattern. These reflections occur at 7.64, 8.80, 14.63, 15.28, 17.71, 19.29, 19.72, 20.77, and 21.67º 2θ. As the temperature reaches 411 ºC these reflections become much more noticeable. When these reflections are compared to what is expected for various materials in the ICDD database, the peak reflections correspond to PbP_2O_7 (marked in red). Looking closer at this temperature, additional reflections were measured in the data set at 5.91, 6.23, 9.92, 10.56, 11.68, 12.29, 12.53, 14.01, 14.55, 15.28, 18.21, and 19.87º 2θ. Comparing these reflections with the materials in the ICDD database, suggests that this material is contaminated possibly with PbO (marked in yellow). At 429

ºC during the experiment the synchrotron beam was refilled and these reflections become much more apparent due to the increase in intensity. PbP_2O_7, however, never becomes a dominant phase in this material, however, its peaks are more apparent than that of precursor batch B.

Finally, as the material is continually heated to 600 ºC a whole series of reflections correlating to PbP_2O_6 (marked in light blue) are observed indicating that the material has decomposed from $Pb(HPO_4)_2$ and PbP_2O_7. The additional increase in beam current helped distinguish PbP_2O_6 clearly with all of its reflections.

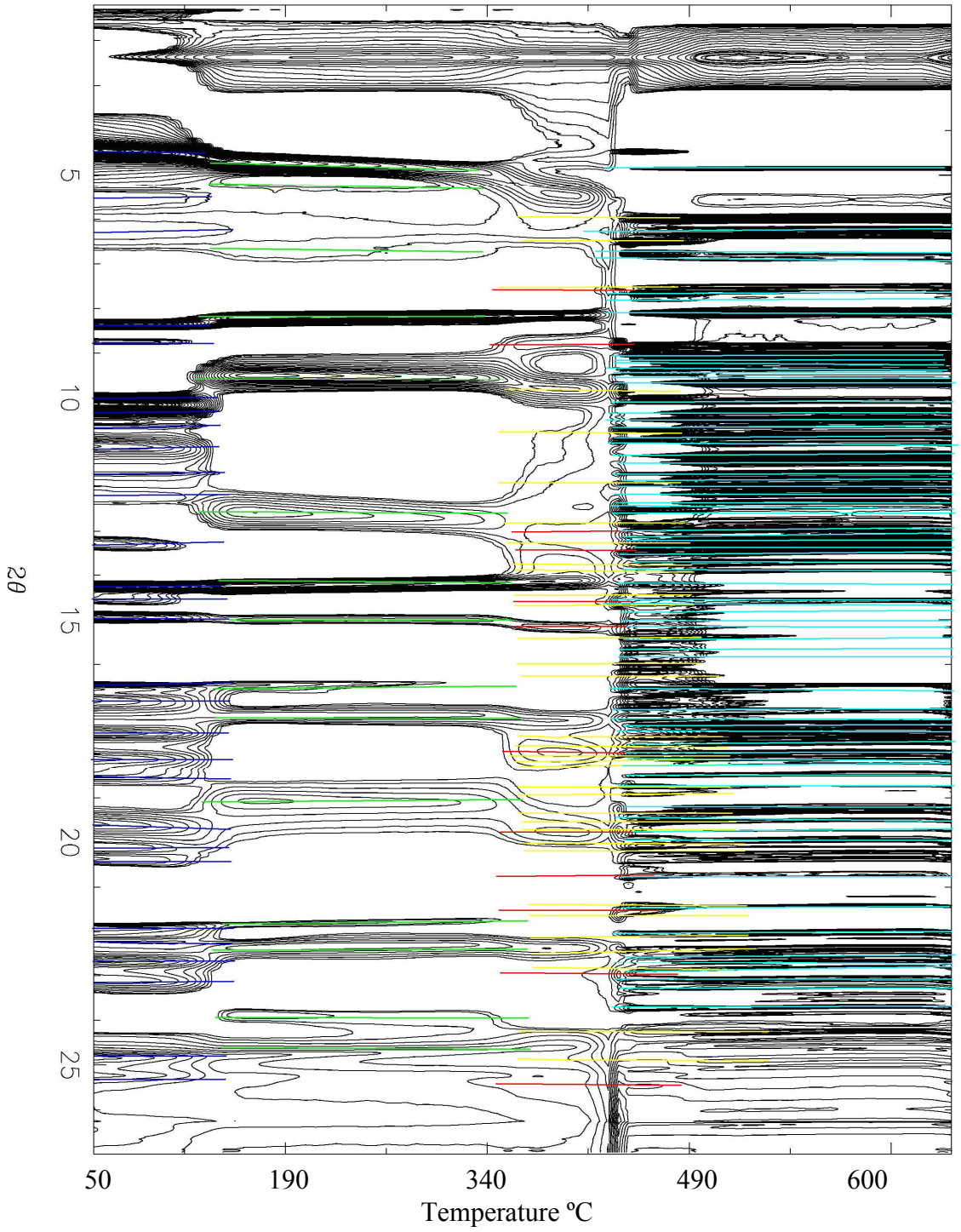

Figure 4.11. A 2D diagram of the powder x-ray diffraction patterns collected during a variable temperature experiment on batch C of precursor $Pb(HPO_4)_2 \cdot xH_2O$. The sample was heated to 600 ºC at a rate of 3 ºC/min under air flow in a furnace. Reflections of $Pb(HPO_4)_2 \cdot H_2O$ are marked in dark blue, $Pb(HPO_4)_2$ in green, PbP_2O_7 in red, PbP_2O_6 in light blue. Reflections from the impurity PbO are marked in yellow.

4.3.4 SEM Measurements

Samples for the SEM measurement were prepared by taking a small spatula tip of the precursor batch and adding it to a vial with acetone. The material was dispersed onto carbon tape and coated with a gold layer for conduction.

Examination of the SEM images for precursor batch A (see Figure 4.12) reveals that the white product is grouped together in clusters ranging from ~40 to ~200 μm per side. As the magnification of the clusters is increased, it can be seen that the surface is very textured with many raised surfaces and appears to be somewhat porous in character.

In comparison, in the images for precursor batch B (see Figure 4.13), it can be seen that the material appears to be less well defined. In some of the more well defined areas the larger clusters range from ~40 to ~150 μm on a side, while a majority of the material appears to be under 5 μm on a side and dispersed throughout the sample. At higher magnification, it is apparent that the material is much smoother than that of precursor batch A. At 7,000 times magnification precursor batch B appears to be even more porous than batch A making the material very different and may explain as to why they behave so different on TGA.

The images for precursor batch C can be observed in Figure 4.14. In the preparation of this sample, after the acetone had dried, it appeared as no crystals were detected on the carbon tape. The sample was then dispersed two more times on the carbon tape drying each time in an open atmosphere. Examination of the material at low magnification reveals that the shortened reaction time makes the material clump together and not form clusters of the material suggesting the material is comprised of extremely small crystals or the precursor batch is amorphous. At higher magnification the material appears as

though it has been layered in this lightly textured sheets. Precursor batch C, however, does appear to be smoother in surface than batches A and B, while less porous than both of the other batches. This difference in surface may allow further exploration into how it affects the dehydration of the starting material into a suitable product of PbP_2O_7.

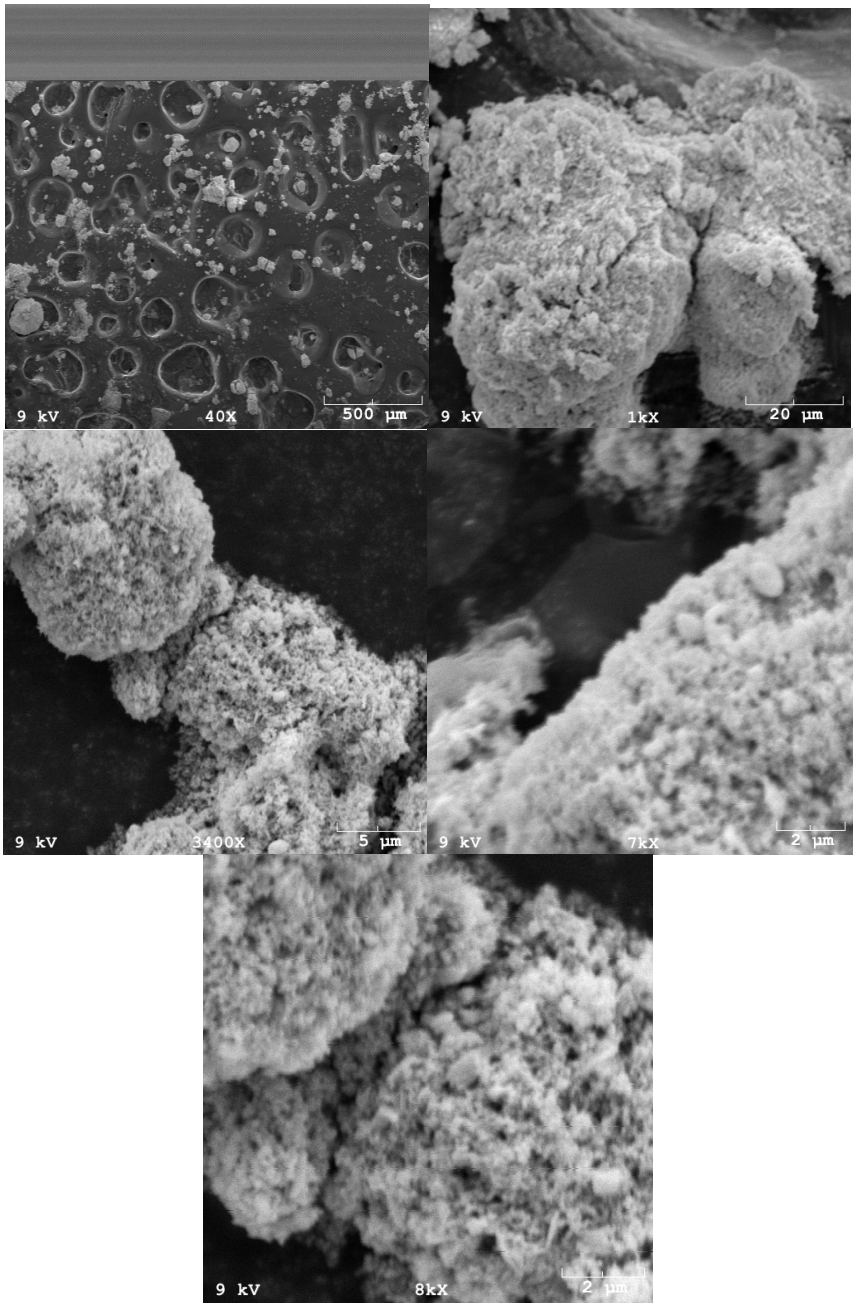

Figure 4.3.12 SEM images magnified by 40X (top left) to 8,000X (bottom center) for batch A leading to high quality PbP_2O_7.

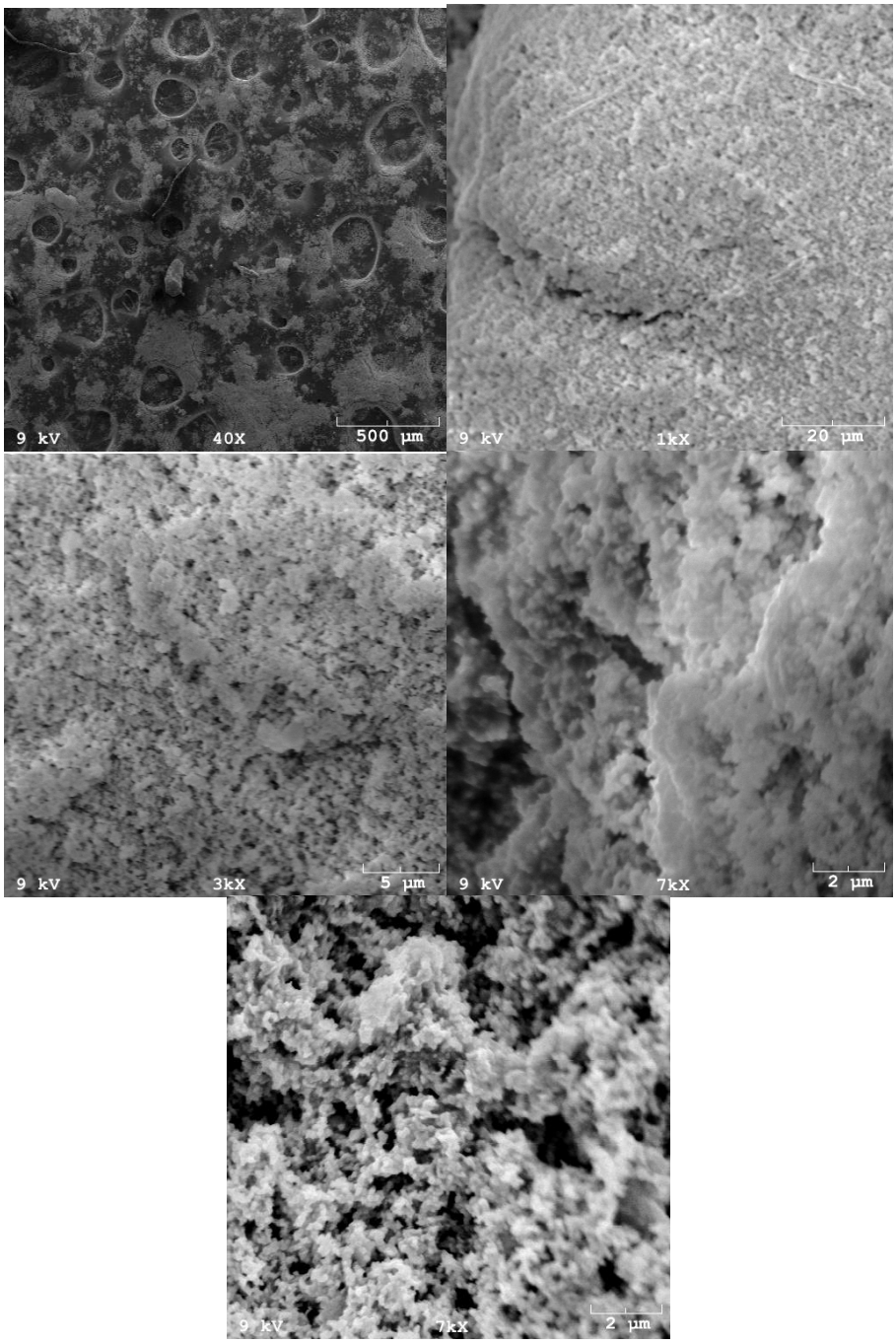

Figure 4.13. SEM images recorded for $Pb(HPO_4)_2 \cdot xH_2O$ batch B from 40X (top left) to 7,000X (bottom center).

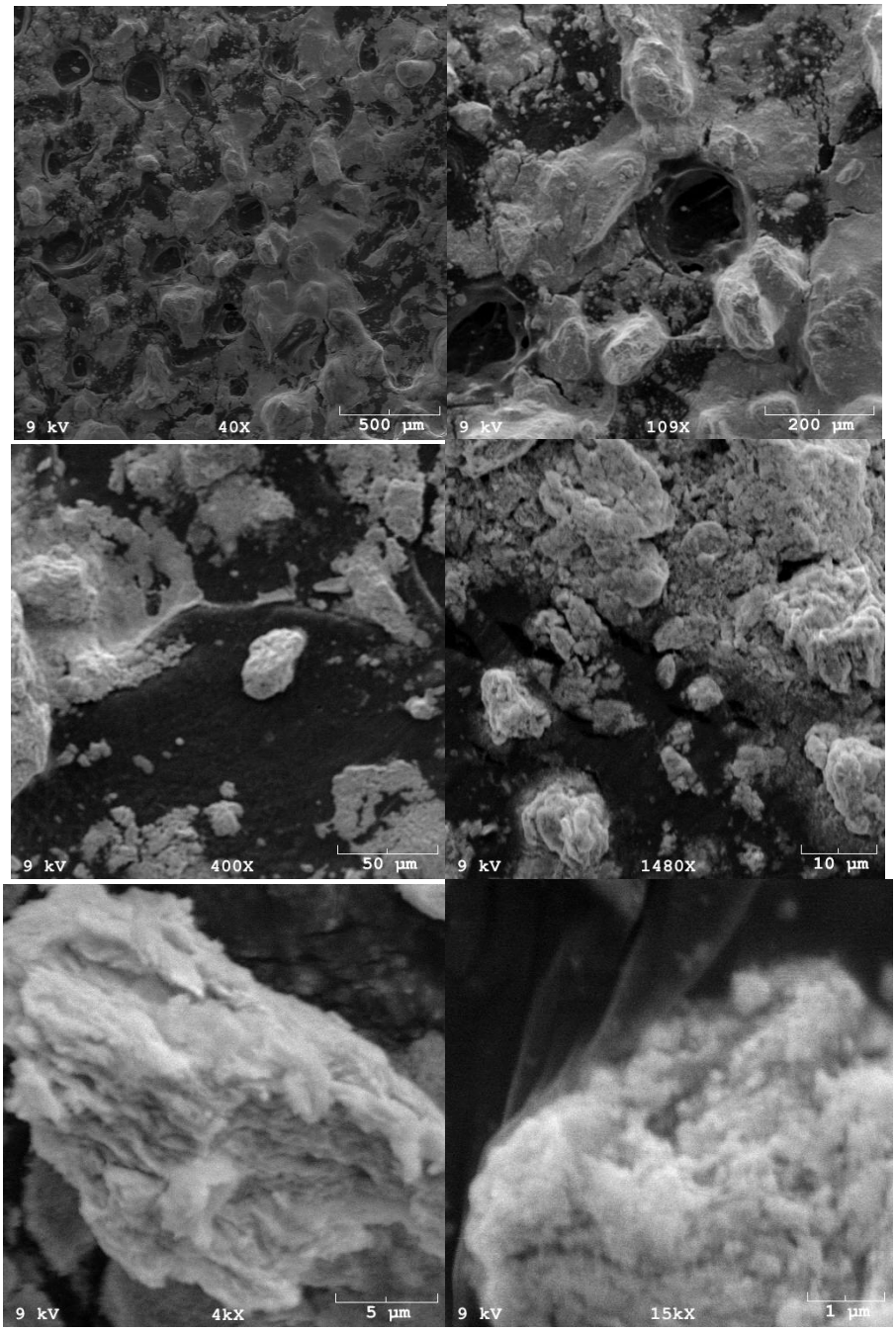

Figure 4.14. SEM images of $Pb(HPO_4)_2 \cdot xH_2O$ batch C, with increasing magnifications from 40X (top left) to 15,000X (bottom right).

4.3.5 PbP_2O_7 Laboratory Powder X-ray Diffraction Measurements

The powder x-ray diffraction pattern collected on the heated sample of precursor batch A is shown below in Figure 4.15.

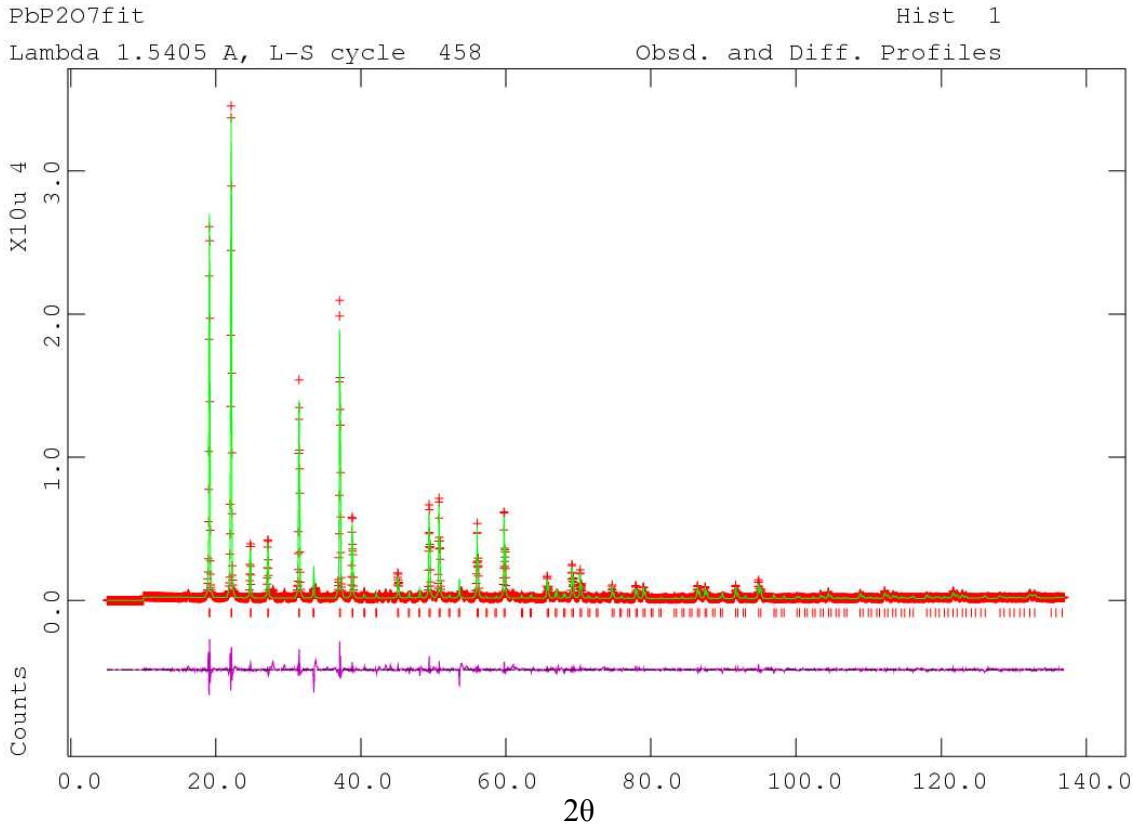

Figure 4.15. X-ray diffraction pattern collected for precursor batch A heated at 310 ºC for 2.5 h (red), compared to a Le Bail fit for PbP_2O_7 in space group *Pa-3* (green). Reflections expected for PbP_2O_7 are marked below and the difference curve is shown in purple.

The reflections at ~19.12, 22.20, 24.76, 27.16, 31.46, 33.74, 37.08, 38.78, 45.10, 49.40, 50.77, 53.82, 56.02, 59.74, 65.67, 67.02, 69.10, 70.22, 74.64, 77.88, 78.96, 86.40, 91.67, and 94.82º 2θ correspond to reflections to PbP_2O_7 as compared to the ICDD database

#00-002-1081. The diffraction pattern for PbP_2O_7 is not pure and several impurities can be suggested within the material. Minor reflections at approximately 28.85, 33.50, 47.98, 56.95, 59.82, 70.26, and 77.71º 2θ suggest that this product contains PbO_2.[29] Reflections at approximately 15.62, 26.68, 29.44, 35.34, 40.46, and 46.54 suggest that this material also has contamination from $PbO{\cdot}xH_2O$, PDF# 00-022-0665. There are many other reflections visible in the pattern that cannot be identified, so while we can say that the majority of the product is PbP_2O_7 the product definitely contains up to approximately 20% of impurities based on TGA measurements making it difficult to take accurate measurements on the material. A much cleaner product has to be generated.

Data when compared to a Le Bail fit for pure PbP_2O_7 in space group *Pa-3* did not give a very good fit due to the large number of peaks from impurities as seen in Figure 4.16. While heating sample batch A at 310 ºC did lead to a large amount of the most desired product, the impurities prevent reasonable measurements to be collected on the sample.

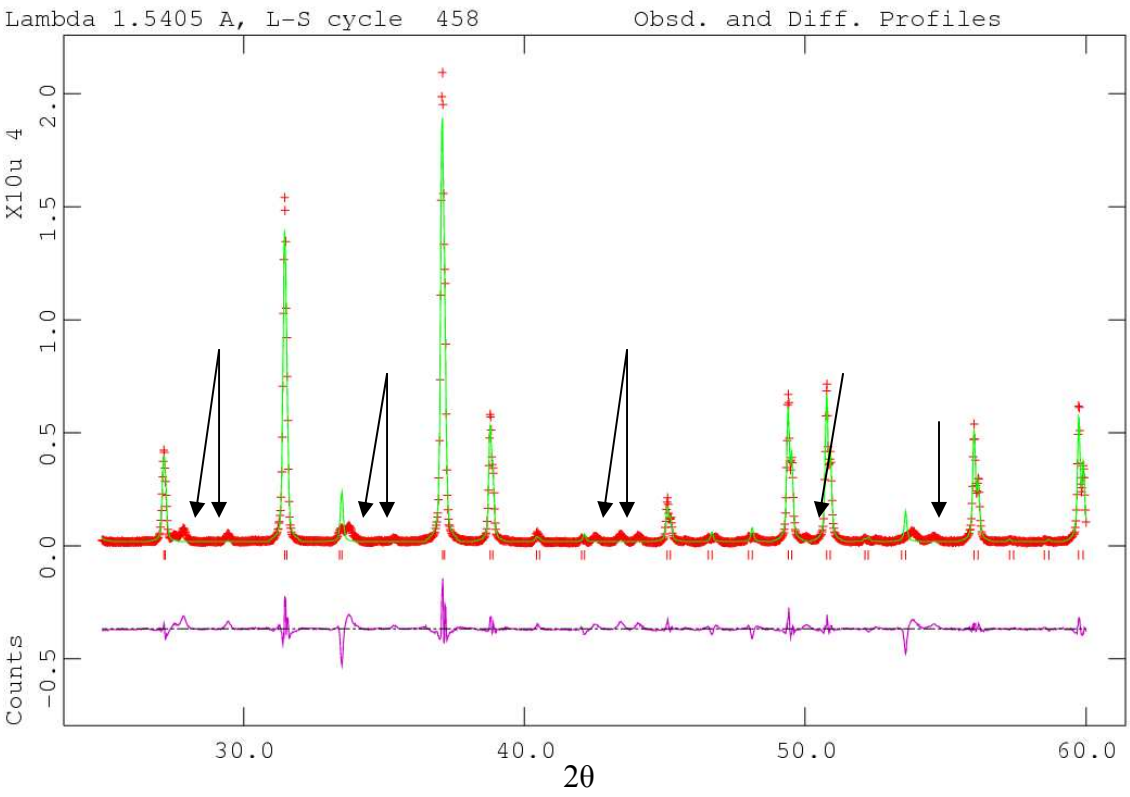

Figure 4.16. X-ray diffraction pattern (red) collected from 25 to 60º 2θ for precursor batch A heated at 310 ºC for 2.5 h. The pattern is compared to a Le Bail fit for PbP_2O_7 (green) with the difference cruve shown in purple. Black arrows mark the presence of impurities in the sample.

4.4 Discussion

4.4.1 Synthesis of $Pb(HPO_4)_2 \cdot xH_2O$ Precursors

While the overall synthesis of the precursor material should be straightforward, one of the biggest questions that we have come across that still remains unanswered is why do different products form using essentially the same reaction conditions. Of the many batches of the $Pb(HPO_4)_2 \cdot xH_2O$ that we have synthesized, only two have been good precursors to form PbP_2O_7, with one of those being lost in a laboratory accident. The syntheses of batches A and B were carried out at the same time using different bottles of

phosphoric acid leading us initially to believe that the ascribed differences were due to the different bottles of H_3PO_4. However, after repetition of the experiment, two products were generated both similar to batch B, leading to almost no PbP_2O_7 upon heating of the precursor. The strangeness of the reaction not repeating is even further complicated when the phosphoric acid containers are examined. Examination of the bottles confirms that as bought, both starting bottles of phosphoric acid were from the same company and same lot number suggesting that the starting material should be chemically equivalent and should produce identical products. Thus, there is something happening during the reaction of these starting materials that is causing the precursor "$Pb(HPO_4)_2 \cdot H_2O$" to behave differently in each case.

In the synthesis of batch C the reaction time for the material was shortened from four days to 30 minutes adding the nitric acid halfway between. From our results in the material with the shortened reaction time, the final product was found to contain some impurities of $PbO \cdot xH_2O$ in the material. The addition of nitric acid usually allows for the oxidation of PbO, however, since it is present in the final product after heating it is possible that nitric acid didn't have time to oxidize all of the lead(II) in the product to lead(IV).

Additionally, it was found that when batches of the material were left at reflux for a week instead of four days that all of the material in the reaction vessel was converted to a lead(II) phosphate material. Thus from this generalization, the overall reaction time is a significant influence on obtaining a desirable product for dehydration to PbP_2O_7.

4.4.2 Decomposition of Precursor Batches

4.4.2.1 Precursor Batch A

The TGA curve for batch A exhibits an initial weight loss from 50 to 90 ºC accounting for a 1.51% weight loss from the original mass of the sample. As mentioned in the results this weight loss is likely the result from loss of absorbed water collected due to the material being stored in an open atmosphere. However, the weight loss could also be a result from decomposition of an impurity in the sample. Comparing this result to the *in-situ* powder diffraction patterns collected at the same temperature, we can clearly see that the lattice constants are not significantly affected until 160 ºC, indicating that this weight loss in the TGA curve does in fact correspond to dehydration of the material. It is also suggested that the 0.32 mol of water per mole of sample being removed is not incorporated into the crystal structure and is loosely attached to the material.

Further inspection of the TGA curve for batch A significantly shows a weight loss in material from 150 to 210 ºC. This information correlates with the diminishing peak intensity of the reflections expected for $Pb(HPO_4)_2 \cdot H_2O$. By the time 210 ºC is reached in the *in-situ* powder x-ray diffraction patterns have produced new reflections. While these reflections did not correspond to any material within the ICDD database, the largest peak intensities were taken into account and were in good comparison with the peak intensities for α-$Zr(HPO_4)_2$.[28] Due to the structures of α-$Zr(HPO_4)_2 \cdot H_2O$[28] and α-$Pb(HPO_4)_2 \cdot H_2O$ were similar it is a relatively good assumption that the reflections in the *in-situ* diffraction patterns correspond to anhydrous $Pb(HPO_4)_2$. This suggests that this batch of material is losing water molecules within the framework of the crystal structure which also would dramatically effect the lattice constants of the material. The calculated loss of 0.79 mol of

water per mole of sample during the weight loss suggests even further that the material is not being dehydrated throughout the material all at the same time and is a gradual step in the material.

In precursor batch A, the next weight loss accounts for 0.75 moles of water being lost from 210 to 260 ºC, then leveling off into a new stable material. This loss corresponds to the *in-situ* pattern where PbP_2O_7 peaks become visible at roughly 225 ºC. However, as the temperature is increased further and the plateau on the TGA curve suggests that we have a stable product formation, the *in-situ* patterns suggest that $Pb(HPO_4)_2$ and PbP_2O_7 coexist for much of the same time. If this material were to be heated in the temperature range at this plateau for a longer period of time, it would be possible to generate a large quantity of PbP_2O_7 with some impurities. However, it still cannot explain as to why the material only loses 0.75 mol of water per mole of sample over at this weight loss. If the material led to a pure PbP_2O_7 phase, 1.00 moles of water would be completely removed during the dehydroxylation of $Pb(HPO_4)_2$. This 25% error suggests that the material contains some other lead containing phase.

Examination of the unidentified peaks generated at ~400 ºC suggests that $Pb(HPO_4)_2$ decomposes into a secondary product possibly containing some hydroxyl groups that is a structure relative of anhydrous $Pb(HPO_4)_2$. When these unidentified peaks disappear in the x-ray data, the only reflections that can be accounted for are from PbP_2O_6. This suggests that the unknown lead materials are decomposing to PbP_2O_6 or are another decomposition product that is being completely removed from the system. The other possibility is that this product is so minor in the material that decomposition to another material produces so little that the reflections cannot be seen with the data.

Additionally, the weight loss on the TGA curve between 350 and 370 ºC which we attribute to the possibility that the material is completing dehydroxylation needs to further be explored. The weight loss accounting for 0.12 moles of water per sample is in agreement with the temperature of the weight losses of the other batches, it could very well be a loss from unknown material as well. In coordination with the *in-situ* patterns, this is roughly the same temperature where the new peaks of an unidentified material begin to form. So this weight loss may be associated with the unknown material or the completion of dehydroxylation.

The final weight loss in the TGA for batch A occurs between 420 and 470 ºC. However, this data doesn't correlate with the *in-situ* diffraction pattern where the final material isn't being formed until ~500 ºC. Significantly it shows that the PbP_2O_7, $Pb(HPO_4)_2$, and the other unknown lead material, actually begin decomposition at an earlier temperature, but the overall materials take longer to decompose than indicated by the TGA of precursor. If the material was purely PbP_2O_7 decomposing to strictly PbP_2O_6 there should theoretically be a 0.50 mol O_2 loss in this decomposition phase. The fact that this decomposition of material has only a calculated loss of 0.41 mol O_2 suggests that ~18% of the material decomposing is not PbP_2O_7. This error is a relatively good agreement with the other weight losses observed in this system suggesting that even our best batch of sample contains up to 20% of an impurity and does not allow for clean decomposition of the precursor to PbP_2O_7.

4.4.2.2 Precursor Batch B

The first weight loss in the decomposition of precursor batch B is observed between 160 and 210 ºC and correlates with the loss of 0.89 mol of water per mole of starting sample. This weight loss in the sample material correlates with the *in-situ* data collected at the synchrotron. In the *in-situ* x-ray diffraction pattern at ~190 ºC, the peaks for $Pb(HPO_4)_2 \cdot H_2O$ begin to disappear and reflections for anhydrous $Pb(HPO_4)_2$ become apparent. This confirms that the first weight loss in the material is from the hydrate within the crystal structure. The removal of water significantly changes the lattice constants of the material producing a different pattern.

The second weight loss observed in the shoulder of the TGA between 250 and 280 ºC doesn't correlate very well with any significant change in the *in-situ* diffraction patterns. In this temperature range the peaks for $Pb(HPO_4)_2$ in the material do become more concentrated and are the only peaks observed in the diffraction pattern which may allow us to think that there are no impurities in the product. This weight loss, however, in comparison to that of precursor batch A is in the same position as the decomposition to PbP_2O_7. While this weight loss accounts for a 0.14 mol of water per mole of sample. This weight loss suggests two possibilities in the final material. The first possibility is that this weight loss is just the rest of decomposition of the hydrate to form anhydrous $Pb(HPO_4)_2$. This possibility seems highly unlikely due to the fact that most materials lose their hydrates before 200 ºC. The second possibility, and the more likely one, is that a very small percentage of the material is readily decomposing to PbP_2O_7 while a majority of the product remains $Pb(HPO_4)_2$. The weight loss of 0.14 moles of water per mol of sample

would suggest ~15% of the material is forming PbP_2O_7 which may not be visible on the x-ray diffraction pattern at that temperature.

Coordinating this information with the images taken on the SEM, the formation of the larger clusters leads to a higher quality product of PbP_2O_7 while the smaller more dispersed material (majority) decomposes at higher temperature and gives the undesired product.

The next significant weight loss observed in precursor batch B occurs in the TGA from 360 to 410 ºC and corresponds in the *in-situ* temperature experiment with the formation of peaks belonging to PbP_2O_7 in a diminished quality. The largest problem with this observance is the fact that there is such a small window as to where the desired product can actually be found that if this sample were to be heated right in the middle of this weight loss and the one following immediately, there is no telling if the entire sample will not start to decompose. The lack of a significant plateau in the TGA curve tells us that the material is very unstable with the heating and could most likely decompose as quickly as the product can be formed.

As this weight loss corresponds to the loss of 1.02 mol of water per sample and would suggest that if the starting material was pure $Pb(HPO_4)_2 \cdot H_2O$ this would be the step for complete dehydroxylation of the sample to pure PbP_2O_7. However, examining the *in-situ* x-ray diffraction patterns closely, this temperature range also contains reflections from the impurity PbO_2. As stated earlier PbO_2 is stable up to 257 ºC then begins decomposition to $Pb_{12}O_{17}$ up to 459 ºC.[30] In this situation if PbO_2 is experiencing decomposition as well, the weight loss observed between 360 and 410 ºC would be a combination of water loss from dehydroxylation and oxygen loss from the reduction of

the lead impurity. It can be suggested that the starting material upon dehydration could have as much as 20% impurity from another phase that remains undetected or can be mixed in with the background during x-ray analysis. Also it goes to show, that any sample batch containing impurity from PbO_2 will have difficulty in generating a clean batch of starting material that will lead to pure PbP_2O_7.

The final weight loss observed in the TGA between 410 and 460 ºC is decomposition to PbP_2O_6. This is confirmed by the *in-situ* x-ray diffraction patterns above 420 ºC. The weight loss in the TGA, however, only reflects a loss of 0.35 mol of oxygen per mol of sample. Under perfect conditions for a sample of pure $Pb(HPO_4)_2{\cdot}H_2O$, 0.50 mol of O_2 would be released. The erroneously low amount can be explained by 1) the formation of an unknown lead product similar to that seen in batch A at 340 ºC with the same peak positions, and 2) the possibility of PbO_2 impurity in the sample losing O_2 at an earlier phase and limiting the amount lost from PbP_2O_7.

Overall, the TGA curve of this material is very similar to that reported by Brúque *et. al.*[25] with the two weight losses and dissimilar for that of $Ce(HPO_4)_2{\cdot}H_2O$.[8] This leads to the question that remains unanswered as to what conditions in the reaction need to be generated to be able to make a clean sample with a TGA curve similar to that of $Ce(HPO_4)_2{\cdot}H_2O$ and does the contamination of the final product by PbO_2 or some other impurity cause the material to not display this TGA curve.

4.4.2.3 Precursor Batch C

In the decomposition of precursor batch C, while the starting material was classified as $Pb(HPO_4)_2{\cdot}H_2O$, it should be additionally noted that in both the laboratory x-ray

diffraction patterns and the *in-situ* powder diffraction patterns, the reflections are broader and suggesting that this precursor is more disordered than batches A and B. The SEM images of the material suggest that this material does not have very well developed crystals and is very dispersed as compared to the other batches. This suggests that as the reaction is occurring, the addition of phosphoric acid to the lead acetate in acetic acid first forms an amorphous product that slowly becomes more crystalline. Thus the more crystalline material results from reflux or just the time of the experiment and introduces a kinetics factor that must be explored further into this material.

Overall, the TGA pattern and the *in-situ* diffraction patterns correlate very well with each other. The first weight loss in the TGA is observed from 50 to 90 ºC, while peaks corresponding to $Pb(HPO_4)_2 \cdot H_2O$ remain unchanged in the *in-situ* diffraction patterns. This lack of change in the crystal structure confirms that this weight loss is due to absorbed water in the material that is easily removed with heating giving what appears to be pure $Pb(HPO_4)_2 \cdot H_2O$.

The next weight loss observed from 110 to 160 ºC correlates with the *in-situ* patterns in the formation of anhydrous $Pb(HPO_4)_2$ confirming that the structure is now losing water molecules that are strongly attached to the crystal structure. Under the reaction conditions of this experiment it suggests that the desired lead(IV) product is formed immediately and is the predominant material in the suspension.

The almost continuous weight loss from 200 to 385 ºC is associated with a weakening of the intensity of peaks for $Pb(HPO_4)_2$ in the *in-situ* diffraction patterns, and an appearance of peaks for PbP_2O_7. The weight loss in the TGA curve corresponds to 1.35 moles of water loss per mole of sample. This weight loss is a grossly unrealistic

overestimate if this starting material were initially pure $Pb(HPO_4)_2 \cdot H_2O$. The overestimate can be explained if the precursor batch contains a large amount of amorphous material with hydrogen phosphate groups, hydroxyl group, or other impurities that are decomposing over this temperature range. While we cannot fully explain as to where this excess of water is coming from, we do know it is present in the sample and may be from the amorphous material. Additionally, considering that this weight loss does not plateau at any point, there may be multiple decompositions from a variety of amorphous materials in the sample.

As the temperature is increased further, at ~429 ºC reflections indicating the presence of $PbO \cdot xH_2O$ appear. The presence of $PbO \cdot xH_2O$ is probably a consequence of the limited reaction time and lack of reflux within the material. Nitric acid addition to the reaction is supposed to eliminate PbO, which reduces the remaining material to lead(II), and with no heat and only 15 min of stirring with nitric acid, it was very much a likely possibility that this material is still present.

The final weight loss observed between 385 and 450 ºC on the TGA correlates very nicely with the *in-situ* powder x-ray diffraction patterns with all the peaks visible for PbP_2O_6. The weight loss at this point on the TGA supposedly correlates with 0.49 mol of O_2 which would be extremely good if the starting material was pure $Pb(HPO_4)_2 \cdot H_2O$. However, with all of the amorphous product suggested earlier, we cannot clearly say that this weight loss is solely from the PbP_2O_7 in the sample. However, with the peaks visible for PbP_2O_6 and no other sign of impurities other than $PbO \cdot xH_2O$, we can only assume that a majority of the original product is small crystals of $Pb(HPO_4)_2$.

4.5 Conclusions

$Pb(HPO_4)_2 \cdot H_2O$ has been found to be a very interesting material. In many attempts to derive a desired PbP_2O_7 product, we have found that repeating essentially the same procedure generates a variety of different products even though x-ray diffraction suggests otherwise. The difference in the products, is readily observable through TGA and the decomposition of the starting materials. In each of our batches, the material first undergoes water loss from dehydration to form $Pb(HPO_4)_2$, followed by a dehydroxylation step to form PbP_2O_7. All of the batches then experience oxygen loss at ~400 ºC and decompose to PbP_2O_6. The largest difference in the batches, is the temperature where dehydroxylation occurs varying from ~250 ºC for batch A to ~350 ºC as seen in batch B. The large difference in temperature for the dehydroxylation of the material leads to one material being a better precursor for PbP_2O_7 than the other, having a longer period of stabilization, before completely decomposing.

Additionally, precursor batch C was able to be generated through a shortened reaction time. From the shortened reaction time, we have learned that the material begins as an amorphous lead phosphate material that crystallizes through time to become the product that is observed in either batches A or B. TGA of this precursor batch suggests that this material doesn't go through clean decomposition and that the material has a large amount of impurities, mostly amorphous, in the sample.

In-situ, variable temperature x-ray diffraction confirms the steps of decomposition suggested by the TGA measurements. It also shows that the decomposition of each sample is not clean and there are additional materials present such as $PbO \cdot xH_2O$, PbO_2, and some other unknown lead compounds structurally related to $Pb(HPO_4)_2$. It is still

unknown if the impurities present in the sample lead to the differences in the TGA curves. With regards to the production of PbP_2O_7, *in-situ* diffraction shows that each sample produces PbP_2O_7 and that the material slowly decomposes above ~400 ºC, however, the PbP_2O_7 is present longer in batch A than in the other batches suggesting that extensive heating of this sample should produce high quality PbP_2O_7.

In our attempt to synthesize PbP_2O_7, we were able to get a decent but not great fit for the material with Rietveld modeling. Examination of the x-ray diffraction pattern showed too many impurity peaks to do thermal expansion measurements. Additionally, work still needs to be performed to generate a reproducible procedure to obtain the precursor that we desire. Of the variables we have tested we can conclude that the time of reaction is of significant importance since excessive reaction causes the material to reduce to a lead(II) compound. Additionally, the material does need to reflux to generate more quality crystals and remove the amorphous impurities from the sample. We have concluded that the order of addition is important as well, because otherwise a significant amount of PbO_2 is formed in the material that cannot be removed. Finally water addition is essential in the formation of the desired product, because otherwise when nitric acid is added, the lead(IV) reduces to lead(II) and gives an undesirable product.

4.6 References

1. Levi, G. R.; Peyronel, G., Struttura Cristallografica del Gruppo Isomorfo (Si^{4+}, Ti^{4+},Zr^{4+},Sn^{4+},Hf^{4+})P_2O_7. *Z. Kristallogr.* **1935,** 92, 190-209.

2. Bjorklund, C. W., The Preparation of PuP_2O_7 and $PuPO_4$. *J. Am. Chem. Soc.* **1958,** 79, 6347-6350.

3. Hagman, L.-O.; Kierkegaard, P., Note on the Structures of $M^{IV}P_2O_7$ (M^{IV} = Ge, Zr, and U). *Acta Chem. Scand.* **1969,** 23, 327-328.

4. Liebau, V. F.; Bissert, G.; Koppen, N., Synthese und kristallographische Eigenschaften einiger Phasen im System SiO_2-P_2O_5. *Z. Anorg. Alleg. Chem.* **1968,** 359, 113-134.

5. Huang, C.-H.; Knop, O.; Othen, D. A., Pyrophosphates of Tetravalent Elements and a Mossbauer Study of SnP_2O_7. *Can. J. Chem.* **1975,** 53, 79-91.

6. Vollenkle, H.; Wittmann, A.; Nowotny, H., Uber Diphosphate vom Typ Me(IV)P_2O_7. *Monatsh. Chem.* **1963,** 94, 956-963.

7. Burdese, A.; Lucco Borlera, M., Sul sistema tra i pirofosfati di uranio e torio. *Ann. Chim. (Rome)* **1963,** 53, 333-343.

8. White, K. M.; Lee, P. L.; Chupas, P. J.; Chapman, K. W.; Payzant, E. A.; Jupe, A. C.; Bassett, W. A.; Zha, C. S.; Wilkinson, A. P., Synthesis, Symmetry, and Physical Properties of Cerium Pyrophosphate. *Chem. Mater.* **2008,** 20, 3728-3734.

9. Evans, J. S. O.; Hanson, J. C.; Sleight, A. W., Room-Temperature Superstructure of ZrV_2O_7. *Acta Cryst.* **1998,** B54, 705-713.

10. Baran, E. J., The unit cell of hafnium divanadate. *J. Less Common Met.* **1976,** 46, 343-345.

11. Onken, H., Uber Zirkonpyroarsenat. *Naturwissenschaften* **1965,** 52, 344.

12. Losilla, E. R.; Cabeza, A.; Bruque, S.; Aranda, M. A. G.; Sanz, J.; Iglesias, J. E.; Alonso, J. A., Syntheses, Structures, and Thermal Expansion of Germanium Pyrophosphates. *J. Solid State Chem.* **2001,** 156, 213-219.

13. Oyetola, S.; Verbaere, A.; Guyomard, D.; Crosnier, M. P.; Piffard, Y.; Tournoux, M., New ZrP_2O_7-like diphosphates of either mixed ($M^{III}_{0.5}M'^{V}_{0.5}$) cations (

M=Sb,Bi,Ho,Eu; M'=Sb,Nb,Ta) or M'^{V} cations (M'=Ta, Nb): synthesis and structure. *Eur. J. Solid State Inorg. Chem.* **1991,** 28, 23-36.

14. Varga, T.; Wilkinson, A. P.; Haluska, M.; Payzant, E. A., Preparation and thermal expansion of $(M^{III}_{0.5}M'^{V}_{0.5})P_2O_7$ with the ZrP_2O_7 structure. *J. Solid State Chem.* **2005,** 178, 3541-3546.

15. Evans, J. S. O.; Mary, T. A.; Vogt, T.; Subramanian, M. A.; Sleight, A. W., Negative Thermal Expansion in ZrW_2O_8 and HfW_2O_8. *Chem. Mater.* **1996,** 8, 2809-2823.

16. Harrison, D. E.; McKinstry, H. A.; Hummel, F. A., High-Temperature Zirconium Phosphates. *J. Am. Ceram. Soc.* **1954,** 37, 277-280.

17. Khosrovani, N.; Korthuis, V.; Sleight, A. W.; Vogt, T., Unusual 180^{o} P-O-P Bond Angles in ZrP_2O_7. *Inorg. Chem.* **1996,** 35, 485-489.

18. Roy, R.; Agrawal, D. K.; McKinstry, H. A., Very Low Thermal Expansion Coefficient Materials. *Annu. Rev. Mater. Sci.* **1989,** 19, 59-81.

19. Taylor, D., Thermal Expansion Data: XIII Complex Oxides with chain, ring and layer structures and apatites. *Br. Ceram. Trans. J.* **1988,** 87, 88-95.

20. Kirchner, H. P.; Merz, K. M.; Brown, W. R., Thermal Expansion of Uranium Pyrophosphate and Ceramic Bodies in the System UO_2-P_2O_7. *J. Am. Ceram. Soc.* **1963,** 46, 137-141.

21. Laud, K.; Hummel, F. A., The system ThO_2-P_2O_5. *J. Am. Ceram. Soc.* **1971,** 54, 296-298.

22. Craig, D. F.; Hummel, F. A., Zirconium Pyrovanadate Transitions. *J. Am. Ceram. Soc.* **1972,** 55, 532.

23. Sleight, A. W., Compounds that Contract on Heating. *Inorg. Chem.* **1998,** 37, 2854-2860.

24. Peyronel, G., The existence, properties and crystalline structure of $Pb^{IV}P_2O_7$. *Gazz. Chim. Ital.* **1939,** 69, 254-262.

25. Bruque, S.; Aranda, M. A. G.; Losilla, E. R.; Olivera-Pastor, P.; Maireles-Torres, P., Synthesis Optimization and Crystal Structures of Layered Metal(IV) Hydrogen Phosphates, .alpha.-$M(HPO_4)_2 \cdot .H_2O$ (M = Ti, Sn, Pb). *Inorg. Chem.* **1995,** 34, 893-899.

26. Chupas, P. J.; Chapman, K. W.; Kurtz, C.; Hanson, J. C.; Lee, P. L.; Grey, C. P., A versatile sample-environment cell for non-ambient X-ray scattering experiments. *J. Appl. Crystallogr.* **2008,** 41, 822-824.

27. Hammersley, A. P.; Svensson, S. O.; Hanfland, M.; Fitch, A. N.; Hausermann, D., Two-dimensional detector software: From real detector to idealised image or two-theta scan. *High Press. Res.* **1996,** 14, 235-248.

28. Chernorukov, N. G.; Korshunov, I. A.; Zhuk, M. I., Polymorphic Transitions in Acidic Titanium, Zirconium, and Hafnium Phosphates. *Zhurnal Neorganicheskoi Khimii* **1977,** 22, 2065-2069.

29. Olbertz, A.; Stachel, D.; Svoboda, I.; Fuess, H., Redetermination of the crystal structure of lead catena-polyphosphate, $[Pb_2(PO_3)_4]$(infinity). *Zeitschrift Fur Kristallographie-New Crystal Structures* **1998,** 213, 239-240.

30. Alamlhoda, A. A.; Sajadi, S. A. A.; Hashemian, S. J., Study of thermal behavior of alpha-PbO2, using TG and DSC. *J. Therm. Anal.* **2008,** 92, 917-920.

CHAPTER 5

IN-SITU LOCAL STRUCTURE STUDIES OF CUBIC $ZrMo_2O_8$ AS A FUNCTION OF PRESSURE AND TEMPERATURE

5.1 Introduction

There has recently been much scientific interest in materials exhibiting negative thermal expansion.[1-12] A large amount of work has been directed toward the AM_2O_8 (A= Zr and Hf; M = W or Mo) family of frameworks.[1-3, 8, 10, 13-23] Members of this family have been studied since the discovery of ZrW_2O_8 in 1959.[24] Their frameworks are constructed from corner sharing AO_6 octahedra and MO_4 tetrahedra. While all of the oxygen atoms in the AO_6 octahedra bridge to MO_4 tetrahedra, only three of the oxygen atoms in the tetrahedra are bridging, leaving a terminal oxygen on each tetrahedron.

Previous studies have shown that cubic ZrW_2O_8 exhibits negative thermal expansion up to its decomposition into ZrO_2 and WO_3 at 1050 K.[25] From 0.3 to 430 K, cubic ZrW_2O_8 exists in space group $P2_13$ (Figure 5.1).[1] Below 430 K, ZrW_2O_8 has a linear CTE of ~ -8.8×10^{-6} K^{-1}.[1]

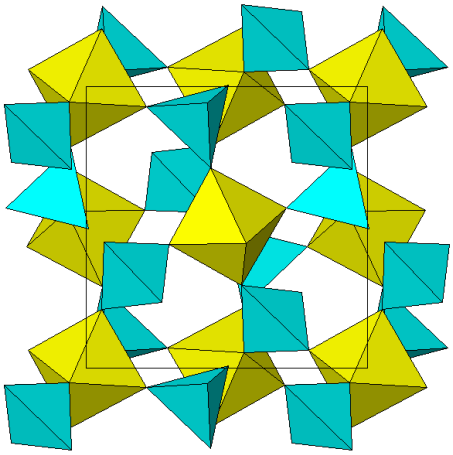

Figure 5.1. Crystal structure of α-ZrW_2O_8. ZrO_6 octahedra are shown in yellow, WO_4 tetrahedra are shown in turquoise.

As the temperature is increased, ZrW_2O_8 undergoes a crystalline to crystalline phase transition from space group $P2_13$ to $Pa\text{-}3$ at ~430 K. After the phase transition, the CTE changes from ~ -8.8 x 10^{-6} K^{-1} to ~ -4.9 x 10^{-6} K^{-1}.[1] The increase in symmetry results from a rearrangement of the WO_4 tetrahedra and a loss of order within the crystal structure. The disorder associated with the phase transition in ZrW_2O_8 is illustrated in Figure 5.2.[14] Below the phase transition temperature, the WO_4 tetrahedra are ordered and pairs of tetrahedra point in a well defined direction as depicted by the dark solid lines. Above the phase transition temperature, each pair of WO_4 tetrahedra can face in the original direction (W_{1A} and W_{2A}), or in the opposite direction (W_{1B} and W_{2B}) represented by the thin solid line.

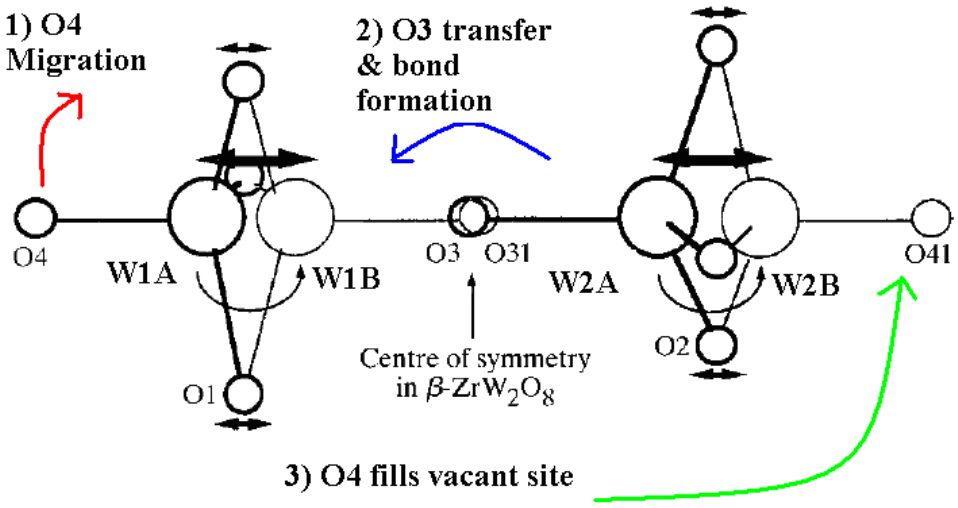

Figure 5.2.[14] The order-disorder phase transition adapted from Evans *et.al.* as α-ZrW_2O_8 becomes β-ZrW_2O_8 at 430 K. Disorder rearrangement occurs by O4 migration (red), followed by O3 transfer from W2 to W1 (blue) then oxygen filling the vacant site (green).

Unit cells of α-ZrW_2O_8 and β-ZrW_2O_8 each have four formula units in the framework of the cell. Figure 5.3 shows the arrangement of the four pair of WO_4 tetrahedra in the ordered α-ZrW_2O_8 structure. Each of the pairs of tetrahedra lies along a three-fold axis of symmetry. The orientation of the pairs of tetrahedra becomes random on a long length scale. It is not known if there is still any short range ordering associated with the orientations of neighboring pairs of tetrahedra.

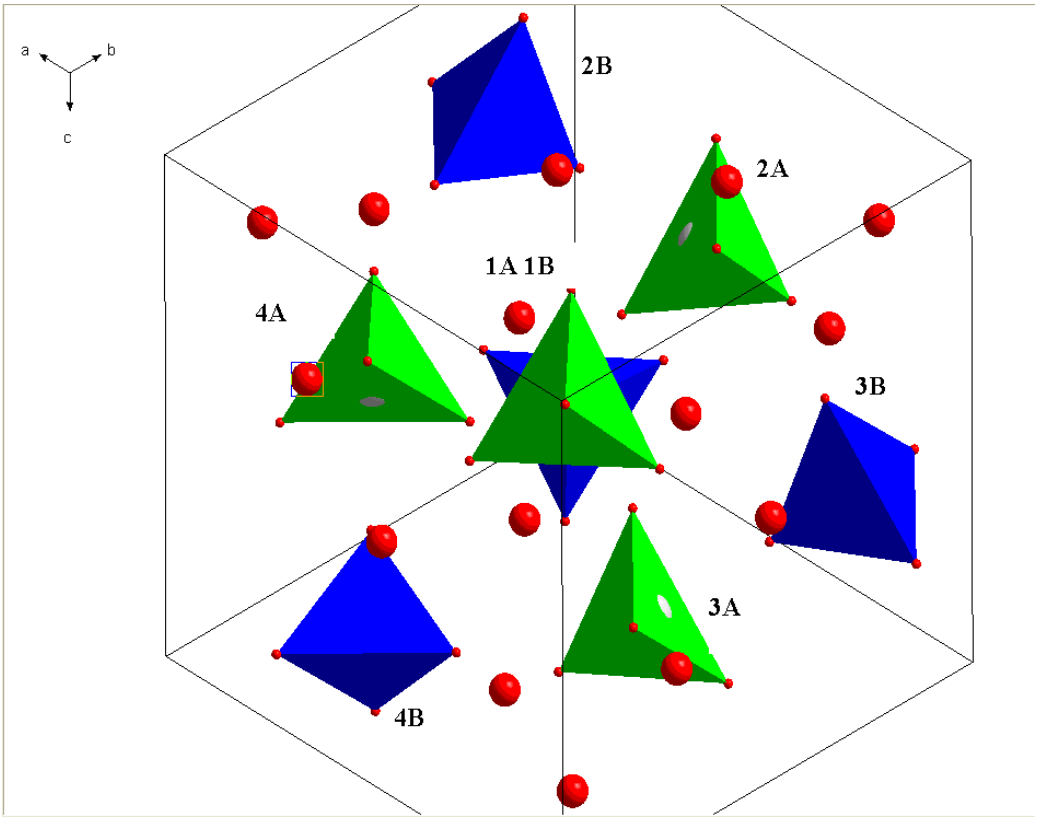

Figure 5.3. Unit cell arrangement of four pairs of WO_4 tetrahedra for α-ZrW_2O_8 in space group *P2₁3* viewed down the threefold symmetry axis of a pair of tetrahedra. Green tetrahedra (A) are symmetry equivalents of the first W atom in a formula unit, while blue tetrahedra (B) are symmetrically equivalent to the second W atom in the unit, with oxygen atoms shown in red. Zr atoms have been removed for clarity.

The cubic form of $ZrMo_2O_8$ was first synthesized by our group in 1998 by dehydrating $ZrMo_2O_7(OH)_2{\cdot}2H_2O$.[8] Prior to this, $ZrMo_2O_8$, was known as monoclinic (*C2/c*) and trigonal (*P-3c*) polymorphs.[26-29] Cubic $ZrMo_2O_8$ crystallizes in space group *Pa-3* and is isostructural to β-ZrW_2O_8. *In-situ* diffraction studies of cubic $ZrMo_2O_8$ have shown that it is stable up to 673 K and that it has a thermal expansion coefficient of -5.0 x 10^{-6} K^{-1} from 11 to 573 K.[8] Above 673 K, cubic $ZrMo_2O_8$ undergoes an irreversible

phase transition to the trigonal polymorph. $ZrMo_2O_8$ does not adopt a structure similar to that of α-ZrW_2O_8 under any conditions.

Unlike cubic ZrW_2O_8, which undergoes a phase transition to an orthorhombic phase at 0.21 GPa,[30] cubic $ZrMo_2O_8$ has been shown to be stable up 0.6 GPa under hydrostatic conditions.[13] As pressure is increased from 0.7 to 2.0 GPa, $ZrMo_2O_8$ under goes a fully reversible first order phase transition.[13] As the pressure is increased to ~1.7 GPa, $ZrMo_2O_8$ begins pressure induced amorphization (PIA) which is complete by the time the pressure approaches 3.5 GPa.[23]

We have used the pair distribution function (PDF) method to examine the local structure of $ZrMo_2O_8$. This is a real space method used to determine the interatomic distances within a material. A PDF is obtained by the Fourier-transformation of the structure function, S(Q) ($Q = 4\pi\sin\theta/\lambda$). The structure factor S(Q) is calculated as follows[31]:

$$S(Q) = \frac{I^{coh}(Q) - \sum c_i \left| f_i(Q) \right|^2}{\left| \sum c_i f(Q) \right|^2} + 1 \qquad (1)$$

Where I(Q) is the intensity measured from a powdered sample and f_i is the form factor of the atom, and c_i is atomic concentration. At high Q, S(Q) approaches 1. G(r), the PDF, is calculated as follows[31]:

$$G(r) = (2/\pi) \int_{Q=0}^{Q\max} Q[S(Q) - 1]\sin(Qr)dQ \qquad (2)$$

The peak maxima in G(r) correspond to the distances between pairs of atoms in the sample.

This chapter describes our local structure studies of $ZrMo_2O_8$ using the PDF method. We examined how the local structure of the material is affected by both pressure and temperature.

5.2 Experimental

5.2.1 *In-situ* Variable Temperature Experiment

A $ZrMo_2O_8$ sample was packed in a kapton capillary tube and mounted on a crystallographic goniometer head. Diffraction data were collected at the Advanced Photon Source, Argonne National Lab, beam line 11-ID-B using x-rays with $\lambda = 0.2128$Å. An Oxford Cryosystem's Cryostream 700 was used to ramp the sample temperature while x-ray data were acquired. 2D diffraction images were recorded on an amorphous silicon General Electric Healthcare detector with 2048 x 2048 pixels.[32] Data were collected in sets of twenty exposures with each exposure lasting 6 s, with 22 s to average the data set before the next set of exposures, totaling 142 s. Data were collected continuously while the sample was first cooled to 120 K at 6 K/min, as a lower temperature may have led to ice formation, then heated to 500 K, the upper temperature limit of the apparatus, at 4 K/min, cooled again to 120 K at 4 K/min, and finally reheated to 300 K at 6 K/min. The sample was held at temperature for 10 min between each heating and cooling segment. Temperatures were estimated from the known temperature

ramp and the initial temperature on the cryostat display as the shutter was opened for the first set of exposures.

Sets of exposures were averaged, summed, then integrated into one file using FIT-2D.[33] Integrated files were imported into PDFgetX2[34] to generate the pair distribution functions (PDF). The PDFs were modeled using the program PDFfit2 with the PDFgui interface.[35]

For each data set, peaks corresponding to the first Mo-O, Zr-O, and Zr-Mo correlations, at ~1.75, 2.10, and 3.79 Å, were fit with a Gaussian and the estimated positions and widths of the peaks recorded.

5.2.2 *In-situ* Variable Pressure Experiment

Data were collected for $ZrMo_2O_8$ at room temperature at up to ~8 GPa in a Diacell Bragg-(S) two screw DAC. The diamonds in this beryllium backed cell had 600 μm culets. A stainless steel, pre-indented gasket 105 μm thick was drilled using EDM to have a 300 μm diameter hole. Before loading, the sample was ground using a mortar and pestle to reduce the grain size of the sample, and, hence, improve the powder sampling statistics. A 4:1 mixture of methanol to ethanol was used as the pressure transmitting medium. This medium was chosen because it is hydrostatic up to 10.4 GPa.[36] Diffraction data were collected at the Advanced Photon Source, Argonne National Lab, beam line 11-ID-B using x-rays with λ= 0.2128 Å. 2D diffraction images were captured on an amorphous silicon based General Electric Healthcare detector with 2048 x 2048 pixels.[32] Data sets were collected one hundred exposures at a time with each exposure lasting 15 s.

Each set of exposures was averaged to form a usable data file. At each pressure, 8-12 summed average files were acquired. Data were integrated using FIT-2D[33] and imported into PDFgetX2[34] to generate the PDFs.

The pressure in the DAC was estimated using the ruby fluorescence technique. The reported pressure is the average of those determined before and after each exposure. Errors in pressure calibration for the ruby fluorescence technique are often between 0.05 and 0.1 GPa.[37]

5.3 Results and Discussion

5.3.1 Local Structure at Ambient Temperature and Pressure

Figure 5.4 shows the pair distribution function generated from PDFgetX2[34] along with the calculated PDF generated from PDFfit2 with the PDFgui[35] interface for $ZrMo_2O_8$ in space group $P2_13$. Partial PDF's have been calculated for each element pair and are shown below the difference curve. In general, the calculated PDF gives quite poor agreement up to 20 Å.

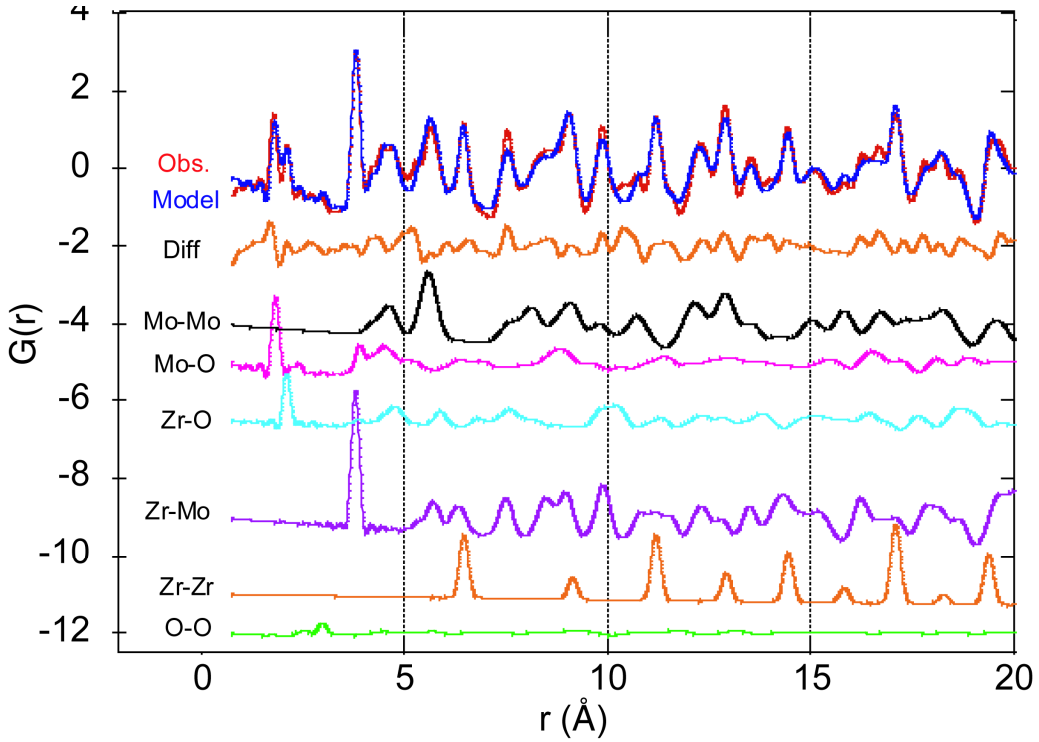

Figure 5.4. A comparison of the expereimental PDF for $ZrMo_2O_8$ (red) that was calculated from a *P2₁3* model (blue) out to 20 Å. The difference curve is shown directly below in orange, along with the partial PDFs derived from the model.

A closer look at the calculated PDF from 0-10 Å (Figure 5.5) shows that there are major discrepancies between the observed PDF and the model just before 6 Å. In *P2₁3* a Mo-Mo distance of 5.62 Å is predicted, but the shoulder observed at 5.28 Å is not predicted by the model. This model predicts accurately distances for the first Mo-O, Zr-O, and Mo-Zr distances at 1.75, 2.10, and 3.79 Å respectively. However, the absence of the shoulder in the shoulder at 5.28 Å is a significant flaw in the *P2₁3* model.

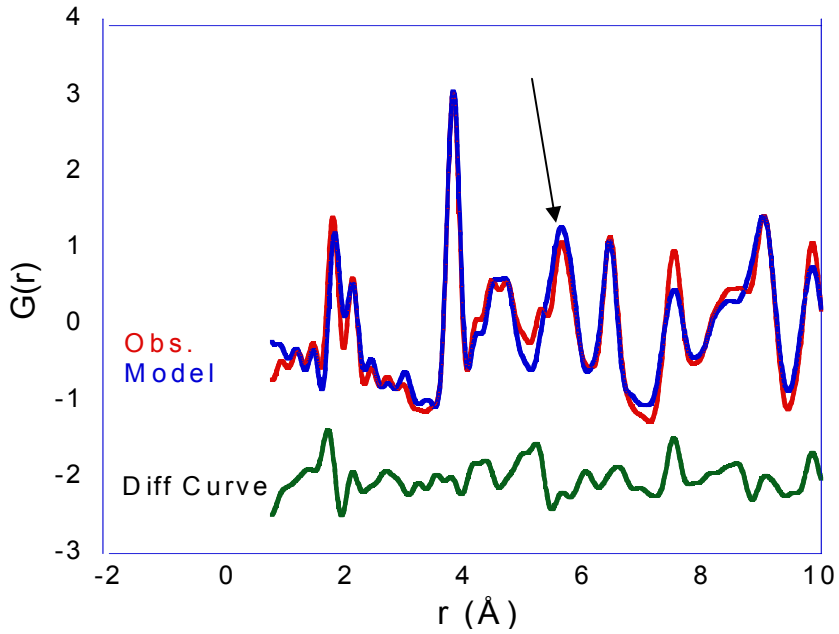

Figure 5.5. The experimental PDF (red) compared to the model calculated (blue) for $ZrMo_2O_8$ from 0 – 10 Å. The difference curve is shown below in green. Missing atomic correlations are marked by black arrows.

$ZrMo_2O_8$ crystallizes in space group *Pa-3,* which is the space group for β-ZrW_2O_8. We can compare the experimental PDF for $ZrMo_2O_8$ to that predicted by the disordered crystallographic model for β-ZrW_2O_8. Figure 5.6 shows the observed G(r) and the computed PDFs from 0-20 Å. Space group of *Pa-3* gives a better fit at high r, but there are still discrepancies at low r. While the disordered *Pa-3* model works well at long distances, it does not adequately describe the materials local structure.

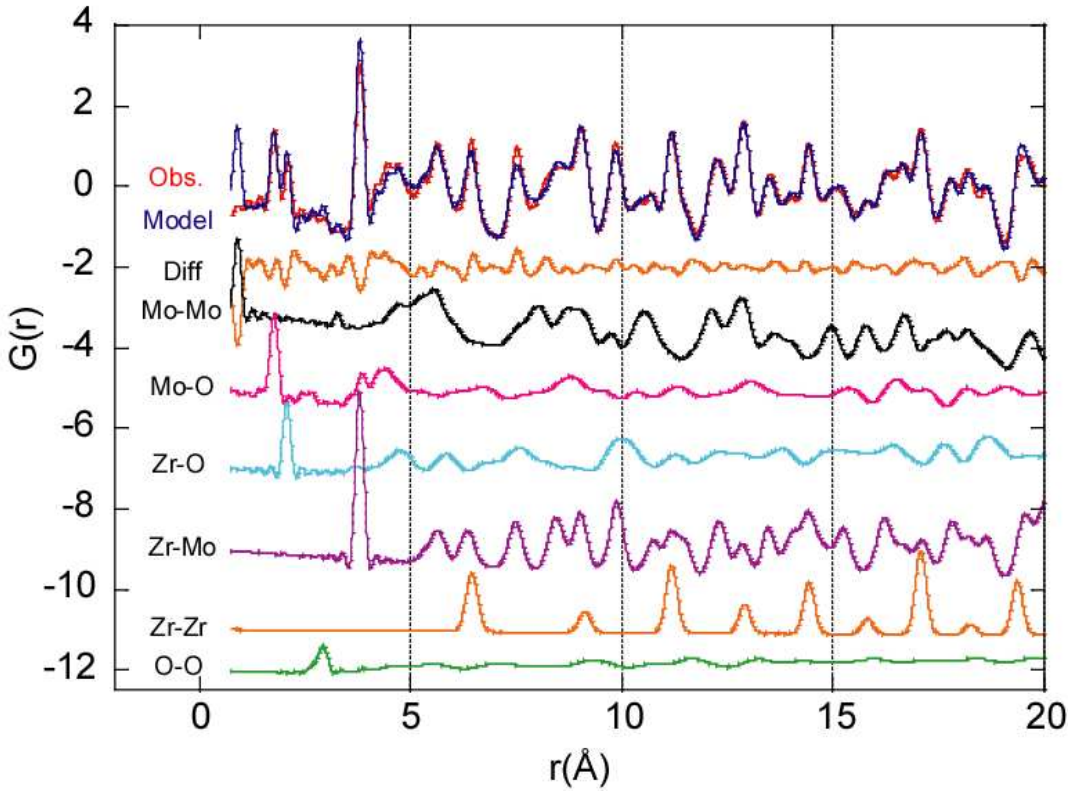

Figure 5.6. The experimental PDF for $ZrMo_2O_8$ (red) compared to that computed for a *Pa-3* (blue) model out to 20 Å. The difference curve is shown directly below in orange as are the partial PDFs.

In the calculated PDF, a significant discrepancy occurs at 0.78 Å corresponding to a suggested Mo-Mo correlation. This correlation is not real and can be explained using the diagram from Evans *et. al.* showing the phase transition and oxygen mobility of ZrW_2O_8.[14] Each unit cell of $ZrMo_2O_8$ contains four formula units, and each formula unit has a pair of MoO_4 tetrahedra that will either be located in either the W_{1A} and W_{2A} direction or W_{1B} and W_{2B} direction. The distance of 0.78 Å corresponds to molybdenum atoms occupying the paired positions (W_{1A}, W_{1B}) and (W_{2A}, W_{2B}) instead of one atom at each site. The PDF is calculated from all possible distances in the crystal structure including what would be a pair of Mo atoms in a formula unit at the pair of positions (W_{1A}, W_{1B}), so this correlation can be ignored. As with the above model the peaks

appearing at 1.75, 2.10, and 3.79 Å are the first correlations between the Mo-O, Zr-O, and Mo-Zr pairs of atoms. Unlike the $P2_13$ model, the correlation peak at 5.28 Å is accounted for by the *Pa-3* model (Figure 5.7). The extra peak is a result of a combination of the Mo-Mo distances and the Zr-Mo distances which overlap in the calculated *Pa-3* model.

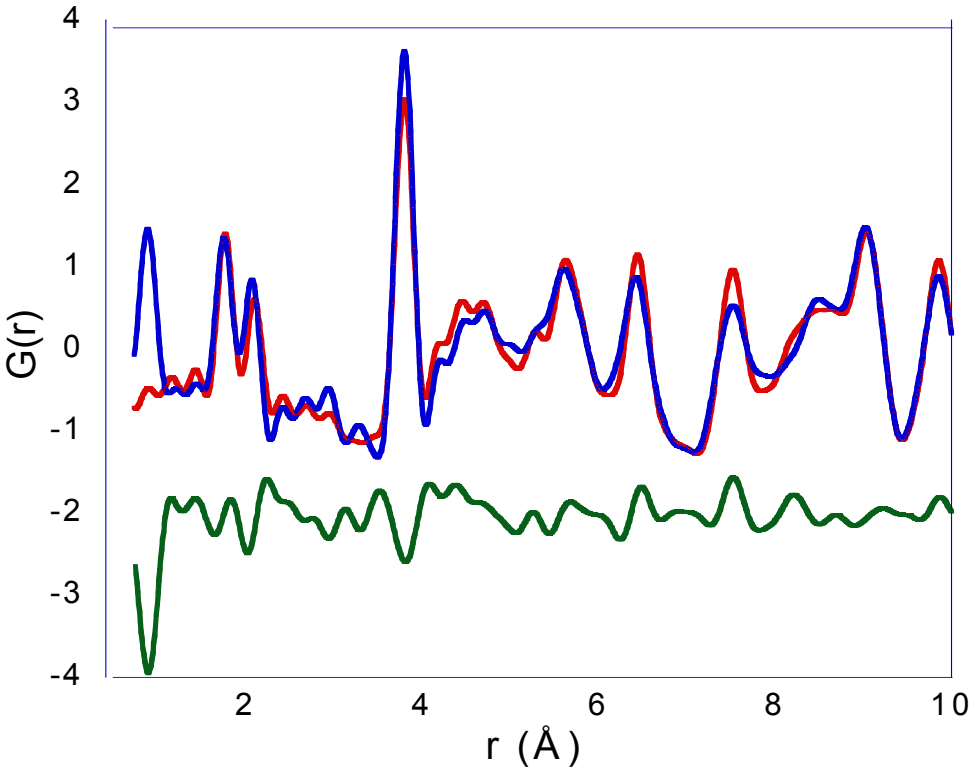

Figure 5.7. The experimental PDF (red) compared to the *Pa-3* model (blue) for $ZrMo_2O_8$. The difference curve is shown below in green.

5.3.2 Variable Temperature Study of Local Structure

The Mo-O, Zr-O, and Zr-Mo distances calculated from fitting the appropriate correlation peaks to a Gaussian are plotted against both scan number and temperature in Figures 5.8-5.10. As the temperature was lowered from room temperature to 120 K, the average nearest neighbor Mo-O distance decreased from 1.7545 to 1.7514 Å, while the Zr-O distance changed from 2.0980 to 2.0914 Å, and the nearest neighbor Zr-Mo distance increased from 3.7962 to a maximum of 3.7982 Å. Minimum Mo-O and Zr-O distances of 1.7498 Å and 2.0910 Å respectively, were observed at ~150 K as the temperature was being raised to 500 K. The Mo-O and Zr-O distances generally increase in length to 1.7583 Å and 2.1048 Å, while Zr-Mo distances decrease to a minimum of 3.7905 Å at ~470 K as the temperature is being increased to 500 K, and have a distance of 3.7907 Å at 500 K. The increase in the bonded Mo-O and the Zr-O distances is expected since these atom pairs behave like anharmonic oscillators. The decrease in the Zr-Mo distance as the temperature is increased, is presumably due to the transverse vibrations of the bridging oxygen associated with the polyhedral rocking leading to NTE.

Upon recooling the sample to 120 K, a maximum Mo-O distance of 1.7594 Å is observed at ~470 K, while at 120 K the distance is 1.7533 Å. The minimum distance in this temperature cycle, however, is observed at ~240 K with a distance of 1.7527 Å. On recooling to 120 K, the Zr-O distance reaches a maximum of 2.1077 Å at ~470 K and decreases to a local minimum of 2.0916 Å at 120 K. The Zr-Mo distance increases to a value of 3.7973 Å at 120 K. As the sample is heated back to room temperature, the Mo-O, Zr-O, and Zr-Mo distances are 1.7578, 2.1002, and 3.7952 Å respectively.

Theoretically the shortest and longest distances for nearest neighbor Mo-O and Zr-O correlations should occur at 120 K and 500 K respectively. For Zr-Mo correlations the longest separation should be at 120 K and the shortest separation at 500 K. Mo-O and Zr-O maximum distances were observed at 470 K and not at 500 K as expected. We can attribute this error to several factors. First, a slight miscalculation of the temperature could have happened, as this was estimated from the temperature ramp and the temperature as the shutter opened on the first data set. The temperature curve is perfectly smooth because of the estimation. Typically the temperature would be recorded as the shutter was opened and closed and would be recorded with a time stamp on the computer software, and the average value would have slight variance. The other possibility is that the temperature of the sample lagged behind the temperature of the cryostream. As the sample may change temperature at a different rate than the cryostream, and the temperature of the cryostream was reported the actual temperature of the sample may vary by several degrees. In Figures 5.9 and 5.10 it can be seen that the apparent Zr-O and Zr-Mo distance vary in a systematic and reversible fashion on heating/cooling. This is not so for the apparent Mo-O distance. The origin of this effect is not clear.

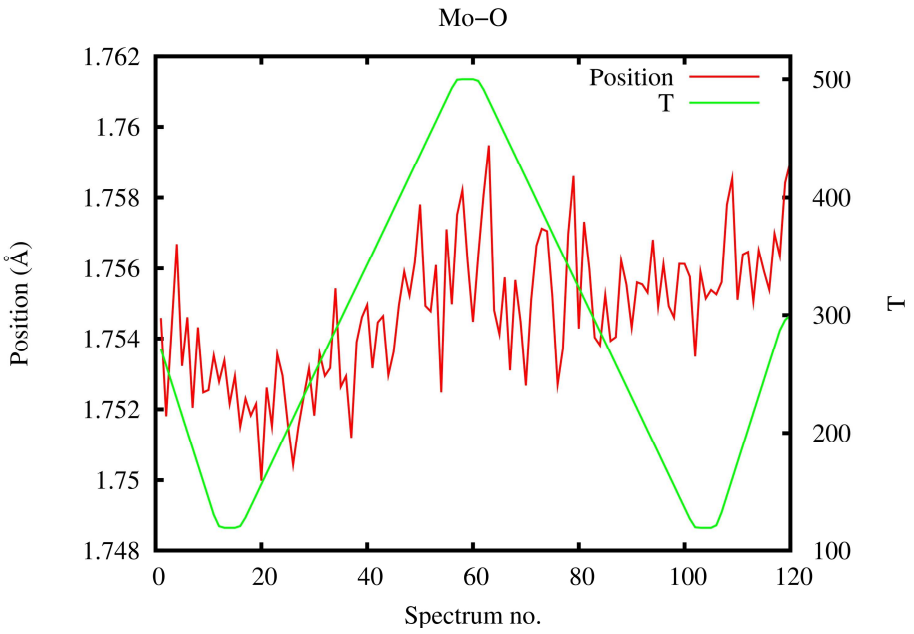

Figure 5.8. The calculated average Mo-O distance (red) from the experimental PDFs and the temperature in Kelvin (green) plotted as a function of the diffraction pattern number.

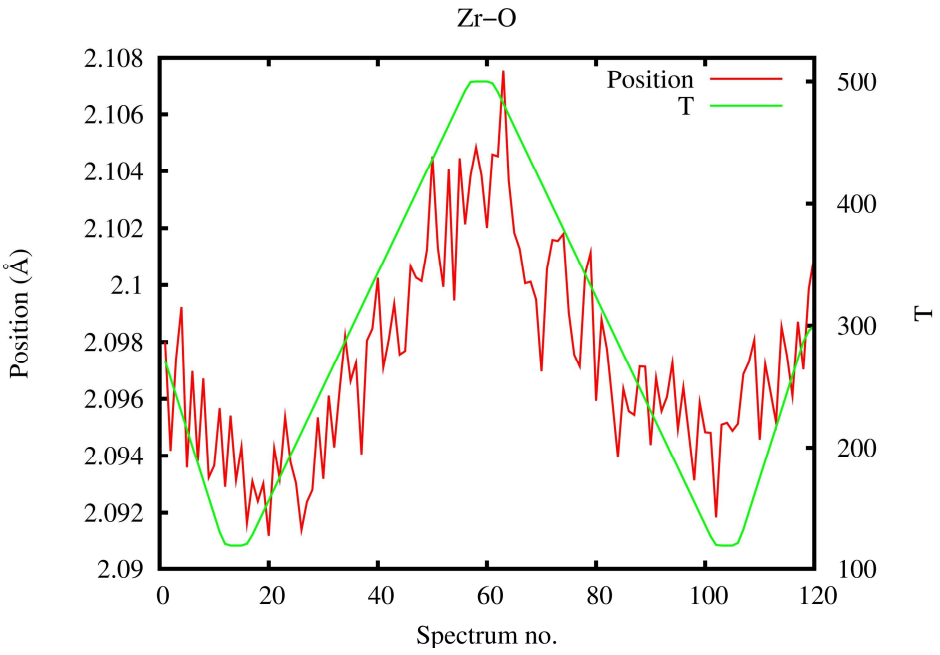

Figure 5.9. The calculated average Zr-O distance (red) from the experimental PDFs and the temperature in Kelvin (green) plotted as a function of the diffraction pattern number over time.

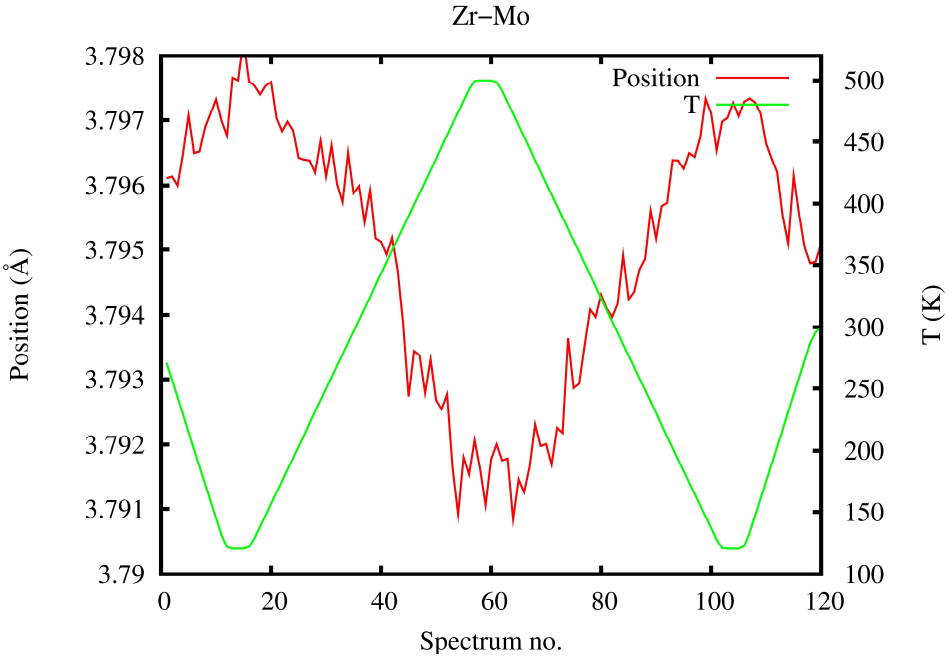

Figure 5.10. The calculated average Zr-Mo distance (red) from the experimental PDFs and the temperature in Kelvin (green) plotted as a function of the diffraction pattern number over time.

The width of the Zr-O and Zr-Mo correlation peaks are shown in Figures 5.11 and 5.12. These widths vary with the temperature in a physically reasonable fashion. As temperature is increased, the width increases due to enhanced vibrational motion. There is no systematic trend in the width of the Mo-O correlation peaks with temperature (Figure 5.13).

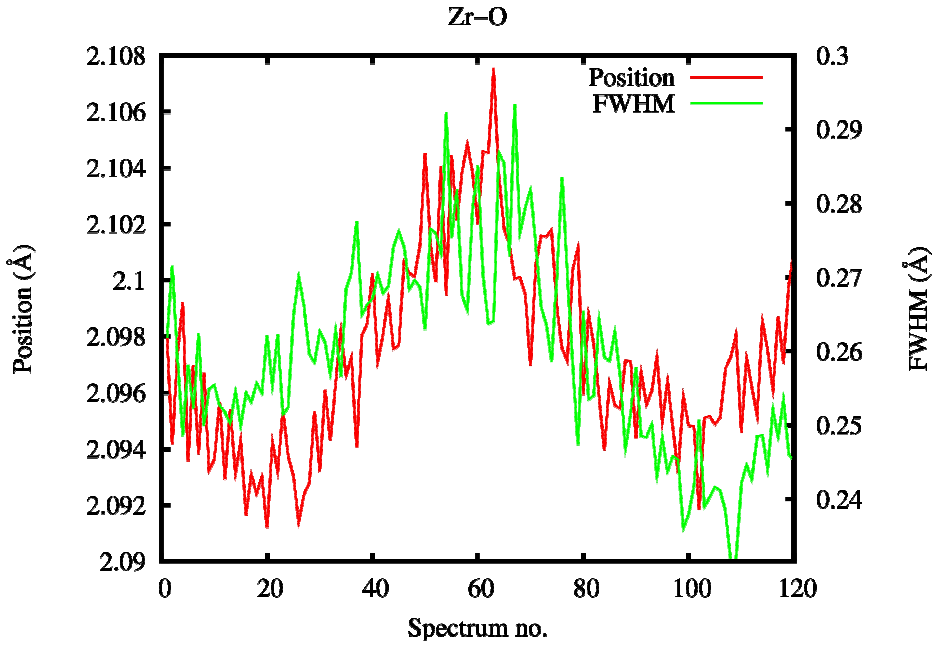

Figure 5.11. The calculated Zr-O distance (red) from the experimental PDFs and the full width at the peaks half maximum for the Zr-O correlation peaks (green) plotted as a function of the spectrum number.

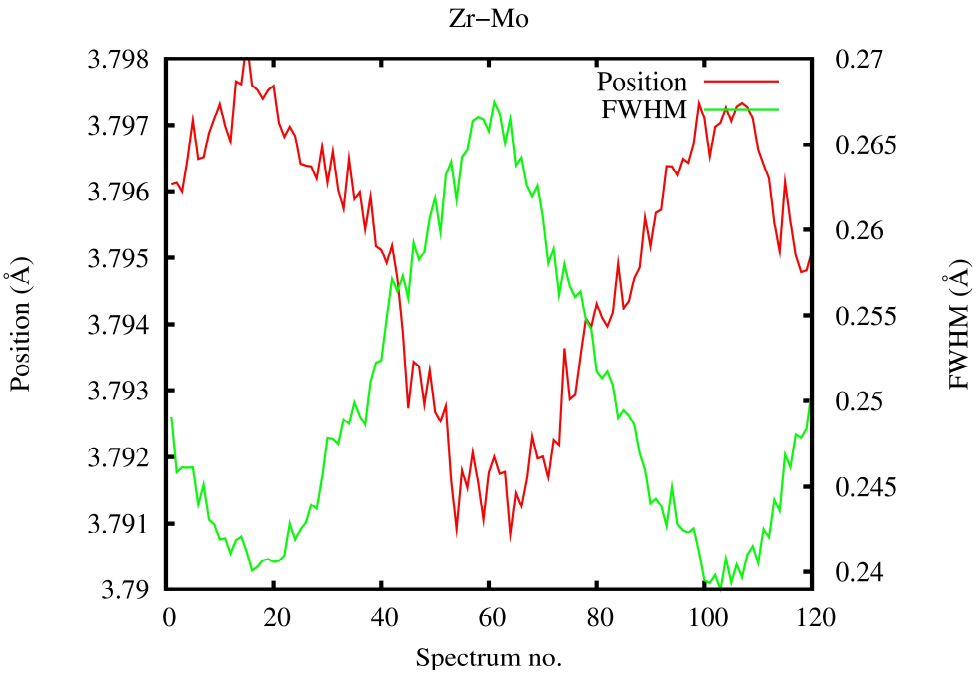

Figure 5.12. The calculated Zr-Mo distance (red) from the experimental PDFs and the full width at the peaks half maximum for the Zr-Mo correlation peaks (green) plotted as a function of the spectrum number.

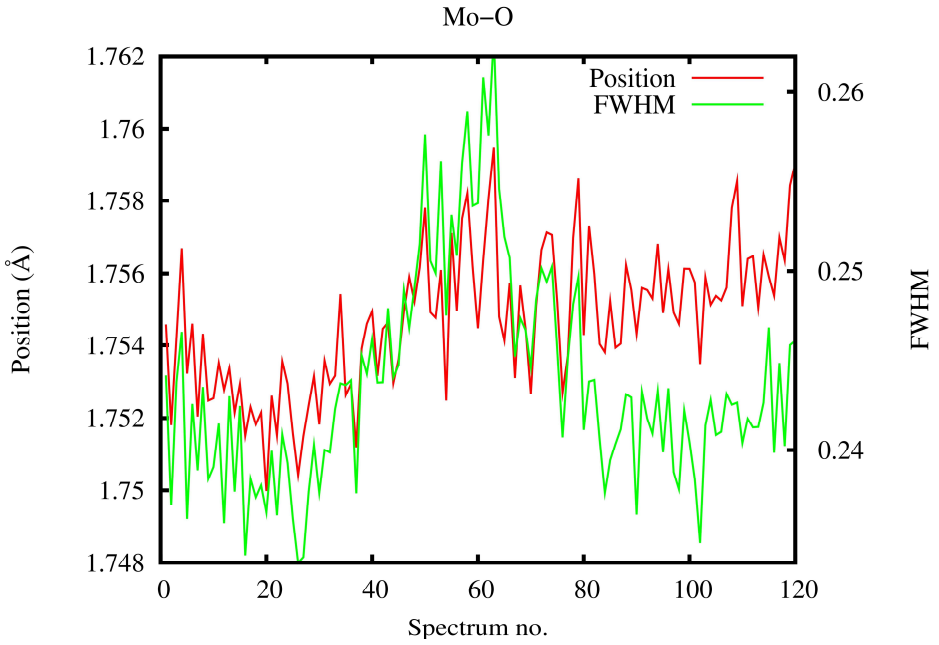

Figure 5.13. The calculated Mo-O distance (red) from the experimental PDFs and the full width at the peaks half maximum for the Mo-O correlation peaks (green) plotted as a function of the spectrum number.

5.3.3 Local Structure as a Function of Pressure

Figure 5.14 shows the PDFs generated up to 10 Å for all of the pressures examined. At ambient pressure, the interatomic distances between atoms are easily distinguishable for $ZrMo_2O_8$ past 20 Å with a Q_{max} = 150 nm^{-1}. The Zr-Mo nearest neighbor distance at ambient pressure occurs at 3.80 Å while the Mo-O and Zr-O maxima occur at 1.77 Å and 2.15 Å respectively. The quite large difference (~1.1% and ~2.3%) in apparent Mo-O and Zr-O distances between the high pressure and variable temperature measurements is presumably a consequence of the different sample environments. The diamond anvil cell introduces a lot of background, which must be removed in order to generate a usable G(r). Data from the DAC was only recorded out to a usable Q_{max}, of 150 nm^{-1} as opposed

to the 220 nm^{-1} for the data acquired with this sample in a kapton capillary tube. The reduced Q_{max} lowers the resolution of G(r) and introduces additional artifacts into G(r).

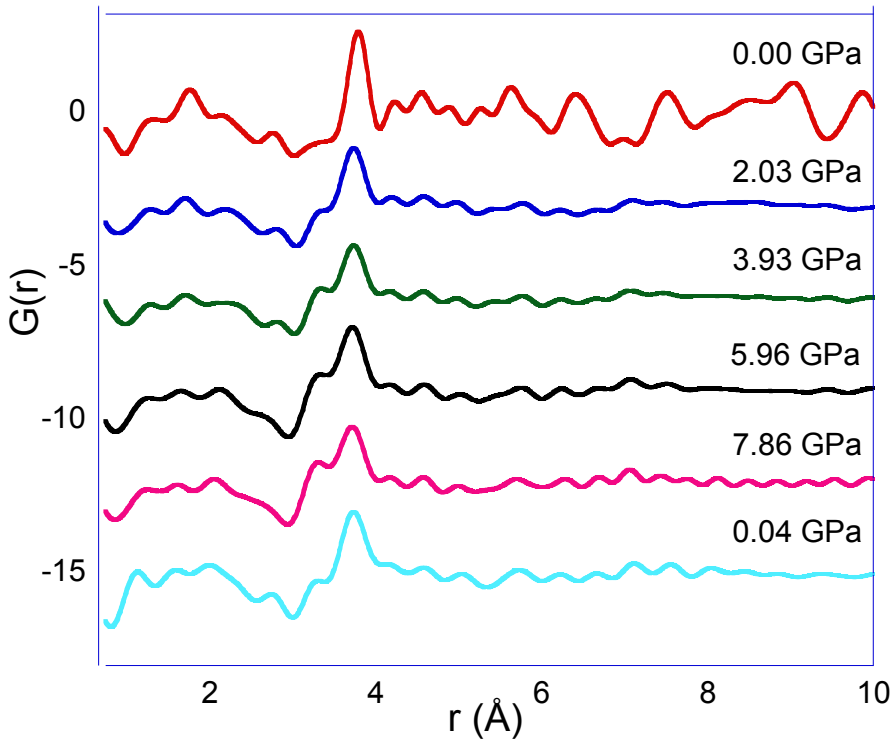

Figure 5.14. Experiment PDF for $ZrMo_2O_8$ on compression. Q_{max} was 150 nm^{-1} for all the G(r). The bottom G(r) (0.04 GPa) was recorded on decompression.

As the pressure is increased to 2.03 GPa, most of the interatomic correlations above 4 Å are washed out. This is expected since $ZrMo_2O_8$ has been reported to begin PIA at ~1.7 GPa.[23] At this pressure, a shoulder starts to form at ~3.36 Å before the Zr-Mo distance at 3.74 Å, very likely the result of a decrease in the Zr-O-Mo bond angle as the polyhedra are being compressed into the void space of the unit cell. The Zr-O-Mo linkages in the framework are apparently very robust and are not destroyed or massively

deformed under pressure. The peak at ~3.36 Å is increasing in intensity, while the Zr-Mo correlation at ~3.74 Å is decreasing in intensity as the pressure is increased. This suggests that the additional peak forming is also a Zr-Mo correlation. Upon decompression in the DAC, $ZrMo_2O_8$ remains amorphous. However, the intensity of the peak at ~3.36 Å diminishes and the Zr-Mo correlation at ~3.75 Å increases in size suggesting that this transformation is reversible in amorphous $ZrMo_2O_8$.

5.4 Conclusions

We have attempted to discern the local structure of $ZrMo_2O_8$ by the PDF method. When the experimental PDF at room temperature was fit with space group $P2_13$, the overall fit of the model was quite poor at all distances up to 20 Å. However, this model does predict the first Mo-O, Zr-O, and Zr-Mo distances accurately. As the experimental PDF is compared to the *Pa-3* disordered model, a better fit is obtained at large r. At low r, however, the fit is still quite poor suggesting more work needs to be performed to understand the short range structure of the material.

As the temperature is varied, the Mo-O and Zr-O nearest neighbor separations increase with increasing temperature as expected. However, as the sample is cooled the behavior of the Zr-O separation is reversible, but this is not the case for the Mo-O average nearest neighbor separation. The Zr-Mo distance decreases with increasing temperature and is reversible on cooling. The temperature dependence of the Zr-Mo distance is very similar to the overall CTE for $ZrMo_2O_8$.

We were able to generate PDFs for $ZrMo_2O_8$ in a DAC using a Q_{max} of 150 nm^{-1}. As the pressure increased above 2 GPa, $ZrMo_2O_8$ undergoes a PIA that is irreversible on

decompression. Above 4 Å, there are no well defined peaks in the PDF. A well defined nearest neighbor Zr-Mo correlation peak at ~ 3.74 Å indicates that the Zr-O-Mo links are still well defined in the amorphized material. At ~2 GPa, a new Zr-Mo correlation appears at ~3.36 Å. As the pressure is increased, the intensity of this peak increases, and the intensity of the Zr-Mo peak at 3.74 Å decreases. The formation of this peak is reversible upon decompression and suggests that the Zr-O-Mo links may change geometry on compression.

5.5 References

1. Evans, J. S. O.; Mary, T. A.; Vogt, T.; Subramanian, M. A.; Sleight, A. W., Negative Thermal Expansion in ZrW_2O_8 and HfW_2O_8. *Chem. Mater.* **1996,** 8, 2809-2823.

2. Sleight, A. W., Compounds that Contract on Heating. *Inorg. Chem.* **1998,** 37, 2854-2860.

3. Evans, J. S. O.; Mary, T. A.; Sleight, A. W., Negative thermal expansion materials. *Physcia B* **1998,** 241-243, 311-316.

4. Evans, J. S. O., Negative Thermal Expansion Materials. *J. Chem. Soc. Dalton Trans.* **1999**, 3317-3326.

5. Evans, J. S. O.; Mary, T. A.; Sleight, A. W., Negative Thermal Expansion in a Large Molybdate and Tungstate Family. *J. Solid State Chem.* **1997,** 133, 580-583.

6. Ravindran, T. R.; Arora, A. K.; Mary, T. A., High-pressure Raman spectroscopic study of zirconium tungstate. *J. Phys. Condens. Matter.* **2001,** 13, 11573-11588.

7. Wilkinson, A. P.; Lind, C.; Pattanaik, S., A New Polymorph of ZrW_2O_8 Prepared using Nonhydrolytic Sol-Gel Chemistry. *Chem. Mater.* **1999,** 11, 101-108.

8. Lind, C.; Wilkinson, A. P.; Hu, Z.; Short, S.; Jorgensen, J. D., Synthesis and Properties of the Negative Thermal Expansion Material Cubic Zirconium Molybdate. *Chem. Mater.* **1998,** 10, 2335-2337.

9. Baiz, T. I.; Gindhart, A. M.; Kraemer, S. K.; Lind, C., Synthesis of MgHf(WO4)(3) and $MgZr(WO_4)_3$ using a non-hydrolytic sol-gel method. *J. Sol-Gel Sci. Tech.* **2008,** 47, 128-130.

10. Pryde, A. K. A.; Hammonds, K. D.; Dove, M. T.; Heine, V.; Gale, J. D.; Warren, M. C., Origin of the Negative Thermal Expansion in ZrW_2O_8 and ZrV_2O_7. *J. Phys. Condens. Matter* **1996,** 8, 10973-10982.

11. Losilla, E. R.; Cabeza, A.; Bruque, S.; Aranda, M. A. G.; Sanz, J.; Iglesias, J. E.; Alonso, J. A., Syntheses, Structures, and Thermal Expansion of Germanium Pyrophosphates. *J. Solid State Chem.* **2001,** 156, 213-219.

12. Varga, T.; Wilkinson, A. P.; Haluska, M.; Payzant, E. A., Preparation and thermal expansion of $(M^{III}_{0.5}M'^{V}_{0.5})P_2O_7$ with the ZrP_2O_7 structure. *J. Solid State Chem.* **2005,** 178, 3541-3546.

13. Lind, C.; VanDerveer, D. G.; Wilkinson, A. P.; Chen, J.; Vaughan, M. T.; Weidner, D. J., New high pressure form of the negative thermal expansion materials zirconium molybdate and hafnium molybdate. *Chem. Mater.* **2001,** 13, 487-490.

14. Evans, J. S. O.; David, W. I. F.; Sleight, A. W., Structural investigation of the negative-thermal-expansion material ZrW_2O_8. *Acta Cryst.* **1999,** B55, 333-340.

15. Evans, J. S. O.; Jorgensen, J. D.; Short, S.; David, W. I. F.; Ibberson, R. M.; Sleight, A. W., Thermal expansion in the orthorhombic γ-phase of ZrW_2O_8. *Phys. Rev. B* **1999,** 60, 14643-14648.

16. Jorgensen, J. D.; Hu, Z.; Teslic, S.; Argyriou, D. N.; Short, S.; Evans, J. S. O.; Sleight, A. W., Pressure -induced cubic-to-orthorhombic phase transition in ZrW_2O_8. *Phys. Rev. B* **1999,** 59, 215-225.

17. Lind, C.; Wilkinson, A. P.; Rawn, C. J.; Payzant, E. A., Preparation of the negative thermal expansion material cubic $ZrMo_2O_8$. *J. Mater. Chem.* **2001,** 11, 3354-3359.

18. Lind, C.; Wilkinson, A. P.; Rawn, C. J.; Payzant, A. E., Kinetics of the cubic to trigonal transformation in $ZrMo_2O_8$ and their dependence on precursor chemistry. *J. Mater. Chem.* **2002,** 12, 990-994.

19. Achary, S. N.; Mukherjee, G. D.; Tyagi, A. K.; K., G. B., New polymorph of $HfMo_2O_8$ synthesized using a high-pressure and high-temperature toroid anvil setup. *Phys. Rev. B* **2002,** 66, 184106.

20. Varga, T.; Lind, C.; Wilkinson, A. P.; Xu, H.; Lesher, C. E.; Navrotsky, A., Heats of Formation for Several Crystalline Polymorphs and Pressure-Induced Amorphous Forms of AMo_2O_8 (A = Zr, Hf) and ZrW_2O_8). *Chem. Mater.* **2007,** 19, 468-476.

21. Kennedy, C. A.; White, M. A.; Wilkinson, A. P.; Varga, T., Heat capacity, lattice dynamics, and thermodynamic stability of the negative thermal expansion material $HfMo_2O_8$. *Phys. Rev. B* **2007,** 75, 9.

22. Varga, T.; Wilkinson, A. P.; Lind, C.; Basset, W. A.; Zha, C.-S., Pressure-induced amorphization of cubic $ZrMo_2O_8$ studied in-situ by x-ray absorption spectroscopy and diffraction. *Solid State Commun.* **2005,** 135, 739-744.

23. Varga, T.; Wilkinson, A. P.; Jupe, A. C.; Lind, C.; Bassett, W. A.; Zha, C.-S., Pressure-induced amorphization of cubic ZrW_2O_8 studied in-situ and ex-situ by synchrotron x-ray absorption spectroscopy and diffraction. *Phys. Rev. B* **2005,** 72, 024117-(1-10).

24. Graham, J.; Wadsley, A. D.; Weymouth, J. H.; Williams, L. S., A New Ternary Oxide, ZrW_2O_8. *J. Am. Ceram. Soc.* **1959,** 42, 570.

25. Mary, T. A.; Evans, J. S. O.; Vogt, T.; Sleight, A. W., Negative Thermal Expansion from 0.3 to 1050 Kelvin in ZrW_2O_8. *Science* **1996,** 272, 90-92.

26. Auray, M.; Quarton, M.; Tarte, P., Crystal Data for Two Molybdates $M(MoO_4)_2$ with M = Zr, Hf. *Powder Diffraction* **1987,** 2, 36-38.

27. Auray, M.; Quarton, M., Revised Crystal Data of $Zr(MoO_4)_2$, L.T. Form. *Powder Diffraction* **1989,** 4, 29-30.

28. Auray, M.; Quarton, M.; Tarte, P., New Structure of High Temperature Zirconium Molybdate. *Acta Cryst.* **1986,** C42, 257-259.

29. Serezhkin, V. N.; Efremov, V. A.; Trunov, V. K., The Crystal Structure of α-$Zr(MoO_4)_2$, the High-temperature Modification of Zirconium Molybdate. *Russian Journal of Inorganic Chemistry* **1987,** 32, 1566-1570.

30. Jorgensen, J. D.; Hu, Z.; Short, S.; Sleight, A. W.; Evans, J. S. O., Pressure-induced cubic-to-orthorhombic phase transfromation in the negative thermal expansion material HfW_2O_8. *J. Appl. Phys.* **2001,** 89, 3184-3188.

31. Billinge, S. J. L.; Kanatzidis, M. G., Beyond crystallography: the study of disorder, nanocrystallinity and crystallographically challenged materials with pair distribution functions. *Chem. Commun.* **2004,** 7, 749-760.

32. Lee, J. H.; Aydiner, C. C.; Almer, J.; Bernier, J.; Chapman, K. W.; Chupas, P. J.; Haeffner, D.; Kump, K.; Lee, P. L.; Lienert, U.; Miceli, A.; Vera, G., Synchrotron applications of an amorphous silicon flat-panel detector. *J. Synchrotron Radiat.* **2008,** 15, 477-488.

33. Hammersley, A. P.; Svensson, S. O.; Hanfland, M.; Fitch, A. N.; Hausermann, D., Two-dimensional detector software: From real detector to idealised image or two-theta scan. *High Press. Res.* **1996,** 14, 235-248.

34. Qiu, X.; Thompson, J. W.; Billinge, S. J. L., PDFgetX2: a GUI-driven program to obtain pair distribution function from X-ray powder diffraction data. *J. Appl. Cryst.* **2004,** 37, 678.

35. Farrow, C. L.; Juhas, P.; Liu, J. W.; Bryndin, D.; Bozin, E. S.; Bloch, J.; Proffen, T.; Billinge, S. J. L., PDFfit2 and PDFgui: computer programs for studying nanostructure in crystals. *J. Phys. Condens. Matter* **2007,** 19, 7.

36. Miletich, R.; Allan, D., R.; Kuhs, W., F., High-Pressure Single-Crystal Techniques. *Rev. Mineral. Geochem.* **2001,** 41, (High-Temperature and High-Pressure Crystal Chemistry), 445-519.

37. Barnett, J. D.; Block, S.; Piermarini, G. J., An Optical Fluorescence System for Quantitative Pressure Measurement in the Diamond-Anvil Cell. *Rev. Sci. Instrum.* **1973,** 44, 1.

CHAPTER 6

CONCLUSIONS

In this thesis we have examined some members of the $A_2M_3O_{12}$, AX_2O_7, and AM_2O_8 framework families as part of an effort to better understand how chemical modification effects the physical properties of these frameworks.

In Chapter 2, we used *in-situ*, variable temperature x-ray diffraction to examine the thermal expansion characteristics of $Zr_2(PO_4)_2(SO_4)$. We learned that $Zr_2(PO_4)_2(SO_4)$ exhibits anisotropic positive thermal expansion from 120 to 500 K, but unlike many other members of this family, its overall expansion coefficient is positive. The *b* and *c* axes of $Zr_2(PO_4)_2(SO_4)$ contract on heating while *a* expands. The expansion along the *a* axis more than compensates for the contractions along *b* and *c* leading to overall positive thermal expansion.

Thermogravimetric analysis of $Zr_2(PO_4)_2(SO_4)$ shows decomposition in three steps as the temperature is increased to 800 ºC. The most significant weight loss for the material occurred between 100 and 150 ºC, and was attribute to the loss of hydroxyl defects from within the structure of $Zr_2(PO_4)_2(SO_4)$. In the variable temperature diffraction experiment, we observed an irreversible change in lattice constants confirming the loss of water from within the crystal structure. Density measurements on "$Zr_2(PO_4)_2(SO_4)$" were also consistent with the presence of defects in the sample under study.

We have shown that $Zr_2(PO_4)_2(SO_4)$ doesn't crystallize in space group *Pbcn*. Examination of the low angle diffraction pattern clearly shows reflections which should be systematically absent for space group *Pbcn*. Single crystal measurements on $Zr_2(PO_4)_2(SO_4)$ suggest that the material is still orthorhombic. Our data is consistent with the space groups *P222, P22m, P2mm,* and *Pmmm*.

In Chapter 3, we examined how pressure affects the structure of $Hf_2(PO_4)_2(SO_4)$ which is a close structural relative of $Zr_2(PO_4)_2(SO_4)$. At ambient pressure, reflections are visible at low angle similar to those observed for $Zr_2(PO_4)_2(SO_4)$, suggesting that the hafnium and zirconium phases both crystallize in a lower symmetry space group than other members of the $A_2M_3O_{12}$ family. As the pressure was increased, additional peaks appeared in the diffraction pattern, that did not correspond to an impurity or ruby within the sample. Diffraction patterns at all pressures were modeled using the Le Bail method in space group *P222*. Above 0.57 GPa, the Le Bail fit to the data was quite poor. We found an almost linear dependence of the apparent unit cell volume on pressure, which is unusual. It was suggested that the extra peaks appearing on compression and the unusual pressure dependence of the apparent unit cell volume may be the result of a phase transition or possibly two. However, a unit cell and space group for the possible high pressure polymorphs was not established.

In Chapter 4, we explored the preparation of PbP_2O_7 by the dehydration of $Pb(HPO_4)_2 \cdot xH_2O$. However, we were unable to find a reproducible procedure for the production of high quality PbP_2O_7 samples.

Finally, in Chapter 5, we examined how the local structure of $ZrMo_2O_8$ responded to both temperature and pressure changes using the PDF method. We showed that local

structure of cubic $ZrMo_2O_8$, under ambient conditions, was not well described by either the *$P2_13$* or *Pa-3* crystallographic models for this material. The *Pa-3* model performed well at high r, it was still a poor at short distances. Variable temperature measurements showed that temperature dependence of the nearest neighbor Zr-Mo distances in $ZrMo_2O_8$ was very similar to the bulk CTE. On compression irreversible pressure induced amorphization was observed for $ZrMo_2O_8$. All interatomic correlations above 4 Å were washed out. At shorter distances, however, we observed that Zr-O-Mo linkages remain well defined and do not massively deform as the pressure is increased. We also suggest that Zr-O-Mo linkages change geometry reversibly leading to the formation of an additional Zr-Mo peak at ~3.36 Å when the material is under pressure.